Technische Universität München
Physikalische Chemie I

Investigation of Weak Intra- and Intermolecular Interactions and Conformational Structures of Flexible Molecules and Complexes by Mass Selective High Resolution Resonance Enhanced Two Photon Ionization Laser Spectroscopy

Sotir Chervenkov

Vollständiger Abdruck der von
der Fakultät für Chemie
der Technischen Universität München
zur Erlangung des akademischen Grades eines

Doktors der Naturwissenschaften

genehmigten Dissertation.

Vorsitzender: Univ.-Prof. Dr. St. J. Glaser

Prüfer der Dissertation:

1. Univ.-Prof. Dr. H. J. Neusser
2. Univ.-Prof. Dr. Dr. h. c. A. Laubereau

Die Dissertation wurde am 05.03.2007 bei der Technischen Universität München eingereicht und durch die Fakultät für Chemie am 29.03.2007 angenommen.

To the memory of my father,

Minko Sotirov Chervenkov

Preface

The myriad of chemical and biological systems, their macroscopic properties and functionality, the numerous natural phenomena people encounter, are manifestations of the collective behavour of matter constituents, atoms and molecules, governed by a fascinating subtle interplay between several types of interactions at microscopic level. This model on how the nature is built up recognizes the notion that complexity grows out of simplicity. That is why, for a better understanding of many physical, chemical, and biological processes, and optimization of various applications relevant to biotechnologies, medicine, and industry, a profound insight into the microworld is indispensable.

The interactions between atoms lead to the formation of a qualitatively new objects, molecules, whose properties are completely different in chemical aspect from the ones of their building components. This type of interaction was called *covalent* . Covalent interactions were adequately described as early as 1916 by Lewis [1], five years prior to the formulation of the laws of quantum mechanics. The modelling of covalent chemical bonds has drawn a significant interest and has become a subject of intense experimental and theoretical research over the years thus ultimately leading to a consistent theory which has turned into the pivot of modern chemistry. Along with covalent interactions, there exists another class of interactions termed *noncovalent* (*nonbonded*, *weak*). They were first discovered by the Dutch physicist J. D. van der Waals [2] in the end of the 19th century. Nowadays, it is well established that covalent interactions lead to the formation of classical molecules, crystals, etc., and the nonbonded ones are responsible for the formation of molecular clusters (molecular complexes), liquids, and for solvation processes. It has been found that noncovalent interactions are one-two orders of magnitude weaker compared to covalents ones, and for this reason, the traits of the molecules building up a molecular cluster remain relatively unaffected compared to their isolated state. Still, however, some small changes in the subsystems occur, which can serve as a signature for the cluster formation. It was not until the 1970s when the significance of the noncovalent interactions was recognized in physics, chemistry, and biology-related disciplines. This marked the onset of an active exploration of weak interactions, which is still a hot topic in present time due to its relevance to diverse fields ranging from biochemical and pharmacological research through material sciences.

Most of the processes interesting for chemistry and biology occur in the condensed phase where noncovalent interactions come to the fore and gain additional significance. Noncovalent interactions play an important role in liquids, solvation phenomena, secondary structures of biological macromolecules such as DNA and proteins, molecular recognition, supramolecular chemistry, crystal packing, etc. It has been shown (for a comprehensive review, see [3]) that molecular conformations determine the reactivity and functionality of biomolecules. Molecular shapes on the other hand are stabilized by *intra*molecular noncovalent interactions. For a number of chemical and biological phenomena such as solvation, molecular transport, and molecular recognition, pertinent to transport through membranes, neurotransmission, drug-receptor matching, virus detection, enzyme catalysis, etc., not only the conformations of the involved molecules are important but also the interactions with the molecules of the surrounding environment, which comprise the intermolecular weak interactions. Thus, in real biochemical systems, the ultimate conformational shape and reactive properties of the molecules are determined by the delicate balance between *intra*- and *inter*molecular interactions. This aspect has not been yet fully studied and needs further elucidation. supramolecular chemistry is another realm of noncovalent interactions. It has been aptly defined by Lehn [4, 5] as ”chemistry beyond the molecule”. The so-called noncovalently assisted synthesis is used to produce molecules with predefined shape, respectively properties, employing the stabilization provided by the recognition binding sites embedded in the precursors. It provides a convenient means for *targeted* synthesis of varios supramolecular structures. Depending on the particular system, various types of nonbonded interactions can be harnessed: hydrogenbonds (H-bonds), charge-transfer interactions, electrostatic interactions, hydrophobic interactions, stacking interactions, metal coordination [6]. By noncovalently assisted synthesis special new materials can be produced, which meet specific requirements. Thus, for instance, polymers whose molecules are bound by both covalent and noncovalent interactions manifest novel and drastically different physical, chemical, electrochemical, photochemical, optical, thermal, and catalytic properties in comparison with the classical polymers, based only on covalent bonds. The applications of targeted synthesis cover diverse fields: drug design [7], catalysis [8, 9], molecular electronics [10].

The detailed study of nonbonded interactions necessitates investigation of well-defined finite-sized isolated model systems of molecules and molecular complexes. This has provided a great impetus for the development of techniques for production of the aforementioned model systems in the gas phase. The most advantageous and robust method for isolating molecules and molecular clusters in the gas phase is the supersonic jet expansion leading to the formation of molecular beams [11]. In cold molecular beams, the translational and internal degrees of freedom are cooled down [11, 12] and as a result, along with the isolated molecules, weakly bound complexes held by nonbonded intermolecular interactions are formed. These complexes survive on a timescale of several microseconds after the adiabatic expansion. An additional asset of molecular jet expansion is that it allows, through varying of certain parameters, for an efficient control of

the cluster formation process, thus making possible the formation of complexes of different size ranging from two to tens of molecules in a frigid state, which is on the grey line between the gas phase and bulk condensed phase [13]. In the cold molecular beam, the species do not interact with each other and thus can be considered as nonperturbed by external influences.

Laser spectroscopy provides versatile and powerful, yet nondemolishing and gentle, means for probing of isolated species. So far, a great number of spectroscopic techniques have been developed to investigate various aspects of the structure and dynamics of isolated molecules and molecular complexes. Because of the low density and total number of species in the molecular beam, the spectroscopy of electronic states is often preferred compared to microwave and infrared spectroscopy. The UV electronic excitation of an isolated species can be relatively easily detected. The simplest way is to monitor the spontaneous fluorescence emission from the excited electronic state. This technique is commonly known as laser induced fluorescence (LIF). Measuring the fluorescence decay in the time domain, one can readily obtain information on the dynamics of the respective electronically excited state. Such type of measurement is not attainable by microwave and infrared spectroscopy due to the small spontaneous emission probability stemming from the ν^3 law (for review, see [14]). A powerful UV laser spectroscopy technique, particularly suitable for detection of electronically excited complexes in the cold molecular beam, is the resonance enhanced two-photon ionization (R2PI) spectroscopy, in which a further photon is absorbed in the electronically excited state leading to ionization of the species. This techniques provides an additional experimental advantage compared to LIF; this is the mass selectivity. This feature is particularly important when many different species are present in the cold molecular beam, as is usually the case. On top of the exerimental advantages R2PI spectroscopy yields important information on the dynamics and energy transfer occurring upon deposition of a certain amount of energy in the electronically excited states, resulting in a fragmentation of the species. For noncovalently bound complexes it is interesting to observe the energy redistribution from excited intramolecular vibronic modes to intermolecular modes. This is closely related to the stability of weakly bound complexes in electronically excited states since if the deposited vibronic energy exceeds the cluster dissociation energy, this will lead to a fragmentation of the complex (for review, see [15]). Such experiments are of paramount importance in photochemistry, particularly concerning the stability of biological systems such as DNAs.

R2PI UV spectroscopy with spectral resolution of several tenths of a cm^{-1} is referred to as *vibrational* (low-resolution) since it can resolve only the vibronic structure of the excited electronic state but not the rotational one. It has provided over the years a wealth of valuable information on the vibrational structure of many molecules and molecular complexes [16]. The change of the binding energy of molecular clusters upon electronic excitation can be obtained by measuring the frequency shift of the rotationless transition due to the complexation [17–19]. The width of vibronic bands can also serve as a source of information on the energetics and dynamics of molecular complexes [20, 21]. Further, a detailed and accurate information, particularly on the

structure of isolated molecules and molecular complexes, can be retrieved from the experimental technique combining *i*) *rotationally resolved* (high-resolution) R2PI UV spectroscopy and *ii*) mass selectivity. This method features several important assets:

- it enables a selection of the particular molecular complex to be studied.
- it provides a resolution of the rotational structure and hence, the values of the molecular inertial parameters and transition moment ratio.
- it makes possible on the basis of the obtained molecular parameters, the geometrical structures of the observed species to be reliably assigned, even in the case of complex molecular systems.

For high-resolution spectroscopy it is necessary that the Doppler broadening be eliminated. It is known that the Doppler broadening is the limiting factor in room- temperature measurements since it mars the spectral resolution and the rotational lines are concealed under the envelope of the Doppler width. That is why, cold supersonic molecular beams provide advantages also in this case. They inherently reduce the transverse velosity distribution of the species and hence, the Doppler broadening [22–24]. Rotationally resolved R2PI UV spectroscopy with mass selectivity is helpful also in the analysis of isomerization and fragmentation processes occurring upon electronic excitation.

For a successful and reliable analysis and interpretation of highly resolved spectra of large molecules and molecular complexes, which are composed of densely spaced and partially overlapping rotational lines, a special fitting routine based on genetic algorithms has been developed in our group. It is able to determine the rotational constants, the transition moment ratio, and other molecular parameters, from spectra with densely spaced peaks or low signal-to-noise ratio.

The structures of molecular conformations are encoded in their highly resolved spectra. It is well-known, however, that for molecular systems with complex shape, the rotational constants alone, respectively principal moments of inertia, obtained from the high-resolution spectra do not provide unique information on the structure of the observed molecule or molecular . To assign molecular structures, the experimental results have to be combined with theoretical simulations based, in most cases, on *ab initio* quantum chemistry calculations. Quantum chemistry calculations of large molecules and molecular complexes bound by noncovalent forces were almost intractable or unreliable due to the intrinsic flexibility of such systems [25–30]. An additional challenge posed to this type of systems is often the very flat and anharmonic potential energy surface. The rapid development of numerical algorithms combined with the progress in computational power available, however, has significantly enhanced the reliability and expanded the applicability of quantum chemistry computations of the energetics, structure, dynamics, and frequency analysis of structures stabilized by weak interactions. Thus, the strategy successfully demonstrated in the present work employs the synergism between high-resolution R2PI UV spec-

troscopy with mass selectivity and high-level quantum chemistry *ab initio* calculations: theory predicts possible geometrical structures and the experimental results show which of them are observed under the experimental conditions.

The most widely studied molecules are the aromatic ones, and their clusters in the gas phase. There are two reasons for considering such systems. The first one is that the aromatic rings are present in a great deal of organic and biologically relevant molecules. They are typical examples for molecules containing delocalized electrons, which play an important role in nonbonded interactions. The second argument to focus on benzene-containing molecules is that they are good chromophores and thus are suitable for laser spectroscopy investigations.

The purpose of the present work is to present a systematic investigation of various noncovalent intra- and intermolecular interactions and the subtle interplay between them with a special emphasis on the following issues highlighted in the respective chapters:

- The effect of the *π-electron conjugation* on the structure of an aromatic molecule containing a side chain covalently bound to a benzene ring. This phenomenon is manifested in styrene, described in Chap. 7.
- Formation of a *nonconventional* C-H$\cdots\pi$ bond. Binding preferences and binding pattern of the complex between styrene and acetylene. The issue on how the π-electron system of the acetylene molecule interacts with the two conjugated π-electron systems of styrene, whether in the complex acetylene acts as a proton donor or as a proton acceptor, is elucidated also in Chap. 7.
- Weak van der Waals *dispersion* interactions in a system with conjugated π-electron systems: Ar binding to styrene. The discussion on this topic is in Chap. 8.
- The effect of a strongly electronegative substituent on the electronic distribution of a molecule with conjugated π electrons. Competing phenomena: *mesomeric* vs. *electron-withdrawing* effects. Formation of a classical intermolecular hydrogen bond. Favoured binding site and cluster pattern of the singly hydrated complex of *p*-fluorostyrene (see Chap. 9).
- The effect of intramolecular weak interactions for the stabilization of biologically relevant molecules: the neurotransmitter molecule, ephedrine (Chap. 11), and neurotransmitter analogue, 2-phenylethanol (Chap. 10).
- Interplay between intramolecular O-H$\cdots\pi$ bond and an intermolecular dispersion interaction present in the model cluster between 2-phenylethanol and Ar (Chap. 10).
- Conformationally selective fragmentation: the neurotransmitter molecule, ephedrine (Chap. 11).

Contents

Preface **3**

I Theoretical Fundamentals **15**

1 Molecular Interactions **17**
1.1 Chemical Bonds . . . 17
1.2 Weak Molecular Interactions . . . 18
1.2.1 Attractive Molecular Interactions . . . 18
1.2.2 Repulsive Molecular Interactions . . . 20
1.3 The Concept of Weak Molecular Bonds . . . 20
1.4 Classification of Weak Molecular Bonds . . . 22
1.4.1 Hydrogen Bonds . . . 22
1.4.2 Quadrupole-Quadrupole Bonds . . . 24
1.4.3 Charge-Transfer Bonds . . . 24
1.4.4 Ion-Mediated Bonds . . . 24
1.4.5 Hydrophobic Interactions . . . 25
1.4.6 Dispersion Bonds . . . 25
1.5 Binding Motifs . . . 25

2 *Ab Initio* Quantum Chemistry Calculations **27**
2.1 Semiempirical Methods . . . 27
2.2 *Ab Initio* Quantum Chemistry Calculations . . . 28
2.2.1 Self-Consistent Field Hartree-Fock (SCF-HF) Method . . . 28
2.2.2 Basis Functions . . . 28
2.2.3 Configuration Interaction (CI) . . . 30
2.2.4 Configuration Interaction Singles (CIS) . . . 31
2.2.5 The Møller-Plesset Perturbation Theory . . . 32
2.2.6 The Coupled-Cluster Method . . . 33
2.3 Density-Functional Theory . . . 34

2.4 Molecular Mechanics . . . 35
2.5 Molecular Geometry . . . 35
2.5.1 Equilibrium Geometry . . . 35
2.5.2 Potential Energy Surface . . . 36
2.5.3 Geometry Optimizations . . . 36
2.5.4 Conformational Search . . . 37
2.6 Molecular Vibrational Frequencies . . . 37
2.7 Programme Packages for Theoretical Molecular Investigations . . . 38

3 Interaction between Light and Matter 39

4 Molecular Quantum Mechanical Characteristics and Molecular Structure 43
4.1 Born-Oppenheimer Approximation . . . 43
4.2 Rotation of Molecules . . . 44
4.2.1 Molecular Rotational Energy . . . 45
4.2.2 Molecular Rotational Energy Levels . . . 46
4.2.3 Electric Dipole Transition Moment . . . 49
4.2.4 Selection Rules . . . 49
4.2.5 Transition Intensity . . . 49
4.2.6 Deviations from the Born-Oppenheimer Approximation . . . 50
4.3 Rotational Constants and Structure of Molecular Species . . . 50

II Spectroscopic Investigation of Molecular Systems 53

5 The Concept of Spectroscopy 55
5.1 Survey on Molecular Spectroscopy Techniques . . . 55
5.2 Molecular Electronic Spectroscopy . . . 56
5.2.1 UV Laser Induced Fluorescence . . . 56
5.2.2 UV Resonance Enhanced Multiphoton Ionization . . . 57
5.2.3 Spectrosopy of Resolved High Rydberg States . . . 57
5.2.4 Zero Kinetic Energy (ZEKE) and Mass Analysed Threshold Ionization (MATI) Spectroscopies . . . 57
5.2.5 Double Resonance Spectroscopy . . . 58
5.3 Near- and Far-Infrared Laser Spectroscopy . . . 58
5.4 Microwave Spectroscopy . . . 59
5.5 Raman Spectroscopy . . . 59
5.6 Rotational Coherence Spectroscopy . . . 60
5.7 Gas Electron Diffraction . . . 60

6 Resonance Enhanced Two-Photon Ionization Spectroscopy in Molecular Beams 61
6.1 Resonance Enhanced Two-Photon Ionization (R2PI) UV Laser Spectroscopy . . 62
6.2 Experimental Set up 63
6.2.1 Cold Supersonic Molecular Beams 63
6.2.2 Laser System 66
6.2.3 Control of the Experiment. Data Acquisition System 68
6.3 Genetic Algorithm 68

III Results and Discussion 73

7 Evidence for a C-H$\cdots\pi$ Type Weak Ineraction: Styrene-Acetylene Complex 75
7.1 Introduction 76
7.2 Experiment and Data Processing 78
7.3 Results 78
7.3.1 *Ab initio* Calculations 78
7.3.2 Vibronic Spectra of the ST·C_2H_2 Cluster 81
7.3.3 High Resolution Spectrum of the 0_0^0 Origin Band of ST·C_2H_2 83
7.4 Discussion 86
7.5 Summary and Conclusions 90

8 van der Waals Complex of Styrene with Argon 93
8.1 Introduction 94
8.2 Experiment and Data Processing 95
8.3 *Ab Initio* Calculations 95
8.4 Experimental Results 97
8.4.1 Low Resolution Spectra 97
8.4.2 High Resolution Spectrum 97
8.5 Discussion 98
8.6 Summary and Conclusions 101

9 Evidence for a σ-type Hydrogen-Bonded Dimer: *p*-Fluorostyrene-Water 103
9.1 Introduction 104
9.2 Experiment and Data Processing 104
9.3 Results and Discussion 105
9.3.1 *Ab Initio* Calculations 105
9.3.2 Vibronic Spectra of the *p*-FST·H_2O Cluster 108
9.3.3 High Resolution Spectrum of the 0_0^0 Origin Band of the *p*-FST·H_2O Cluster 112
9.4 Summary and Conclusions 114

10 Dispersion and H- Bonding: The Complex between 2-phenylethanol and Ar 115
10.1 Introduction . . . 116
10.2 Experiment and Data Processing . . . 117
10.3 Experimental Results . . . 117
10.3.1 Low Resolution Spectrum . . . 117
10.4 High Resolution Spectra . . . 119
10.4.1 Main Band . . . 119
10.4.2 Red-shifted Band . . . 121
10.5 Theoretical Results . . . 124
10.5.1 *Ab Initio* Results . . . 124
10.5.2 Kraitchman Equations . . . 126
10.5.3 Transition Moment Orientation . . . 128
10.6 Discussion . . . 130
10.7 Summary and Conclusions . . . 132

11 Fragmentation and Conformational Preferences of Ephedrine 135
11.1 Introduction . . . 136
11.2 Experiment and Data Processing . . . 137
11.3 Results and Discussion . . . 137
11.3.1 Low Resolution Spectra . . . 137
11.3.2 High Resolution Spectrum . . . 140
11.4 Summary and Conclusions . . . 141

IV Concluding Remarks 145

Bibliography 154

List of Figures 170

List of Tables 172

List of Publications 175

Poster and Oral Presentations 176

Index 178

Part I

Theoretical Fundamentals

Chapter 1

Molecular Interactions

This chapter presents the molecular interactions and their most important characteristics. It makes a classification of the weak intermolecular bonds along with examples of their typical occurrrences. Stabilization of molecular structures and binding patterns of molecular clusters resulting from the subtle interplay between various weak interactions are highlighted.

1.1 Chemical Bonds

The formation of chemical bonds is a quantum mechanical phenomenon manifesting itself in the interaction of two atoms and resulting in the building of more complex objects such as molecules and solids. Chemical bonds can be subsumed into three main categories: *covalent* (homopolar), *ionic*, and *metallic* [31].

- Covalent bonds are formed by sharing an electron pair between two atoms, thus leading to a minimization of the total energy of this system. When two identical atoms form a covalent bond, for instance H_2, O_2, etc., the electron density is distributed symmetrically between them and the bond in this case is referred to as *nonpolar*. In general, however, the two atoms participating in the covalent bond formation have different electron affinities, and hence the electron density is shifted towards the one with higher electronegativity, thus resulting to a *polar* bond: HCl, HF, etc.

- In the extreme case, when the difference of electron *affinities* of the two atoms is very large, the electon pair is shifted to the strongly electronegative atom, thus giving rise to the formation of two electric charges which are held together by Coulomb electrostatic attraction. In this way the strongly polar covalent bond transforms into an *ionic* bond such

as in the case of NaCl, for instance. The border between strongly polar *covalent* and *ionic* bonds, however, is not rigorously set.

- *Metallic* bonds are strongly delocalized. They result from sharing the valent electrons, which are in the conduction band, between all atoms, thus forming the so-called electron gas.

Chemical bond energies range between 1 and 10 eV, and their typical distances are between 1 and 3 Å. They determine the ‘skeletal‘ structure of molecules.

1.2 Weak Molecular Interactions

In isolated molecules the negatively charged electron shell shields off the positively charged molecular core, thus yielding a neutral system. When molecules are close to one another, however, their electron shells experience not only the influence of their own positive cores but also the presence of the electron shells of the surrounding molecules. This brings about a deformation and redistribution of the electron charge within the molecules, leading to an incomplete shielding of the positive cores and, respectively, to the appearance of locally charged molecular species. Thus, molecules interact with one another by electrostatic forces acting between the positively charged molecular cores and the negatively charged shells. Weak molecular interactions are also referred to as *nonbonding* or *noncovalent* to distinguish them from chemical (also called *bonding*) interactions. Nonbonding interactions are two types: *attractive* and *repulsive*. *Attractive* weak molecular interactions are classified as *electrostatic*, *inductive*, and *dispersion*. *Repulsive* interactions stem from the Pauli exclusion principle.

1.2.1 Attractive Molecular Interactions

Permanent-Charge-Distribution Interactions

Static charge distributions can be expanded in a series of multipole moments. Thus, two molecules, A and B, interact with each other through the interaction of the static multipole moments of their charge distribution. That is why, this type of intermolecular interaction is referred to as *electrostatic*, and the resulting interaction energy is designated as E_{el}. This type of intermolecular interactions is subject of the *first-order perturbation theory* . The electrostatic energy can be presented in the following way:

$$E_{\mathrm{el}} = \frac{q_{\mathrm{A}}q_{\mathrm{B}}}{|\mathbf{r}|} + \frac{q_{\mathrm{A}}|\boldsymbol{\mu}_{\mathrm{B}}|}{\mathbf{r}^2} + \frac{q_{\mathrm{B}}|\boldsymbol{\mu}_{\mathrm{A}}|}{\mathbf{r}^2} + \frac{\boldsymbol{\mu}_{\mathrm{A}}\cdot\boldsymbol{\mu}_{\mathrm{B}}}{|\mathbf{r}|^3} + \frac{q_{\mathrm{A}}Q_{\mathrm{B}}}{|\mathbf{r}|^3} + \frac{q_{\mathrm{B}}Q_{\mathrm{A}}}{|\mathbf{r}|^3} + \frac{\boldsymbol{\mu}_{\mathrm{A}}\cdot Q_{\mathrm{B}}}{\mathbf{r}^4} + \frac{\boldsymbol{\mu}_{\mathrm{B}}\cdot Q_{\mathrm{A}}}{\mathbf{r}^4} + \frac{Q_{\mathrm{A}}\cdot Q_{\mathrm{B}}}{|\mathbf{r}|^5} + \cdots \quad (1.1)$$

where q, $\boldsymbol{\mu}$, Q, and $\mathbf{r}$ stand for the *electric charge*, *electric dipole moment*, *electric quadrupole moment*, and the *position vector* of the second molecule relative to the first one, respectively. It is important to emphasize that the energy, E_{el} depends not only on the magnitude of the multipoles but also on their mutual orientation (this is encoded in the dot products in Eq. 1.1). That is why, in natural systems the molecules are oriented such as to minimize the total electrostatic energy. It is obvious from Eq. 1.1 that the magnitude of the higher-order terms in the multipole expansion dwindles down very rapidly with the intermolecular distance (inverse power law) and for this reason, the interaction energy can be described fairly accurately only by retaining the first nonvanishing terms in the multipole series. Some molecules, due to symmetries, do not have low-rank permanent multipoles, and hence necessitate the inclusion of higher-order terms. There exist also molecular systems, e.g., complexes with rare gas atoms, that do not have permanent multipoles at all, and for them the electrostatic interactions do not come to the scene.

Induction Interactions

The induction interaction between two molecules, A and B, originates from the interaction between the permanent dipole moment of one of the molecules with the induced dipole moment (it induces) in the other one. The magnitude of the induced dipole moment depends on the magnitude of the permanent dipole moment, the spacing between the two molecules, and the *polarizability* α of the molecule in which the dipole moment is induced. This model constitutes the so-called *second-order perturbation theory* . The potenatial energy of induction interactions, E_{ind}, can be presented in the form:

$$E_{\mathrm{ind}} = -\frac{1}{2}\alpha_{\mathrm{B}}\left(\frac{q_{\mathrm{A}}^2}{\mathbf{r}^4} + f_1(\boldsymbol{\mu}_{\mathrm{A}}, \boldsymbol{\mu}_{\mathrm{B}})\frac{\boldsymbol{\mu}_{\mathrm{A}}^2}{\mathbf{r}^6} + f_2(\boldsymbol{\mu}_{\mathrm{A}}, \boldsymbol{\mu}_{\mathrm{B}})\frac{Q_{\mathrm{A}}^2}{\mathbf{r}^8}\right), \tag{1.2}$$

where α, q, $\boldsymbol{\mu}$, and Q designate the polarizability, the electric charge, the electric dipole moment , and the electric quadrupole moment , respectively. The molecule with permanent multipoles is denoted by A, and the one with induced multipoles by B. Functions f_1 and f_2 depend on the mutual orientation of the two molecules, A and B.

Dispersion Interactions

Dispersion interactions constitute the third type of attractive intermolecular interactions. They derive from the mutual polarization of the instantaneous electron density distributions of the two monomers, A and B. They were for the first time rationalized and described by London [32], and hence called also *London* inetractions. The potential energy of such an interaction, E_{disp}, can be cast in the form

$$E_{\text{disp}} = -\frac{C_6}{\mathbf{r}^6} - \frac{C_8}{\mathbf{r}^8} - \frac{C_{10}}{\mathbf{r}^{10}} - \cdots \tag{1.3}$$

C_6, C_8, C_{10}, etc. are empirical constants, and $\mathbf{r}$ is the position vector of the molecule B relative to molecule A. London [32] has discovered a relation between the above-mentioned constants and the polarizabilities α_A and α_B of the two interacting molecules, A and B, and their ionization energies. Notwithstanding it is the weakest among the attractive interactions, the dispersion interaction gains importance in nonpolar molecular complexes where it gives rise to the only binding force. Hence, it is of paramount importance in large molecules with large polyrizability, and in complexes containing a noble-gas atom, as will be shown in this work.

1.2.2 Repulsive Molecular Interactions

The only repulsive intermolecular interaction arising when two molecules, A and B, are close to each other stems from the *exchange* interaction. The latter is a manifestation of the fundamental Pauli exclusion principle, which precludes the penetration of electrons from one of the molecular moieties into the occupied orbitals of the other one. The description of the exchange interaction is based completely on quantum mechanics. The resulting energy, E_{exch} has been mathematically formulated by Heitler and London [31–33] through an exponential or inverse power law :

$$E_{\text{exch}} = A \cdot e^{-\frac{2r}{a_0}} \tag{1.4}$$

$$E_{\text{exch}} = \frac{B}{r^n} \tag{1.5}$$

In Eq. 1.4 a_0 is the Bohr radius of the hydrogen atom, and A is an empirical constant. In Eq. 1.5 B is an empirical constant, and the power n ranges between 10 and 20. The inverse-power low describes the exchange repulsion in cases of very small separation distances between the two molecules, A and B.

1.3 The Concept of Weak Molecular Bonds

Weak molecular interactions (descibed above) are not isolated but usually co-exist and act co-operatively. The net effect of the concurring weak interactions is a result of a delicate balance between them, ultimately leading to the formation of a weak bond whose nature, however, is different from the nature of chemical bonds (see Sec. 1.1 above) altogether. Its strength is typically

from one to two orders of magnitude weaker compared to the one of chemical bonds, depending on the nature of the particular molecular system and the weak interactions involved. Usually, the energy of weak molecular bonds, E_{bond}, is in the range of 0.01-1 eV, and the interatomic distances are longer (2-5 Å) than the ones in the case of chemical bonds.
The total energy of a weak molecular bond, E_{bond} can be presented as a sum of the energies of the interactions involved

$$E_{\text{bond}} = E_{\text{attr}} + E_{\text{rep}} = E_{\text{el}} + E_{\text{ind}} + E_{\text{disp}} + E_{\text{exch}} \tag{1.6}$$

The interaction potential and its two constituents, the *repulsive* and the *attractive* potentials, are presented schematically in Fig. 1.1

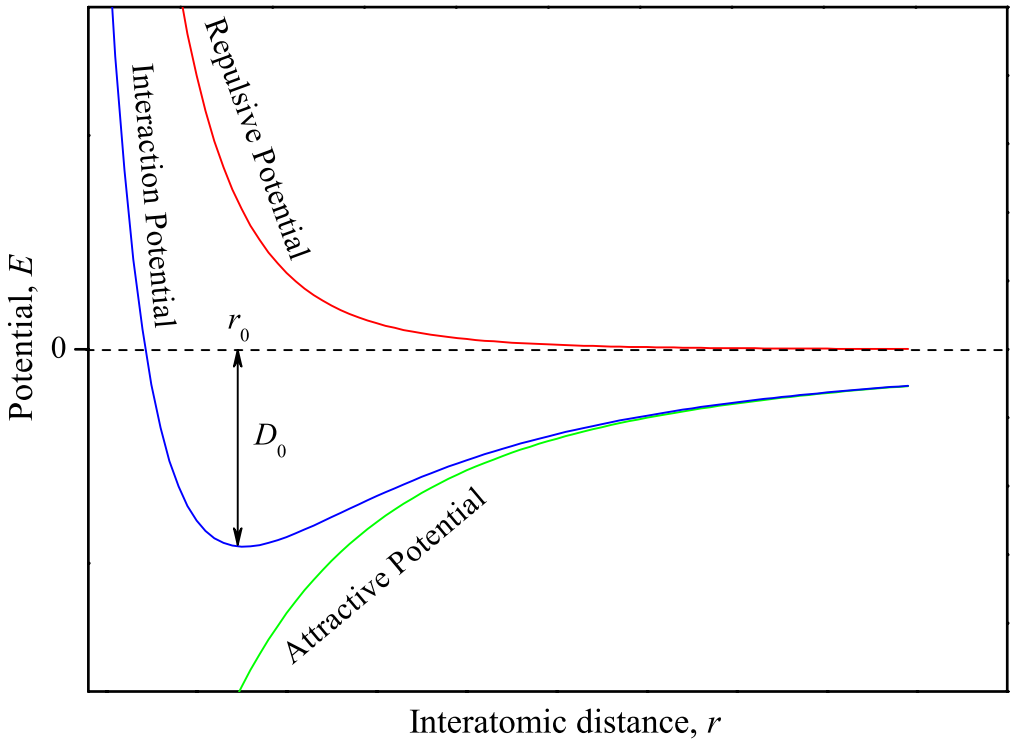

Figure 1.1: *Schematic representation of a weak two-atom molecular interaction potential composed of a repulsive and attractive potentials. r_0 designates the interatomic distance corresponding to the the minimum of the potential well, and D_0 is the depth of the potential well.*

It is interesting to observe that due to the balance between the attractive and repulsive potentials, in most cases, there exists an equilibrium interatomic distance, r_0, at which the net interaction energy has minimum. It may happen, however, that the attractive potential cannot make up for the action of the repulsive potential at any point, thus leading to a nonbonding potential, i. e.,

a potential that do not pertain a minimum. In this case no weak bond can be formed. It is important, however, to point out that for a bond to be formed, not only must the potential have a minimum, but also the zero-point vibrational level must be below the dissociation energy.
Very often, for practical needs, the shape of the interaction potential must be known. Obtaining the shape of the potential starting from first principles and considering all types of interactions involved is quite demanding, and in most cases, untractable problem. Another approach to solving the problem is to devise a model potential, i.e., a special function containing free parameters, as the ones shown in Fig. 1.1, and to fit those parameters to experimental data. The simplest, yet sustainably popular one, was suggested by Morse [34] in 1929. It is a zeroth-order approximation to experimental potentials. To more accurately describe real potentials, one has to resort to more complex potentials, the most commonly used one being the famous Lennard-Jones potential [31, 35, 36]. It includes two terms accounting for repulsive and the attractive interactions.
In real systems, the interactions are not constrained to two-body ones. For an adequate desscription of weak molecular interactions involving more than two particles, the many-body interaction is reduced to a two-body interaction, wherein the above-discussed treatment applies.

1.4 Classification of Weak Molecular Bonds

The combination of the various types of weak molecular interactions gives rise to a big variety of bonding patterns. Though there is no rigorous borderline between them, a general classifcation according to the nature of the interactions involved, bond energies, and bond lengths can be made.

1.4.1 Hydrogen Bonds

Hydrogen bonds (H-bonds) are one of the most abundant and important types of weak molecular interactions in nature. They determine the properties and behaviour of liquids and biological systems. Hydrogen bonds have the general motif X-H$\cdots$Y, where the X-H group is a *proton donor* , and Y is a *proton acceptor* . Usually, X is an electronegative atom (O, N, Cl, F, etc.), and Y is most typically either an atom possessing a lone electron pair or it is a π-electron system (benzene ring, or double or triple chemical bond), which has an excess of electron density. Weak hydrogen bonds involving a π-electron system have attracted scientists' attention for more than 60 years since Dewar's work [37] appeared, and their significance has been recognized in many biologically relevant systems. It was not until recently, when the importance of another specific type of hydrogen bonds was realized; these are the C-H$\cdots$Y (nonconventional) hydrogen bonds [38–42], which play an important role for the stabilization of molecular structures. Usually, Y is an electronegative atom or a π system. They are much weaker compared to the

conventional hydrogen bond, and with respect to the binding energy they are at the borderline between hydrogen bonds and dispersion bonds (see below).

The most significant features and properties of hydrogen bonds are highlighted in the following.

- Hydrogen bonds are stabilized by a subtle interplay between electrostatic, induction (charge-transfer), and dispersion interactions [43]. The most important contribution, however, is the electrostatic one, realized mainly through dipole-charge and dipole-dipole coupling. This brings about the next traits of hydrogen bonds.
- Hydrogen bonds provide a typical example of a two-body interaction. Due to the electrostatic attraction the H-bond length is shorter than the sum of the van der Waals radii of the two atoms, X, and Y.
- *Directionality*. Hydrogen bonds are strongly directional, i. e., the three atoms, X, H, and Y, lie down a straight line.
- Typical H-bond lengths range between 2 and 3 Å.
- The energy of H-bonds varies between 0.1 and 1 eV, depending on the nature of X and Y atom (groups), and consequently, on the relative contributions of the constituting interactions. Thus, some H-bonds render themselves at the brink of chemical bonds

Altogether hydrogen bonds can be subsumed into three major groups: *proper* (*red-shifting*), *improper* (*blue-shifting*), and *dihydrogen* bonds.

Proper Hydrogen Bonds

Proper (red-shifting) hydrogen bonds weaken the covalent X-H bond thus leading to its elongation, and respectively, to a red shift of the X-H stretching vibrations . The nature of this effect has been explained on the basis of bond orbital analysis [43, 44]. The latter shows that a charge transfer takes place from the lone electron pair or the π-electron system of the proton acceptor to the antibonding orbitals of the proton donor. This leads to an increase of the electron density in the antibonding orbitals, which causes the weakening of the X-H chemical bond, and to its elongation.

Improper Hydrogen Bonds

Improper (blue-shifting) hydrogen bonds [43, 45] exhibit behaviour opposite to the one of proper hydrogen bonds (see above), i. e., upon the formation of such weak bonds the chemical X-H bond shortens and the frequency of the X-H vibration increases. Blue-shifting hydrogen bonds

were theoretically predicted for carbon proton donor-benzene complexes [46] and later on, their existence was experimentally verified for the model system chloroform-fluorobenzene complex [47]. As in the case of red-shifting bonds, a charge transfer process underlies the observed phenomena. In this case, however, the charge transfer is directed to the remote part of the X-H bond, followed by a structural change in the proton-donor molecule.

Dihydrogen Bonds

Dihydrogen bonds [43, 48] have the pattern X-H$\cdots$H-Y, where X is an atom of a metal element, and Y is an electronegative atom. They were discovered only recently in a hydrogen-bonded complex containing Ir [49]. The mechanism of these bonds was rationalized a bit later [50], and it is quite straightforward. The metal atom donates electron density to the covalently attached to it H atom, thus creating a partial negative charge upon it. On the other hand the electronegative atom Y withdraws the electron density from the adjacent H atom so that the latter becomes positively charged. In this way the dihydrogen bond is stabilized by a multipole interaction.

1.4.2 Quadrupole-Quadrupole Bonds

The occurence of *quadrupole-quadrupole* bonds is limited to systems containing benzene rings. They determine the T-shape structure of the benzene dimer, and play an important role for the stabilization of secondary and tertiary structures of macromolecules.

1.4.3 Charge-Transfer Bonds

Charge-transfer (CT) bonds emerge when one of the bonded moieties is a good electron donor (it has a low ionization potential), and the other one has high electron affinity. Donors pertain antibonding orbitals designated as n, σ, and π, respectively, and acceptors have vacant orbitals labelled as v*, σ*, and π*, respectively. The strongest of the so-formed CT complexes are the ones of n-v type.

1.4.4 Ion-Mediated Bonds

Ion-mediated bonds stem from the presence of metallic cations, which have high electron affinity, and hence form polar bonds on the basis of multipole interactions.

1.4.5 Hydrophobic Interactions

Hydrophobic interactions are a special class of interactions representing associations of non-polar groups in polar solvents. It has been found [43, 51, 52] that the change of the enthalpy is almost vanishing, and the driving force for the reorganization of the molecules in a solution is the entropy. This is their most distinctive feature compared to the above-described bonds, which are formed as a result of an energy minimization.

1.4.6 Dispersion Bonds

Dispersion bonds are formed when the interacting moieties do not have permanent charge distribution, and hence only the dispersion term in the attractive potential is accounted for. Dispersion bonds lack directionality and help for the stabilization of molecules and molecular complexes. Their manifestation is most pronounced in molecular complexes containing a noble-gas atom. Examples for the formation of such a bond are discussed in Chap. 8 and Chap. 10 of this work.

1.5 Binding Motifs

Weak interactions and weak bonds can be *intra*molecular or *inter*molecular. Intramolecular weak bonds play an important role for the stabilization of molecular structures, in particular, those that have many internal degrees of freedom and can assume different conformational shapes. The most abundant intramolecular bonds are the hydrogen ones, though quadrupole-quadrupole bonds are also observed. The most typical occurrence of such bonds is in biologically relevant molecules, as will be discussed in Chap. 10 and Chap. 11. *Inter*molecular bonds are responsible for the formation of supramolecular structures . When benzene-ring-containing molecules are involved in the formation of a complex with another molecule, two binding patterns are possible. A bond that is formed between an atom/molecule and the π electrons of the host molecule is referred to as a π bond. A bond that is realized between an atom/molecule and a benzene-ring substituent is termed a σ bond. An example for an intermolecular σ bond is presented in Chap. 9. A π-bonding motif of a C-H$\cdots\pi$ bond is discussed in Chap. 7.

The molecular interactions and molecular bonds are summarized and presented with their interconnections schematically in Fig. 1.2.

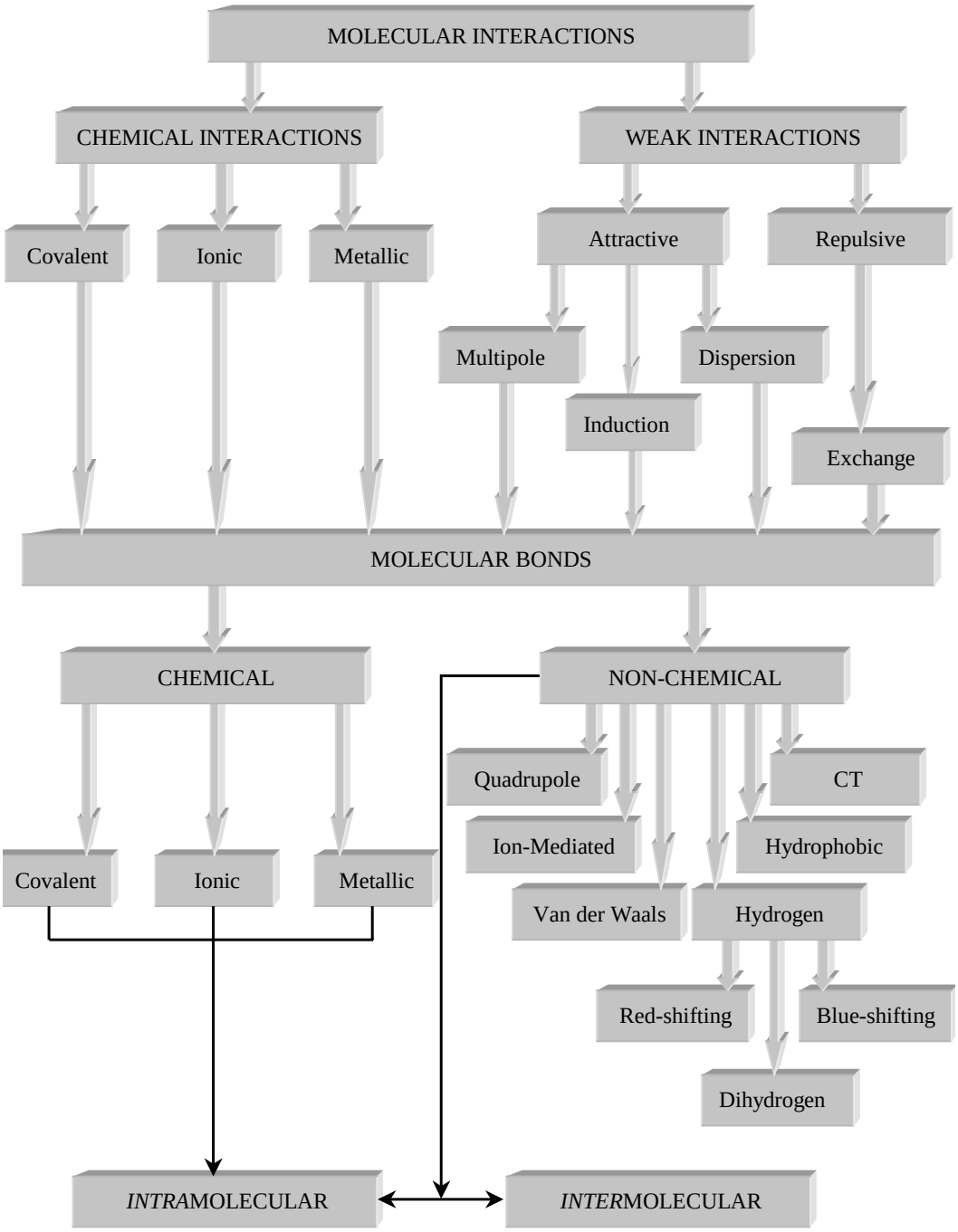

Figure 1.2: *Schematic representation of the various types of molecular interactions and molecular bonds, and the interconnections between them.*

Chapter 2

Ab Initio Quantum Chemistry Calculations: Structure, Energetics, and Frequency Analysis of Isolated Molecular Species

The interpretation of the experimental results is greatly underpinned by theoretical studies. The theoretical prediction of molecular properties has ever been a challanging task. Many models describing one or a few aspects of the molecular behaviour have been developed over the years. Until recently, many theoretical studies even on small molecules were untractable due to their, mainly, mathematical complexity. The rapid enhancement of computational power, however, has stimulated the development of sophisticated algorithms, and enabled the treatment of medium-sized and large molecules and molecular complexes [53–55]. The existing methods for the calculation of molecular structures and properties can be grouped in four categories, which are descibed in the following. The main emphasis, however, is put on the quantum-mechanical methods, which will be presented in more details [56].

2.1 Semiempirical Methods

Semiempirical models use for the description of molecules a simpler Hamiltonian than the real one, and employ a set of parameters whose values are adjusted to match the experimental data, and hence the name semiempirical. A typical example of such a model is the Hückel molecular orbital model (for definition of MO see Sec. 2.2.1), which employs a one-electron Hamiltonian, and the bond integrals play the role of the adjustable parameters.

2.2 *Ab Initio* Quantum Chemistry Calculations

Ab initio quantum chemistry calculations are based on the use of the 'first principles' and the fundamental physical constants. They employ the true molecular Hamiltonian, which accounts for all the interactions within the molecular system. It should be pointed out, however, that due to the approximations inevitably introduced in the solving of the Schrödinger equation, *ab initio* calculations do not provide the exact solution to the treated problem. The main idea on how the Schrödinger equation can be solved along with some important concepts are desribed below.

2.2.1 Self-Consistent Field Hartree-Fock (SCF-HF) Method

The purely electronic nonrelativistic Hamiltonian for a polyatomic molecule is presented in the form

$$\hat{H}_{\text{el}} = -\frac{1}{2}\sum_i \nabla_i^2 - \sum_i \sum_a \frac{Z_a}{|\mathbf{r}|_{ia}} + \sum_i \sum_{i\geq j} \frac{1}{|\mathbf{r}|_{ij}}, \tag{2.1}$$

where the second term in the Hamiltonian represents the interaction of the electrons with the nuclei, and the third member describes the interelectronic interaction. It can be shown [57] that if the interelectronc repulsions are neglected, the zeroth-order wave function is the product of *one-electron* spatial functions [56]. The one-electron spatial functions are referred to as *molecular orbitals*. Taking into account the electron spin and the Pauli exclusion principle leads to the zeroth-order wave function, which is the antisymmetrized product of molecular-spin orbitals, each molecular-spin orbital being a product of a spatial MO and a spin function. Hartree-Fock self-consistent field (HF SCF) [58] function is the best function that has the form of an antisymmetrized product of spin-orbitals. It does not account for the interelectronic repulsion. It is convenient for the MOs to be expressed as a linear combination of basis functions. If the set of the basis functions is large enough then the so-presented MOs are an accurate approximation to the HF MOs. Molecular orbitals that have the same energy form a *shell*.

2.2.2 Basis Functions

The idea of decomposition of the HF function into *basis functions* was introduced by Roothan [59]. The one-electron function can be presented by expansion over basis functions in the following way:

$$\phi_i = \sum_k c_{ik}\chi_k, \tag{2.2}$$

The representation of molecular orbitals through basis functions is not unique. For practical reasons, two types of basis functions are commonly used, the Slater-type (ST) and the Gaussian-type (GT) basis functions, the latter being more commonly employed. The Gaussin-type basis functions were suggested in 1950 by Boys [60]. A Cartesian Gaussian basis function centred on atom *a* has the form

$$g_{ijk} = N x_a^i y_a^j z_a^k . e^{-\alpha r_a^2}, \tag{2.3}$$

where i, j, and k are nonnegative integers, α is a positive *orbital exponent*, and x_a, y_a, and z_a are Cartesian coordinates with origin pinned at the nucleus a. N is a normalization factor that satisfies the condition:

$$N = \left(\frac{2\alpha}{\pi}\right)^{\frac{3}{4}} \cdot \sqrt{\frac{(8\alpha)^{i+j+k} i!\, j!k!}{(2i)!(2j)!(2k)!}} \tag{2.4}$$

Depending on whether the sum of the integers i, j, and k is 0, 1, or 2, the Gaussian functions are referred to as *s*, *p*, and *d* type, respectively. A Gaussian function does not have a cusp at the origin of the coordiante system, and for this reason, it fails to describe correctly the atomic orbitals for small values of r_a. That is why, rarely are Gaussian functions themselves used, however, as basis functions instead, it is customary to form the basis function as a normalized linear superposition of several *primitive* Gaussians:

$$\chi_k = \sum_l d_{kl} g_l. \tag{2.5}$$

In this linear combination, the primitive Gaussian functions have the same values for i, j, and k, but different values for the orbital exponents, α. Usually, d_{kl} is termed a *contraction coefficient*. A great variety of basis sets has emerged over the years. The correct choice of the basis set depends on the particular problem to be solved and on the computational resources available. More extended basis sets, in principle, provide more accurate theoretical results, but on the other hand are computationally more demanding. Thus, the choice of the ”best” basis set for a certain problem is often a matter of trade-off between accuracy and time spent. A comprehensive survey on *ab initio* basis sets can be found in the following compendium [61].
There are four sources of errors in *ab initio* calculations:

- Neglect of or approximate treatment of electron correlation.

- Incompleteness of the basis set used. This leads to the so-called *basis set truncation error*.
- Omission of relativistic effects.
- Break down of the *Born-Oppenheimer approximation* (See Sec. 4.1 of this chapter).

In most cases the first two factors render the biggest contribution to the theoretical errors. The interaction between the electrons in a molecule leads to an *electron correlation,* i.e., the wave function of an electron is not independent of the wave functions of the other electrons in the considered system. There are various approaches to account for the electron correlation. The first one is to include the interelectronic distances, r_{ij}, between every two electrons in the molecular system. This is the most straigthforward way but it is limited only to small systems containing a few electrons.
Nowadays there exist several *ab initio* methods that employ different approaches to the solution of the complete Schrödinger equation trying to minimize the errors, in particular, those stemming from the electron correlation and the incompleteness of the basis sets. They are presented briefly in the following sections.

2.2.3 Configuration Interaction (CI)

It has been shown [56] for the He atom that the first and higher-order corrections to the wave function mix in contributions from excited electronic configurations. This effect is known as *configuration interaction* or *configuration mixing*, and it is present in all many-electron systems. The configuration interaction is calculated by employing the variational method . The SCF MOs, ϕ_i, are presented as a linear superposition of the basis functions in a basis set. The expansion coefficients are found by solving the HF set of equations [56]. The number of the SCF MOs, ϕ_i, is the same as that of the basis-set functions used. The lowest-energy MOs are the occupied orbitals for the ground electronic state, and the remaining unoccuupied orbitals are referred to as *vacant orbitals*. From the one-electron spin-orbitals one can form *multielectron functions*, Φ_i, having different electron occupancies. These many-electron functions are called *configuration state* functions (CSF) or just *configuration functions*. It can be proved that the true wave function of the system under consideration is a linear combination of the above-described CSF:

$$\psi = \sum_i c_i \Phi_i \tag{2.6}$$

The above equation can be viewed upon as a variation function with respect to the coefficients c_i aiming at the minimization of the variational integral

$$\frac{\int \psi^* \hat{H} \psi \, dv}{\int \psi^* \psi \, dv} \tag{2.7}$$

which leads to the secular equation

$$\det(H_{ij} - ES_{ij}) = 0, \tag{2.8}$$

where $H_{ij} \equiv \langle \Phi_i \mid \hat{H} \mid \Phi_i \rangle$, and $S_{ij} \equiv \langle \Phi_i \mid \Phi_j \rangle$. The secular equation 2.8 is then solved for the energy and the associated linear equations yield the values of the coefficients c_i in Eq. 2.6.

2.2.4 Configuration Interaction Singles (CIS)

The *configuration interaction singles* (CIS) (also known as Tamm-Dancoff) is a simple and computationally inexpensive method for modelling excited electronic states of molecules and molecular complexes [62]. The methodology used can be described briefly in the following way. The geometry of the molecule is optimized for the ground electronic state. Then, a single-determinant SCF MO, Φ_0, is calculated for the gound electronic state at the already optimized geometry. As it was shown above, the so-obtained SCF MO wave function contains also vacant orbitals. This allows for the CIS wave variational function ψ_i to be presented as a linear combination of singly excited occupied orbitals:

$$\psi_{\text{CIS}} = \sum_{i,j} c_{ij} \psi_i^j, \tag{2.9}$$

where ψ_i^j designates that the occupied spin-orbital i is repalaced by the vacant spin-orbital j. The ψ_{CIS} function is repalced in the secular equation whose roots are an approximation to the energy of the excited electronic states at the given geomtry. It has been shown, however, that the CIS method yields poor approximation to the excited state energy but it can model accurately the geometric structure and the vibrational frequencies of electronically excited states [63].
It is worth to draw the attention to the following important difference between the ordinary CI and the CIS calculations. While in the ordinary CI calculations the reference function is the one of the respective state under consideration, in the CIS method the reference function for the calculation of an excited state is the one of the ground state, and it does not appear as a component in the linear decomposition of the ψ_{CIS}. This is an important issue since the ψ_{CIS} function for the excited state and the ground-state reference function Φ_0 are orthogonal and this precludes the excited-state calculations from relaxing to the ground electronic state.

2.2.5 The Møller-Plesset Perturbation Theory

The Møller-Plesset (MP) perturbation theory [64] is a particular case of the many-body perturbation theory when the interelectronic repulsion is treated as a perturbation to the interaction energy between the nuclei and the electrons of a molecular system. The first practical applications of the MP theory came to the scene only in 1975 with the work Pople and co-workers [65]. Nowadays, it is widely used for accurate modelling of molecules and molecular complexes, and it is of particular significance when electron correlations must be accounted for. The overview presented below is restricted only to closed-shell ground-state molecules. For practical reasons, the spin-orbitals, rather than the spatial orbitals, are used. For spin-orbitals, the HF equations for electron m in an n-electron molecule have the form

$$\hat{f}(m)u_i(m) = \epsilon_i u_i(m) \tag{2.10}$$

The spin-orbital Hamiltonian can be cast in the following form

$$\hat{f}(m) \equiv -\frac{1}{2}\nabla_m^2 - \sum_i \frac{Z_i}{r_{mi}} + \sum_{j=1}^{n}[\hat{j}_j(m) - \hat{k}_j(m)]. \tag{2.11}$$

$\hat{j}$ and $\hat{k}$ are the Coulomb and the exchange operators, respectively . They are defined as

$$\hat{j}_j(\alpha)f(\alpha) = f(\alpha)\int \mid \phi_j(\beta) \mid^2 \frac{1}{\mathbf{r}_{\alpha\beta}}\, dv_\beta \tag{2.12}$$

$$\hat{k}_j(\alpha)f(\alpha) = \phi_j(\alpha)\int \frac{\phi_j^*(\alpha)f(\beta)}{\mathbf{r}_{\alpha\beta}}\, dv_\beta \tag{2.13}$$

In both definitions above, the integration is performed over the whole space, f is an arbitrary function, and α and β label the electrons. The Coulomb operator shows the interaction of electron α with the spread-out charge of electron β. The exchange operator does not have an intuitive physical meaning. It originates from the condition of of the wave function upon the exchange of two electrons.

It can be proved that the sum of the zeroth- and first-order energies equals the HF energy. That is why, the first significant improvement in the MP energy is introduced through the inclusion of the second-order energy correction. For a comprehensive discussion on the matter, the reader is referred to Levine's textbook on quantum chemistry [56]. The second-order correction to the energy is

$$E_0^{(2)} = \sum_{s \neq 0} \frac{| \langle \psi_s^{(0)} | \hat{H}' | \Phi_0 \rangle |^2}{E_0^{(0)} - E_s^{(0)}} \tag{2.14}$$

where the summation is performed over the excitation of the zeroth-order wave function, i. e., single, double, etc. excitations.

2.2.6 The Coupled-Cluster Method

The *coupled-cluster* (CC) method was invented in 1958 by Coester and Kümmel. A nice discussion on this method can be found in [65]. The fundamental equation the coupled-cluster method is founded on is,

$$\psi = e^{\hat{T}} \Phi_0 \tag{2.15}$$

In this formula, ψ is the exact nonrelativistic ground-state molecular electronic wave function, and Φ_0 is the normalized ground-state HF function. The exponential operator is presented by its taylorization,

$$e^{\hat{T}} \equiv 1 + \hat{T} + \frac{\hat{T}^2}{2!} + \frac{\hat{T}^3}{3!} + \cdots = \sum_{k=0}^{\infty} \frac{\hat{T}^k}{k!} \tag{2.16}$$

$\hat{T}$ is referred to as a *cluster operator*, and $\hat{T} = \hat{T}_1 + \hat{T}_2 + \cdots + \hat{T}_n$, where n stands for the number of electrons in the molecule. Only the low-order cluster operators are of practical importance. The two most commonly used cluster operators are the *one-particle excitation* operator, $\hat{T}_1$, and the *two-particle excitation* operator, $\hat{T}_2$, which are defined as

$$\hat{T}_1 \Phi_0 = \sum_{a=n+1}^{\infty} \sum_{i=1}^{n} t_i^a \Phi_i^a \tag{2.17}$$

$$\hat{T}_2 \Phi_0 = \sum_{b=a+1}^{\infty} \sum_{a=n+1}^{\infty} \sum_{j=i+1}^{n} \sum_{i=1}^{n-1} t_{ij}^{ab} \Phi_{ij}^{ab} \tag{2.18}$$

In the above definitions, Φ_i^a, and Φ_{ij}^{ab} designate singly-, and doubly-excited Slater determinants, where the occupied spin-orbital u_i is replaced by the vacant orbital u_a, and the occupied spin-orbitals u_{ij} are replaced by the vacant orbitals u_{ab}, respectively. The coefficients t_i^a, and t_{ij}^{ab} are named *amplitudes*. The goal of a CC calculation is to find the amplitudes. It is worth pointing

out that two important approximations are present in the CC calculations: *i*) the basis set is not infinite but has some finite number of members included; *ii*) only the first couple of terms in the cluster-operator expansion are considered. Theory shows that the main contribution to $\hat{T}$ is provided by $\hat{T}_2$, and hence the approximation

$$\hat{T} \approx \hat{T}_2 \tag{2.19}$$

is justified. With the approximations made, the ground-state wave function ψ becomes

$$\psi_{CCD} = e^{\hat{T}_2}\Phi_0 \tag{2.20}$$

Coupled-cluster methods provide very accurate treatment of electron correlations, but they are also quite computationally expensive, and hence are applied predominantly to small and medim-sized molecules.

2.3 Density-Functional Theory

Density-functional theory (DFT) emerged in 1964 with the Hohenberg-Kohn theorem [66]. The theorem states that the ground-state energy, E_0, the wave function, and all molecular properties are uniquely determined by the the electron probability density. Mathematically, this means that the ground-state energy is a functional of the *electron density distribution*, ρ_0. The latter depends on the three spatial coordiantes x, y, and z.

$$E_0 = E_0[\rho_0(x, y, z)] \tag{2.21}$$

This relation between the molecular properties in the ground state and the electron probability density lays the ground for the development of the DFT. The approach of the DFT is to derive ground-state molecular properties from the electron probability density.
In the DFT the potential nuclei create on electrons is considered as an external potential since it comes from outside the electron system. It is clear that the ground-state energy depends on the types of the nuclei and on their configuration, hence the electronic ground-state energy can be presented in the following manner

$$E_0 = E_v[\rho_0] = \int \rho_0(\mathbf{r})v(\mathbf{r})\,d\mathbf{r} + \overline{T}[\rho_0] + \overline{V}_{ee}[\rho_0] = \int \rho_0(\mathbf{r})v(\mathbf{r})\,d\mathbf{r} + F[\rho_0] \tag{2.22}$$

The index v shows that the energy depends on the nuclear potential, and F is a functional that depends on the average kinetic energy of the electrons and on the interelectronic interactions, but it does not depend on the external potential. This result as a stand-alone does not have any practical application since the functional $F[\rho]$ and the probability distribution are unknown. To harness Eq. 2.22 for practical needs, Hohenberg and Kohn have proven the following theorem. Let be given a trial electron probability density, $\rho_{\text{tr}}(\mathbf{r})$, that obeys the relations $\int \rho_{\text{tr}}(\mathbf{r})\, d\mathbf{r} = n$ (n is the total number of electrons in the molecular system), and $\rho_{\text{tr}}(\mathbf{r}) \geq 0$. For every trial probability density ρ_{tr}, the following inequality holds

$$E_0 = E[\rho_0(\mathbf{r})] \leq \mathbf{E_v}[\rho_{\text{tr}}(\mathbf{r})], \tag{2.23}$$

where ρ_0 is the true molecular electron probability density. The inequality can be also reenunsiated that the true molecular electron probability distribution minimizes the energy functional $E_v[\rho_{\text{tr}}(\mathbf{r})]$. This theorem is a step ahead towards the practical implementation of the DFT since it claims that in principle all ground state molecular properties descend from the electron density distribution but, it still does not provide a recipe on *how* to do that. The practical aspect of the problem was resolved by Kohn and Sham [67]. Many functionals have been proposed for F, and they have proved themselves to be efficient in describing a great variety of molecular systems. The most typical and widely used functional is the B3LYP one [68].

2.4 Molecular Mechanics

The *molecular mechanics* (MM) method is not a quantum mechanical method. It treats molecules as a system of atoms held together by ellastic bonds characterized by force constants, and obeying the equations of classical mechanics. On the basis of the force constants, the molecular energy and the vibrational frequencies are calculated. This method is computationally cheap, and hence sometimes provides a good starting point to quantum-mechanical calculations.

2.5 Molecular Geometry

2.5.1 Equilibrium Geometry

Finding of the *equilibrium geometry* of a molecule is one of the major goals of the theoretical calculations. The equilibrium geometry of a molecule represents the arrangement of the atomic nuclei that minimizes the molecular energy, E, including also the internuclear repulsions. The task of finding the equilibrium geometry becomes more challanging with the increase of the

molecular size. The problem is aggravated by the fact that polyatomic molecules have very many degrees of freedom, and often several different atomic arrangements may result in a similar molecular energy, which poses very stringent requirements on the accuracy of the energy calculations.

2.5.2 Potential Energy Surface

The geometrical structure of a molecule is uniquely determined by defining $3N$-6 independent coordinates, where N stands for the number of atoms in the molecule. As mentioned in the preceding section, the energy of a molecule depends on the atomic configuration. That is why, it is convenient to present the molecular energy, E, as a function of the $3N$-6 independent coordinates. This will result to a hypersurface (*potential energy surface* (PES)) in the $3N$-6-dimensional space. It can be formally written as $E = -E(\mathbf{r})$. The minima on this surface correspond to *stable-equilibrium* structures of the molecule. The lowest-energy minimum is referred to as the *global minimum* . All other minima are called *local minima*. The potential-surface maxima correspond to *unstable-equilibrium* structures that relax to the nearest minimum. There are also points on the PES corresponding to minima for $3N$-7 coordinates, and to a maximum for one coordinate. Such points are referred to as *saddle points*. The calculation of the energy at a fixed conformation is called a *single point* energy calculation .
The set of the *dihedral angles* about all bonds in a molecule defines its *conformation*. The conformation corresponding to an energy minimum (local or global) is termed a *conformer* . The larger the molecule, the bigger the number of conformers it has. That is why, the prediction of molecular conformers is one of the major goals of the theoretical calculations.

2.5.3 Geometry Optimizations

A *geometry optimization* or *energy minimization* is the procedure of finding the molecular conformation correscponding to an energy minimum in vicinity of some initially defined molecular geometry (conformation). From the view point of mathematics, this is the problem of the multidimensional optimization. There exist various algorithms to handle the problem. The most efficient ones are the *gradient method* , the *Newton-Raphson method*, the *steepest-descend method*, etc. To find different molecular conformers, one has to probe different starting geometries, and locally search for the energy minimum. The problem is aggravated in molecules with many internal degrees of freedom, which may have many different conformers. The finding of the global energy minimum is not a trivial task, and in general, this problem has not been solved yet. The guess of the starting conformation in the vicinity of which the global energy minimum is expected might be misleading since often it may happen that the most stable conformer (this is the conformer

corresponding to the global energy minimum) is rather unconventional. This necessitates the development of algorithms for global optimization.

2.5.4 Conformational Search

Many algorithms have been invented to treat the problem of the global optimization though, none of them can provide a complete reliability. For this reason, sometimes, a combination of different algorithms is used to solve a particular problem. The general name of these algorithms is *global optimizers*. In the following, they are listed without presenting the details on how they work. A comprehensive survey of these techniques can be found in [56].

- **Systematic (grid) search method.**. This is one of the commonly used techniques for global-energy-minimum search. This method samples the PES with a certain step and at each sample point it calculates the single point energy. For practical reasons usually only a few molecular coordianes are scanned (most typically dihedral angles), while the other coordinates are kept fixed at their initial values. Then a local seacrh is applied to the lowest-energy sample point. In this way the global energy-minimum can be found.
- **Random (Stochastic or Monte Carlo) search method.**
- **Distance-geometry method.** In this method the molecule is described as a distance matrix whose elements, d_{ij}, are the distances betwee atoms i and j.
- **Genetic algorithm.** This method is described in detail in Sec. 6.3 in conjunction with the analysis of highly resolved molecular spectra.
- **Molecular dynamics search.**
- **Metropolis (Monte Carlo) method.**
- **The diffusion-equation method.**
- **The low-mode conformational search.**

2.6 Molecular Vibrational Frequencies

The conformational search and the geometry optimization of a molecule provide the electronic energy of this molecule. Since, however, atomic nuclei are never at rest but perform small oscillations about their equilibrium positions, it is of importance to calculate also the molecular vibronic frequencies.
The energy of a harmonic oscillator E_{vib} is

$$E_{\text{vib}} = \left(v + \frac{1}{2}\right)h\nu \tag{2.24}$$

where v stands for the vibrational quantum number that can take on values from 0 to infinity, and ν is the vibrational frequency. The vibrational energy corresponding to $v = 0$ is known as the *zeroth vibrational energy* . For a $3N$-atomic molecule there are $3N$-6 vibrational modes if the molecule is not planar, and $3N$-5 modes if the molecule is linear. Each of the modes has a frequency ν_n, which is called a *fundamental ferequency* . In the harmonic approximation, the total vibrational energy of a molecule is the sum of the vibrational energies of all vibrational modes presented as indiviadual harmonic oscillators

$$E_{\text{vib}} = \sum_{n=1}^{M}\left(v_n + \frac{1}{2}\right)h\nu_n, \tag{2.25}$$

where $M = 3N - 6$ in the general case, and $M = 3N - 5$ for linear molecules. The sum of all the zeroth vibrational energies yields the the so-called *zero-point vibrational energy* (ZPVE). This is the lowest energy level a molecule can occupy for a certain conformer. In practice, the fundamental vibrational frequencies of a $3N$-atomic molecule are determined through the *mass-weighted force-constant matrix elements* . Force constants are also called *Hessians*,

$$F_{ij} = \frac{1}{\sqrt{m_i m_j}}\left(\frac{\partial^2 U}{\partial x_i \partial x_j}\right) \tag{2.26}$$

The real treatment of molecules requires also the inclusion of anharmonic corrections. The methodology is desribed in very detail by Wilson, Decius, and Cross [69].

2.7 Programme Packages for Theoretical Molecular Investigations

Various commercial programmes for modelling of molecular structures and properties, and theoretical investigation of molecular phenomena are available nowadays. One of the most proliferated programme packages is GAUSSIAN [70]. It has been used also to provide the theoretical results in this work. Other, also powerful, programmes are MOLPRO [71], TURBOMOL [72], GAMESS (General Atomic and Molecular Electronic Structure System), Q-CHEM, which is optimized for calculation of large molecules containing several hundred atoms, JAGUAR, ACES II, CADPAC, SPARTAN.

Chapter 3

Interaction between Light and Matter

Spectroscopy deals with *transitions* between states in atoms and molecules actuated by an external electromagnetic field (light, in the case of laser spectroscopy). The studied quantum systems (atoms or molecules) start from some stationary state, and as a result of the interaction with the light, they end up in some other stationary state. Quantum transitions are described by the time-dependent *Schrödinger equation*

$$i\hbar\frac{\partial\psi(q,t)}{\partial t} = [\hat{H}]\psi(q,t), \tag{3.1}$$

where q designates the $3N$ spatial and the N spin coordiantes of a system consisting of N particles, and t is time. The Hamiltonian of the joint system molecule-electromagnetic wave can be presented as the sum of the isolated-molecule Hamiltonian $H^{(0)}$ and the Hamiltonian describing the interaction between the molecule and the external field H_{int} (the lower-case index 'int' stands for 'interaction'), i. e.

$$\hat{H} = \hat{H}^{(0)} + \hat{H}_{\text{int}}(t) \tag{3.2}$$

As seen from Eq. 3.2, the interaction Hamiltonian depends on time. It can be shown [73, 74] that the time-dependent wave function $\psi(q,t)$ can be expanded in terms of the time-independent (stationary-state) wave function corresponding to Hamiltonian $\hat{H}^{(0)}$,

$$\psi(q,t) = \sum_i a_i(t)\psi_i(q) \tag{3.3}$$

After some standard mathematical trasformations, and bearing in mind that the stationary-state wave functions $\psi_i(q)$ are orthonormal, constitute a complete basis, and Eq. 3.2 can be transformed

into its equivalent form,

$$\frac{dc_m}{dt} = -\frac{i}{\hbar}\sum_n c_k e^{i\omega_{mn}t}\langle\psi_m^{(0)} \mid \hat{H}_{\text{int}} \mid \psi_n^{(0)}\rangle, m = 1, 2, 3, ... \tag{3.4}$$

where

$$\omega_{mn} \equiv \frac{E_m^{(0)} - E_n^{(0)}}{\hbar} \tag{3.5}$$

Eq. 3.4 is solved on the basis of the theory of perturbations. The interaction Hamiltonian is treated as a perturbation to the molecular Hamiltonian. If the perturbation is applied to the molecule at the time $t = 0$ in stationary state n then at $t = 0$, $\psi(q, 0) = \psi_n(0)$, and from Eq. 3.3, it can be inferred that $c_n(0) = 1$, and $c_i(0) = 0$, for $i \neq n$. Assuming also that the perturbation is small and acts for short time from $t = 0$ to $t = t_1$, it is reasonable to infer that $\frac{dc_m}{dt}$ is also small, and hence the coefficient c_m is obtained as

$$c_m(t_1) = -\frac{i}{\hbar}\int_0^{t_1} e^{i\omega_{mn}t}\langle\psi_m^{(0)} \mid \hat{H}_{\text{int}} \mid \psi_n^{(0)}\rangle\, dt \tag{3.6}$$

where $c_m(0) = \delta_{mn}$. The probability for the system to commute from the initial quantum state n into a new state m is given by $\mid c_m(t) \mid^2$. This formula is the onset for the derivation of the famous Fermi's golden rule [75], which calculates the transition rate (probability of transition per unit time) from a certain energy eigenstate of a quantum system into a continuum of eigenstates, caused under the action of perturbation. This rule applies when there is no depletion of the initial-state population. Fermi's golden rule has the form

$$T_{n\to f} = \frac{2\pi}{\hbar}\delta(E_f - E_n) \mid \langle f \mid \hat{H}_{\text{pert}} \mid n\rangle \mid^2 \rho \tag{3.7}$$

In the formula above n is the initial state, f designates the continuum of states, and ρ shows the density of the destination states.

Formula 3.6 is irrelevant of the nature of the perturbation applied. The interaction of light with quantum systems is rationalized in the frame of the *semiclassical theory*, wherein light is treated as an electromagnetic wave. The interaction between light and atoms/molecules can be viewed upon as an interaction between an electromagnetic wave and the dipole it induces in molecules. This is the so-called electric dipole approximation . The interaction $\hat{H}_{int}$ has the form

$$\hat{H}_{int} = -\boldsymbol{\mu} \cdot \mathbf{E}(t) \tag{3.8}$$

$\mathbf{E}(t)$ represents the electric-field vector as a function of time. It is convenient to represent a time-varying electric field as a supeposition of plane-polarized waves with different frequencies, ω_i, time-dependent amplitudes, $f_i(t)$, and planes of polarization $\mathbf{e}$. The expansion in terms of plane waves is described by the next formula

$$\mathbf{E}(t) = \sum_{i=1}^{\infty} \mathbf{e}_i f_i(t) e^{-i\omega_i t} \tag{3.9}$$

On the basis of formulae 3.6 and 3.7, the following important for spectroscopy conclusions can be drawn.

- An optical transition is possible only when the energy of the photon equals the energy difference between the two levels, n and m. This is the so-called *resonance condition*.
- If the resonence condition is met, the intensity of the transition depends on the matrix element $|\langle\psi_m^{(0)} \mid \hat{H}_{\text{int}} \mid \psi_n^{(0)}\rangle|^2$. There are two cases when a transition may be resonance-allowed but the intensity of the transition may be zero, or very small. *i*)When the interaction Hamiltonian H_{int} is very small due to the small induced dipole moment $\boldsymbol{\mu}$ the above matrix element is also small. *ii*) Because of molecular-symmetry considerations, the matrix element may vanish even in cases when the induced dipole moment is not zero. This lays the ground for the establishment of *selection rules*, i. e., there are *allowed* and *forbidden* transitions [73]. The particular selection rules that apply to rotationally resolved spectroscopy are discussed in Chap. 4.

Chapter 4

Molecular Quantum Mechanical Characteristics and Molecular Structure

Molecules are complex quantum-mechanical objects. For the understanding of their structures and properties, the entangled interactions between their constituents have to be explained. The Hamiltonian of a molecule with *m* nuclei and *n* electrons is

$$\hat{H} = \hat{H}_{\mathrm{N}} + \hat{H}_{\mathrm{E}} + \hat{H}_{\mathrm{NN}} + \hat{H}_{\mathrm{EE}} + \hat{H}_{\mathrm{NE}} \tag{4.1}$$

In this formula $\hat{H_{\mathrm{N}}}$ is the kinetic energy of the nuclei, $\hat{H_{\mathrm{E}}}$ is the kinetic energy of the electrons, $\hat{H_{\mathrm{NN}}}$ is the interaction energy of the nuclei, $\hat{H_{\mathrm{EE}}}$ stands for the inetarction between the electrons, and the last term describes the interaction between the nuclei and the electrons.
The substitution of the above Hamiltonian into the equation!Schrödinger (see Chap. 3), and the solution of the latter, in principle, yields all the information on the energy levels and wave functions of this molecule. Due to the complicated form of the Hamiltonian, however, the so-produced Schrödinger equation does not render itself to a direct solution. That is why, some reasonable assumptions have to be made in order to make the solution tractable.

4.1 Born-Oppenheimer Approximation

The most straightforward and widely-used approximation, when treating molecules quantum-mechanically, is the *Born-Oppenheimer approximation* [76]. Electrons are *ca*. 2000 times lighter than protons/neutrons. This means that for a small to medium-sized molecule containing several tens of atoms, the ratio between the mass of the electrons and that of the nuclei is in the range $10^{-3} - 10^{-5}$. Due to the higher, mass nucleons are intrinsically more inert than electrons, and

hence their response to forces is slower. This implies that at every instant of time the electrons in a molecule experience a static potential created by the nuclei. Thus, the electronic wavefunction reacts adiabatically to any change in the nuclear configuration, i. e., the nuclear configuration is ”encoded” in the electronic wave function. Actually, the equilibrium configuration of the atomic nuclei in a molecule is the one that yields minimum of the sum of the energies resulting from the interaction between the nuclei, E_{NN}, between the electrons, E_{EE}, and between the nuclei and the electrons, E_{NE}. The binding of atoms to form a molecule brings forth the electronic energy of a molecule, E_{el}. The atomic nuclei in a molecule oscillate about their equilibrium positions, so these oscillations have vibrational energy, E_{vib}. Molecules also rotate with rotational energy, E_{rot}. When considering molecular properties, the overall translation of the molecule is irrelevant, and hence it is omitted.
Thus, the Born-Oppenheimer approximation states that the electronic motions, the vibrations, and the rotations of a molecule can be treated separetaly, and the total energy of a molecule (excluding its translational component) is the sum of its electronic (the potential that keeps the atoms bound together), vibrational, and rotational energies:

$$E = E_{\mathrm{el}} + E_{\mathrm{vib}} + E_{\mathrm{rot}} \tag{4.2}$$

There is a relation between the magnitudes of the electronic, vibrational, and rotational energies:

$$E_{\mathrm{rot}} \approx \sqrt{\frac{m}{M}} E_{\mathrm{vib}} \approx \frac{m}{M} E_{\mathrm{el}} \tag{4.3}$$

The energies differ by two-three orders of magnitude from each other. It is seen also that the electronic energy constitutes the largest contribution to the total energy.
It is important to point out that the Born-Oppenheimer approximation is not always valid. There are cases which cannot be described correctly within this approximation. Such cases are referred to as the Born-Oppenheimer approximation break-down. Typical examples of the Born-Oppenheimer approximation break-down are the vibration-rotation interaction through the Coriolis coupling [77], or the interaction between the electronic wave functions and the vibrations, which is known as the Herzberg-Teller effect [78].

4.2 Rotation of Molecules

The analysis and interpretation of rotatianally resolved molecular spectra necessitates cognizance of the theory of the molecular rotation. This theory relates in an elegant way the structure of molecules with their rotational spectra.

4.2.1 Molecular Rotational Energy

If one assumes that the interatomic distances in a molecule are fixed to some *vibrationally averaged* values, then the molecule can be treated as a rigid body and hence the energy levels corresponding to its overall rotations can be calculated. The assumption of rigidity is well justified in many cases. When, however, this assumption fails due to molecular distortions, the latter are accounted for by an explicit inclusion of *distortion coefficients*.
Every rigid molecule is characterized by its *tensor of inertia* $\hat{I}$ [79, 80]

$$\hat{I} = \begin{pmatrix} I_{xx} & I_{xy} & I_{xz} \\ I_{yx} & I_{yy} & I_{yz} \\ I_{zx} & I_{zy} & I_{zz} \end{pmatrix} \tag{4.4}$$

The matrix elements are defined in the following way

$$I_{xx} \equiv \sum_i m_i(y_i^2 + z_i^2) \qquad \text{etc.}, \qquad I_{xy} \equiv \sum_i m_i x_i y_i \qquad \text{etc.} \tag{4.5}$$

where x_i, y_i, and z_i are the coordinates of atom i with respect to an arbitrary coordinate system, and m_i is the atomic mass. When this tensor is diagonalized (all off-diagonal elements I_{xy} become zeros), it yields the three principal moments of inertia , designated as I_a, I_b, and I_c, about the three principal axes of inertia, a, b, and c, respectively. The principal axes of inertia are labelled so that to produce the inequality

$$I_a \leq I_b \leq I_c \tag{4.6}$$

With respect to their principal moments of inertia molecules can be divided into four groups.

- **Spherical top.** $I_a = I_b = I_c$, for instance CH_4
- **Prolate symmetric top.** $I_a < I_b = I_c$, for instance CH_3Br. Linear molecules constitute a particular case of prolate symmetric tops when $I_a = 0$ and $I_b = I_c$. All diatomic molecules belong to this class of molecules.
- **Oblate symmetric top.** $I_a = I_b > I_c$,
- **Asymmetric top.** $I_a \neq I_b \neq I_c$

The rotational kinetic energy Hamiltonian of a rigid molecule can be expressed through its tensor of inertia and angular velosity

$$\hat{H}_{\text{rot}} = \frac{1}{2} I_{ij} \omega_i \omega_j \tag{4.7}$$

In the principal coordinate system, the rotations about the three principal axes of inetria are decoupled and the total rotational kinetic energy becomes the sum of the rotational kinetic energies about the three axes

$$\hat{H}_{\text{rot}} = \frac{1}{2}(I_a \omega_a^2 + I_b \omega_b^2 + I_c \omega_c^2) = A P_a^2 + B P_b^2 + C P_c^2 \tag{4.8}$$

The coefficients A, B, and C are called *rotational constants*, and obey the inequality $A \geq B \geq C$. They are inversely proportional to the moments of inertia, and are defined by the expressions

$$A = \frac{\hbar^2}{2I_a} \qquad B = \frac{\hbar^2}{2I_b} \qquad C = \frac{\hbar^2}{2I_c} \tag{4.9}$$

As will be shown in the subsequent chapters, rotational constants play an important role in the analysis of rotationally resolved spectra, and the assignement of molecular structures on the basis of spectroscopic data. The quantities P_α, $\alpha = a, b, c$, are the angular momenta of the molecule relative to its principal axes of inertia.

4.2.2 Molecular Rotational Energy Levels

To obtian the energy levels of a rigid molecule, it is convenient to represent the quantum-mechanical Hamiltonian through the angular momenta of the molecule as shown in the last equality of Eq. 4.8. Several important properties and relations of the rigid-molecule angular momenta are highlighted in the following. The detailed derivation of these properties and relations can be found, for instance, in [73, 81, 82]. Let XYZ be a space-fixed coordinate system with its origin in the centre of mass of the molecule, and abc be the coordinate system of the principal axes of inertia of the molecule. Then the following relations between the projections of the squared angular momentum, $\hat{P}^2$, onto the axes X, Y, and Z, and a, b, and c, and the rotational Hamiltonian H_{rot} hold

$$\hat{P}^2 = \hat{P}_a^2 + \hat{P}_b^2 + \hat{P}_c^2 = \hat{P}_X^2 + \hat{P}_Y^2 + \hat{P}_Z^2 \tag{4.10}$$

$$[\hat{P}_X, \hat{P}_Y] = i\hbar\hat{P}_Z \qquad \text{etc.} \tag{4.11}$$

$$[\hat{P}_a, \hat{P}_b] = -i\hbar\hat{P}_c \qquad \text{etc.} \tag{4.12}$$

$$[\hat{P}^2, \hat{P}_c] = 0 \qquad \text{etc.} \tag{4.13}$$

$$[\hat{P}^2, \hat{P}_Z] = 0 \qquad \text{etc.} \tag{4.14}$$

$$[\hat{P}_Z, \hat{P}_c] = 0 \qquad \text{etc.} \tag{4.15}$$

$$[\hat{H}_{\text{rot}}, \hat{P}^2] = 0 \qquad \text{etc.} \tag{4.16}$$

$$[\hat{H}_{\text{rot}}, \hat{P}_Z] = 0 \qquad \text{etc.} \tag{4.17}$$

It can be shown that for every rotor, there exist some fundamental relations

$$\hat{P}^2\psi = J(J+1)\hbar^2\psi, \qquad J = 0, 1, 2, ... \tag{4.18}$$

$$\hat{P}_Z\psi = K\hbar\psi, \qquad K = 0, \pm1, ..., \pm J \tag{4.19}$$

where $\sqrt{J(J+1)}\hbar$ is the magnitude of the total rotational angular momentum and $K\hbar$ is its component along a space-fixed axis.
The energy levels for the different types of moleculs, spherical top, symmetric top, and asymmetric top, are listed below.

Spherical-Top Energy Levels

$$E = AJ(J+1) \tag{4.20}$$

where $A = B = C$ is the rotational constant of the molecule.

Symmetric-Top Energy Levels

$$E(J,K) = BJ(J+1) + (C-B)K^2 \qquad \text{oblate top} \tag{4.21}$$

$$J = 0, 1, 2, ... \qquad K = 0, \pm1, \pm2, ..., \pm J$$

$$E(J,K) = BJ(J+1) + (A-B)K^2 \qquad \text{prolate top} \tag{4.22}$$

$$J = 0, 1, 2, ... \qquad K = 0, \pm1, \pm2, ..., \pm J$$

$$E = BJ(J+1) \qquad \text{linear} \tag{4.23}$$

As seen from the above formulae, the rotational energy of symmetric tops depends not only on J but also on a second quantum number, K, which determines the projections of the total angular momentum along a molecule-fixed axis of the symmetric top.

Asymmetric-Top Energy Levels

The formulae for the energy levels of asymmetric-top molecules are quite complicated, and the energy levels can be obtained analytically only for small values of J. For large values of J, the energy levels are calculated numerically. An important parameter in the analysis of asymmetric rotors is the *Ray's asymmetry parameter* , defined as

$$\kappa = \frac{2B - A - C}{A - C} \tag{4.24}$$

This parameter shows the deviation of the particular asymmetric top from either the prolate or the oblate symmetric top. The energy levels of an asymmetric top are, usually, designated as $J_{K_{\rm pr}K_{\rm ob}}$, where $K_{\rm pr}$ and $K_{\rm ob}$ designate the the values of K for the prolate and oblate symmetric tops, respectively, that correlate with the asymmetry-top level under consideration. It is important to emphasize, however, that $K_{\rm pr}$ and $K_{\rm ob}$ are not true quantum numbers for the asymmetric top. An alternative notation for the asymmetric energy levels is J_τ, where $\tau = K_{\rm pr} - K_{\rm ob}$.
The following table (taken from Ref. [80]) shows the analytical solutions for the first few energy levels of an asymmetric top.

$J_{K_{\rm pr}K_{\rm ob}}$	$\tau = K_{\rm pr} - K_{\rm ob}$	$E(J, K_{\rm pr}, K_{\rm ob})$
0_{00}	0	0
1_{10}	1	$A + B$
1_{11}	0	$A + C$
1_{01}	-1	$B + C$
2_{20}	2	$2A + 2B + 2C + 2\sqrt{(B-C)^2 + (A-C)(A-B)}$
2_{21}	1	$4A + B + C$
2_{11}	0	$A + 4B + C$
2_{12}	-1	$A + B + 4C$
2_{02}	-2	$2A + 2B + 2C - 2\sqrt{(B-C)^2 + (A-C)(A-B)}$

Table 4.1: *Rigid asymmetric-top energy levels*

4.2.3 Electric Dipole Transition Moment

It is proved [73] in the electric dipol approximation (see Chap. 3) that the transition probability of a molecule from state n to state m under the action of plane-polarized (in the x direction) monochromatic light with electromagnetic energy density u_x at frequency ν_{mn} for a time T is

$$| c_{mn}(T) |^2 = 2\pi\hbar^{-2}T \mid \langle m \mid \hat{\mu}_x \mid n\rangle \mid^2 u_x(\nu_{mn}) \tag{4.25}$$

In the above equation μ_x is the x component of the molecular dipole moment. The matrix element $| \langle m \mid \hat{\mu}_x \mid n\rangle |$ can be written in the more general form

$$| \langle m \mid \hat{\mu} \mid n\rangle |^2 = | \langle m \mid \hat{\mu}_x \mid n\rangle |^2 + | \langle m \mid \hat{\mu}_y \mid n\rangle |^2 + | \langle m \mid \hat{\mu}_z \mid n\rangle |^2 \tag{4.26}$$

where $\hat{\mu} = \mathbf{i}\hat{\mu}_x + \mathbf{j}\hat{\mu}_y + \mathbf{k}\hat{\mu}_z$. $\mid \hat{\mu}\rangle$ is called *transition dipole moment* or *transition moment*. The transition moment is a vector quantity, and it is usually defined with respect to the principal axes of inertia of the molecule. Depending on whether the transition dipole moment is oriented along the the a, b, or c principal axis of inertia, one distinguishes between three types of transitions, $a-$, $b-$, and $c-$type.

4.2.4 Selection Rules

Not all transitions between the energy levels of an asymmetric top are possible. One-photon transitions are allowed only for transitions for which $\Delta J = 0, \pm 1$. In a set of transitions those for which $\Delta J = -1$ form the P branch, those for which $\Delta J = 0$ give rise to the Q branch, and $\Delta J = +1$ form the R branch. For two-photon transitions, the selection rules are different from those for one-photon transitions. In this case $\Delta J = -2, +2$, corresponding to O and S branches [83].

4.2.5 Transition Intensity

Transition intensities are determined by statistical weights depending on the degeneracy in the quantum number K, nuclear spin, the polarization of the light inducing the transition, and on the thermal distribution of the species given by the Boltzmann formula

$$exp\left(-\frac{\Delta E_{mn}}{kT_{\text{rot}}}\right) \tag{4.27}$$

where ΔE_{mn} is the energy difference between levels m and n, k is the Boltzmann constant , and T is the rotational temperature .

4.2.6 Deviations from the Born-Oppenheimer Approximation

The discussion hitherto was on rigid molecules obeying the Born-Oppenheimer approximation (see Sec. 4.1). Sometimes, however, these approximations break down, and one has to eleborate different models to treat the molecular behaviour properly. The most typical deviations from the above approximations are listed here.

- **Centrifugal distortion.** When considering high values of J, molecular bonds stretch and hence molecules can be no longer treated as rigid objects. In this case, their rotational energy levels are calculated by including in the respective rigid-molecule-approximation formulae a correction for the centrifugal distortion expressed by centrifugal distortion constants [73, 81]
- **Coriolis coupling.** The Coriolis coupling in molecules results from the coupling between the molecular vibrations and the overall rotation of the molecule. The Coriolis-coupling correction in the Born-Oppeheimer approximation is introduced through the theory of perturbations.
- **Herzberg-Teller effect.** The Herzberg-Teller effect [78] is the gain of intensity by an electronically forbidden but vibronically allowed transition from another both electronically and vibronically allowed transition through vibrational coupling.
- **Jahn-Teller effect.** If at a certain symmetrical nonlinear nuclear configuration of a polyatomic molecule, two electronic states are degenerate, the latter can be lifted by some nuclear distortion. The splitting of the electronic degeneracy by a nuclear distrosion accompanied by the interaction between the rotation-vibration levels of the two electronic states is referred to as the Jan-Teller effect [84].

4.3 Rotational Constants and Structure of Molecular Species

From the rotationally resolved spectroscopy one can derive the values of molecular rotational constants, which are related to the principal moments of inertia of the studied species. Unfortunately, rotational constants do not provide unique information on the molecular structure since it may happen that different structures may have very similar rotational constants. That is why, it is necessary to find a method to assign structures on the basis of the experimentally observed rotational constants.

Molecular structures are determined by defining the interatomic distances, planar, and dihedral angles . Regarding bond lengths, the following bond-length definitions have to be distinguished [80].

- r_e is the bond legth that corresponds to a hypothetic vibrationless state of the molecule.
- r_0 is the effective bond length corresponding to a ground-state vibtation. It is these distances that are involved in the measured rotational constants.
- r_s is the bond length corresponding to an isotopic substitution. The so-defined bond length is discussed in conjuction with the Kraitchman equations [85]
- $\langle r \rangle$ is an averaged bond length corresponding to some atom positions resulting from partial correction to the vibrational effects.
- r_m is the mass-weighted bond length derived from the averaging of the bond lengths of a large number of isotopically substituted species.

Kraitchman equations [80, 85, 86] are a convenient analytical tool for determining the coordinates of an isotopically substituted atom in a rigid molecule with respect to the center-of-mass (COM) principal axis system of the parent molecule (the molecule before the isotopic substitution). Kraitchman equations allow the coordinates of the substituted atom to be found on the basis of the measured rotational constants for the particular molecular species before and after the isotopic substitution. This approach has been successfully applied to the analysis of many noble-gas clusters of benzene (Bzn) and benzene derivatives [87–89]. The coordinates of an isotopically substituted atom with respect to the principal-axis system of the parent molecule are calculated by the formulae

$$
\begin{aligned}
|\, x \,| &= \sqrt{\frac{\Delta P_x}{\mu}\left(1 + \frac{\Delta P_y}{P_y - P_x}\right)\left(1 + \frac{\Delta P_z}{P_z - P_x}\right)} \\
|\, y \,| &= \sqrt{\frac{\Delta P_y}{\mu}\left(1 + \frac{\Delta P_z}{P_z - P_y}\right)\left(1 + \frac{\Delta P_x}{P_x - P_y}\right)} \\
|\, z \,| &= \sqrt{\frac{\Delta P_z}{\mu}\left(1 + \frac{\Delta P_x}{P_x - P_z}\right)\left(1 + \frac{\Delta P_y}{P_y - P_z}\right)}
\end{aligned}
\tag{4.28}
$$

where μ is the reduced mass of the molecular species

$$
\mu = \frac{M \Delta m}{M + \Delta m} \tag{4.29}
$$

M is the mass of the molecule before the isotopic substitution, and Δm is difference of the masses before the substitution.

P_x, P_y, and P_z in Eq. 4.3 are defined as

$$\begin{aligned} P_x &= \frac{1}{2}(-I_x + I_y + I_z) \\ P_y &= \frac{1}{2}(-I_y + I_z + I_x) \\ P_z &= \frac{1}{2}(-I_z + I_x + I_y) \end{aligned} \tag{4.30}$$

I_x, I_y and I_z designate the principal moment of inertia of the unsubstituted molecule. Differences Δ of parameter P in Eq. 4.3 are defined as

$$\begin{aligned} \Delta P_x &= P'_x - P_x \\ \Delta P_y &= P'_y - P_y \\ \Delta P_z &= P'_z - P_z \end{aligned} \tag{4.31}$$

The primed parameters in the above definitions correspond to the molecular species after the isotopic substitution.

Part II

Spectroscopic Investigation of Molecular Systems

Chapter 5

The Concept of Spectroscopy

Spectroscopy provides information on the quantum-mechanical energy levels of physical systems. It is an efficient experimental tool for the investigation of molecular structure and dynamics. Over the years, spectroscopy has diversified, and nowadays, there exists a great variety of spectroscopic techniques [3, 13, 22, 43, 90–96]. It is difficult that all spectroscopic techniques be encompassed and described in detail. This chapter aims at providing a general overview of the existing advanced spectroscopic methods that are relevent to the investigation of weak molecular interactions, molecular conformations, cluster patterns, and molecular ionization and fragmentation. Their advantages and drawbacks are briefly discussed along with the main realms of their applicability.

5.1 Survey on Molecular Spectroscopy Techniques

For weak interactions to be studied, it is important that the model systems (molecules or molecular complexes) should be isolated and unperturbed by external influences. There are several methods to produce isolated molecular species.

- **Molecular beams.** A convenient and powerful method for production of molecular species in the gas phase is the *supersonic jet expansion* [11, 14, 97–103]: the studied species are entrained in some carrier gas (usually He, Ne, Ar), and the mixture is expanded through a pulsed nozzle into vacuum, thus yielding a *cold molecular beam*. The cooling process compells the species to occupy the lowest-energy conformations; thereupon only the most stable conformations can be experimentally identified. An additional phenomenon stemming from the adiabatic cooling is the formation of weakly bound clusters [11, 14, 101].

The details on the supersonic molecular jet expansion are presented in the next chapter.

- **Matrix isolation.** Matrix isolation is an experimental technique used to embed molecular species in an unreactive matrix [104, 105]. Usually the guest sample is diluted in the matrix host material and the so-produced mixture is cooled down to less than 10 K. Thus, the studied species is trapped in the matrix formed by the condensed host material. Most frequently, noble gases and nitrogen are used as host materials. The matrix isolation technique was suggested in 1954 by Pimentel and co-workers [104], and since that time, it has developed as one of the techniques employed to isolate molecules and molecular complexes. It has been applied also to the investigation of biologically relevant molecules [106].
- **Helium droplets.** An advanced technique for the investigation of molecular conformations is the spectroscopy in heluim droplets [107–110]. It is an alternative to the collisional cooling in supersonic jet expansions [111]. The studied molecular species is embedded in a helium droplet that provides an isothermal environment achieved by evaporative cooling down to 0.37 K (^{4}He droplets), or 0.15 K (^{3}He droplets) [110]. Because of the superfluidity of helium at these low temperatures, the helium-droplet environment mimics the gas-phase conditions, but at very low temperature. The helium-droplets technique has been shown to be a promising technique for the exploration of even large biologically significant molecules [112].

For convenience, the spectroscopic techniques that have been elaborated to study isolated molecular species can be devided into several categories [13]: electronic [13, 113], near-infrared [114, 115], far-infrared [116, 117], microwave [118], Raman [119, 120], rotational coherence [119, 121, 122], gas electron diffraction [123], zero electron kinetic energy (ZEKE) [124], mass analysed threshold ionization (MATI) [125].

5.2 Molecular Electronic Spectroscopy

5.2.1 UV Laser Induced Fluorescence

In the UV *laser induced fluorescence* (LIF) experiments, the molecules are excited from their ground electronic state to an excited electronic state. Then the total fluorescence is measured. Through scanning the frequency of the excitation laser, one can chart the excited-state energy levels. Depending on the excitation-laser resolution, LIF spectroscopy may be *low-resolution* (laser linewidth $\Delta\nu \geq 0.05$ cm^{-1} FWHM (Full Width at Half Maximum)) allowing for distinguishing single vibrational bands or rotational band contours in the first excited electronic state [126–129], and *high-resolution* (laser linewidth $\Delta \leq 0.005$ cm^{-1} (FWHM)) resolving single rotational lines or clumps of rotational lines. Low-resolution LIF experiments are routinely

conducted in many laboratories. They employ pulsed excitation . High-resolution UV LIF experiments are more sophisticated, and, in order to achieve high spectral resolution, the excitation is performed by continuous-wave (cw) laser light. Such experiments are carried out by Pratt and co-workers [130–136], and Meerts and co-workers [137–141]. LIF spectroscopy is a sensitive technique but it lacks mass selectivity, and hence spectra originating from different molecular species in the cold molecular beam may overlap and impede the analysis of the so-obtained results.

5.2.2 UV Resonance Enhanced Multiphoton Ionization

The UV *resonance-enhanced multiphoton ionization* (REMPI) spectroscopy can be also two types, low- and high-resolution. This technique has been used to obtain the results presented in this work; therefore it is very coprehensively described in the next chapter.

5.2.3 Spectrosopy of Resolved High Rydberg States

The spectrosopy of high-lying Rydberg states [142, 143] is important for the understanding the behaviour of highly excited molecules, and it paves the way to the investigation of molecules and molecular complexes in the ionic state. Employing a specially developed fitting technique [143], one can obtain the Rydberg series limits. The spectroscopy of high Rydberg states has been applied to various molecules and molecular complexes [144–146].

5.2.4 Zero Kinetic Energy (ZEKE) and Mass Analysed Threshold Ionization (MATI) Spectroscopies

Both *zero electron kinetic energy* (ZEKE) and *mass analysed threshold ionization* (MATI) spectroscopies explore the energy levels in the cation. They exploit the same fundamental principles but differ in the type of the detected particles. After ionization, ZEKE spectroscopy detects electrons, whilst MATI detects ions. For charting the energy levels in the cationic state, however, the frequency scan alone does not suffice: increasing the frequncy of the ionization laser pulses leads only to higher kinetic energy of the ejected electrons. That is why, an additional parameter besides the laser frequency must be also fixed. This parameter is the kinetic energy of the ejected electrons. The underlying idea in ZEKE and MATI spectrosopies is that every cationic state is the limit of a converging Rydberg series of neutral states. Thus, a selective excition of high Rydberg states, followed by a pulsed-filed ionization results in spectrally resolved energy levels

of the cation. ZEKE spectroscopy came to existence in 1984 with the work of Schlag, Müller-Dethlefs, and Sander [147, 148], and it has been applied to many molecular systems [149–151]. MATI spectroscopy has the advantage of mass selectivity. This technique emerged in 1991 with the work of Zhu and JohnsonS [125, 152]. It has provided valuable information on the structure and properties of various molecular monomers and complexes in their ionic state [153–156].

5.2.5 Double Resonance Spectroscopy

Double resonance spectroscopy is a technique that allows for the separate identification of distinct molecular conformations or isomers in the cold molecular beam or can be used also to study the vibrational dynamics in liquids [3, 157–159]. There are two types of double resonance spectroscopy: *UV-UV hole-burning*, and *IR-UV ion-depletion*. In the former, two UV lasers are used, one probe laser whose frequency is fixed to a certain transition from the ground electronic state to a vibrational level in the excited electronic state, and a second, UV ”burn”, laser whose frequency is scanned across the vibrational spectrum of the excited electronic state. The probe laser is delayed relative to the ”burn” laser. Thus, transitions originating from the species that brings forth the transition the probe laser is tuned to will burn out its population in the ground state and this will bring about intensity drops in the signal originating from the probe laser. When the UV-UV hole-burning spectrum is compared with the REMPI spectrum, the vibronic bands associated with different species are discriminated. UV-UV hole-burning experiments have been used to distinguish between different conformations of small biological molecules [160–162]. The other alternative to the UV-UV hole-burning spectroscopy, the IR-UV one, employs also two lasers, one IR ”burn” laser which is fixed to a certain vibrational transition in the ground electronic state, and a second, UV probe, laser whose frecuecy is scanned across the vibrational levels of the excited electronic state. The IR ”burn” laser depopulates the ground state of only one of the species in the cold molecular beam; thereby, the electronic transitions associated with this species will be greatly reduced or removed from the LIF/REMPI spectrum [13, 163–165].
A type of double resonance spectrosscopy is also the coherent ion-dip spectroscopy [142, 166]. It is more important from the view point of molecular dynamics rather than for determination of molecular structures.

5.3 Near- and Far-Infrared Laser Spectroscopy

Near-infrared (near-IR) spectroscopy is used to measure the vibrational spectra of molecules and molecular complexes. Infrared lasers with optical parametric oscillators (OPOs) and frequency mixers are used as tuneable light sources [40, 167, 168]. The spectra are measured by monitoring the depletion of the fluorescence [169, 170] or the ionization [40] signal as a function of

the frequency of the IR laser. Important improvements in the sensitivity of the near-IR spectrosopy have been brought by IR absorption in slit jets [171, 172] and *cavity ring-down* (CRD) spectroscopy [173–176]. Slit jets are used to increase the interaction path between the molecular species and the laser beam/pulses. Cavity ring-down spectroscopy is an absorption spectrosopy with very high sensitivity. It is not affected by fluctuations in the laser-source intensity because it measures the absorption rate rather than the absorption magnitude of light pulses travelling back and forth between two plano-concave mirrors forming a high-Q cavity. Since the light pulses in the cavity traverse through multipassing enormous distance (several kilometers), even very small absorptions can be readily detected.
The *far-infrared* (far-IR) spectroscopy covers the spectral range 20-150 cm^{-1}. It is also referred to as a *vibration-rotation tunnelling spectroscopy* since its main application area is the investigation of the transitions between vibration-rotation tunnelling states. This technique was pioneered by Saykally [177], and successfully applied by Winnewisser and co-workers [178].

5.4 Microwave Spectroscopy

Microwave spectroscopy plays a very important role in structural assignments since it provides very accurate rotational and distrorsion constants of the studied species [80]. It has been used to study isolated molecules [179–181] and molecular complexes [182, 183]. The assignment of molecular structures, however, is not straightforward since usually the parameters needed to unambiguously assign the molecular structure are more than the data provided by microwave spectroscopy. This warrants microwave spectroscopy to be combined with other techniques. Another limitation of microwave spectroscopy is that it can investigate molecular species only in their ground electronic state.

5.5 Raman Spectroscopy

Notwithsatnding *Raman* spectroscopy is applied to the condensed phase rather than to the gas phase, it is listed here because it is a source of important information on the low-frequency vibrational modes of molecules in a solution. It uses a laser to excite the molecules and the subsequent Stokes or anti-Stokes emission is detected [119, 120].

5.6 Rotational Coherence Spectroscopy

Rotational coherence (RC) spectroscopy was invented by Zewail and co-workers [121]. It yields the moments of inertia of freely rotating molecular species from the measurements of their characteristic rotational times. The so-measured moments of inertia in conjunction with theory can provide information on the molecular structure. The characteristic rotational times are measured by a pump-probe spectroscopy. A linearly polarized pump laser pulse excites all species whose transition dipole moments are aligned parallel to the laser polarization. Some time after the excitation the initial alignment breaks due to the different characteristic rotational times of the different species. The initial alignment, however, recurs after a certan time period that depends on the rotational constants. This characteristic time period is probed by a second time-delayed laser pulse [119, 122]. This technique has been demonstrated to yield rotational constants which, along with theoretical predictions, can be used for the assignement of molecular structures [184].

5.7 Gas Electron Diffraction

The *gas electron diffraction* is a particular case of the electron diffraction [123]. It is applied for the determination of molecular structures in the gas phase. The electron diffraction pattern is a fingerprint of the molecular structure, i. e., from the observed electron diffraction pattern one can reconstruct the molecular structure that brings it forth. The physics behind this technique is based on the wave-particle duality nature of electrons. What is recorded is the total scattering intensity, which depends on the electron momentum transfer, i. e., the difference between the momentum vector of the impingent electron beam and that of the scattered one. The electron momentum transfer consists of an atomic and molecular component. The former does not display any structure. The molecular component, however, has a pattern which results from the interference between the spherical electron waves scatterred from the individual atoms building up the molecules of the studies species. Thus, the molecular structure is encoded in the interference pattern and hence can be worked back once the interference pattern is known. It is worth to point out that for large molecules the determination of their structures only on the basis of gas electron diffraction measurements is not always straightforward; it is often necessary in such cases, information from other types of spectroscopy to be adduced [185].

Chapter 6

Resonance Enhanced Two-Photon Ionization Spectroscopy in Molecular Beams

S. Chervenkov, P. Q. Wang, R. Karaminkov, T. Chakraborty, J. E. Braun, and H. J. Neusser Proc. SPIE **5830**, 246 (2005).

High-resolution Doppler-free resonance enhanced two-photon ionization (R2PI) spectroscopy with mass selection of jet-cooled (2-12 K) molecular species is renowned as a powerful experimental technique for studying of isolated molecules and molecular complexes in the gas phase. It allows rotationally resolved (FWHM = 70 MHz) spectra of the vibronic bands of the $S_1 \longleftarrow S_0$ electronic transition of the studied molecular systems to be measured at their mass channel. The so-obtained spectra are analysed by a specially designed computer-assisted fitting routine based on genetic algorithms and thus accurate rotational constants in the ground, S_0 and the first excited, S_1 electronic state, respectively, and the transition moment ratio of the observed species can be determined.

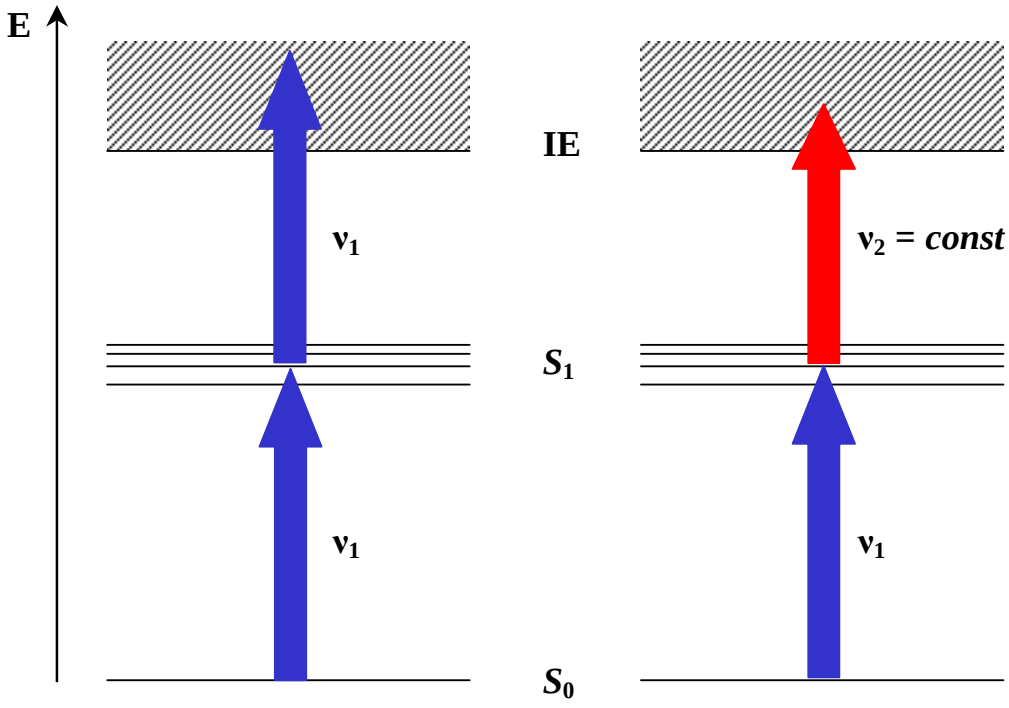

Figure 6.1: *Resonant two-photon ionization (R2PI) scheme.*

6.1 Resonance Enhanced Two-Photon Ionization (R2PI) UV Laser Spectroscopy

UV R2PI spectroscopy of jet-cooled molecular species explores the transitions between the electronic ground, S_0, state and the first excited, S_1, state. All of the studied molecular systems are produced at low rotational temperature via supersonic jet expansion. The R2PI technique employs one excitation photon to promote the molecules from their ground, S_0, electronic state to the first excited, S_1, electronic state and a second photon to ionize them. The energy scheme is presented in Fig. 6.1.

There are two types of R2PI experiments: one-colour (see Fig. 6.1a) and two-colour (see Fig. 6.1b). In the first type, two photons with the same energy (ν_1) from a single light source are used both for the excitation and ionization steps. The drawback of this scheme is that when scanning a broad region in the S_1 electronic state, the total photon energy ($2\nu_1$) may exceed the dissociation energy in the ion and thus lead to an undesired fragmentation of the studied species, especially in case of weakly bound complexes. This shortcoming is overrun by using a two-colour ionization scheme, in which one photon with energy ν_1 is employed to excite the molecules from their elec-

tronic ground state to the first excited electronic state and a second photon with a constant energy ($\nu_2 = const$) is used to ionize the already excited molecules. The energy of the excitation photon is scanned and the one of the ionization photon is fixed to a value which exceeds (typically 100 cm^{-1}) the ionization limit but is below the dissociation energy of the cluster ion. The excitation and the subsequent ionization occur only if the resonance condition is fulfilled (see Eq. 6.1).

$$\Delta E = h\nu_1 = E_n - E_m \tag{6.1}$$

With respect to the linewidth of the scanned laser, R2PI spectroscopy may be *low-* and *high-resolution*. The low-resolution R2PI spectroscopy is used to find the position of the vibrational transitions, and the high-resolution spectroscopy yields the rotational structure of the respective vibronic bands.

6.2 Experimental Set up

The experimental set up comprises three functional units: vacuum equipment with pulsed heatable nozzle for production of jet-cooled molecular species [11, 101, 102] and a coupled time-of-flight mass spectrometer with an ion detector, a laser system for low- and high-resolution spectroscopy, and a data acquisition system. They are described in detail in the following subchapters.

6.2.1 Cold Supersonic Molecular Beams

The supersonically jet-cooled molecules and molecular complexes are produced by adiabatic expansion through a pulsed nozzle into vacuum. The vacuum chamber consists of two differentially pumped subchambers: a forechamber and an interaction chamber (see Fig. 6.2).

The forechamber contains the pulsed nozzle, and the cold molecular beam is produced there. It is evacuated by a turbomolecular pump (Balzers TPU 2200, 3200 l/s) maintaining vacuum in nozzle-nonoperating regime of 9.10^{-9} mbar. When the nozzle is operating, the pressure can increase up to 5.10^{-5} mbar. The interaction chamber is connected to the forechamber through a skimmer with a clearance of 1.5 mm, through which the molecular beam passes. The interaction chamber is the place where the interaction between the molecules and the laser pulses takes place. It is also the receptacle of the time-of-flight mass spectrometer. The vacuum in this subchamber is produced by a turbomolecular pump (Balzers TPU 510, 510 l/s). On two of the opposite walls of this subchamber, there are quartz windows that transmit the counterpropagating UV laser pulses.

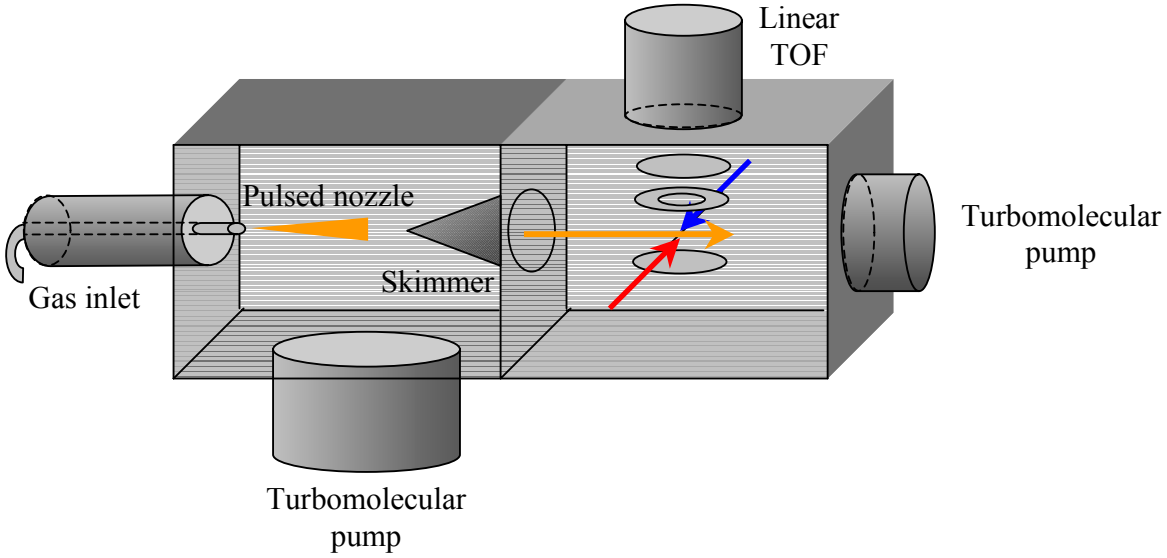

Figure 6.2: *Schematic view of the molecular-beam set up and the time-of-flight mass spectrometer set up.*

The cold molecular beam [11, 101, 102] is produced by expansion of the investigated species entrained in a carrier gas through a heatable (up to 120° C) nozzle with an orifice diameter of 300 μm. The sample is contained in a small cup inside the nozzle, just before the orifice. This allows for the vapours of the sample to mix with the carrier gas prior to the expansion. The container can be heated and the temperature can be maintained stable (within 0.5° C) by a programmable electronic thermocontroller (Hengstler Grado 901). Solvent molecules (such as water, acetylene, methanol, etc.) can be introduced together with the buffer gas. In this case, the buffer gas is mixed with the solvent molecules in a metal cylinder. In this way, the partial pressure of the two components (buffer gas and solvent) can be precisely controlled (within several mbar). The so-obtained gas mixture is supplied to the nozzle where it homogenizes with the investigated species. The carrier gas is usually Ar since it favours the collisional cooling due to its large atomic mass. Ne can also be used, though the cooling process in this case is not very efficient. The stagnation pressure of the carrier gas inside the nozzle is typically in the range 2-4 bar. The molecular beam is laced through a conical skimmer (see Fig. 6.2). The skimmer position is fixed but the nozzle position is adjustable so that the nozzle to-skimmer distance can be optimized as a trade-off between the ion signal intensity and the Doppler broadening. Table 6.1 (Taken from [36]) presents the Doppler broadening at a skimmer orifice diameter of 1.5 mm as a function of the buffer gas and the nozzle-to-skimmer distance.

Usually, the Doppler broadening is reduced down to 40-50 MHz. The ions produced as a result of the interaction between the molecular beam and the laser pulses are mass selected with a homebuilt [186, 187] linear Wiley-McLaren [188] time-of-flight (TOF) mass spectrometer (see

Carrier gas	Nozzle-to-skimmer distance mm	Doppler broadening MHz / cm^{-1}
Ne	50	85 / 0.0028
Ne	100	40 / 0.0013
Ar	50	60 / 0.0020
Ar	100	30 / 0.0010

Table 6.1: *Doppler broadening at a skimmer orifice diameter of 1.5 mm as a function of the carrier gas and the nozzle-to-skimmer distance. For comparison, the Doppler broadening of C_6H_6 in a gas cell at room temperature is 1600 MHz (0.053 cm^{-1}) [36].*

Fig. 6.2). The ion optics of the spectrometer consists of three elements (deflectors), which create an electric field deflecting the ions from the initial straight trajectory of the molecular beam in a direction perpendicular to the plane defined by the molecular beam and the path of the laser pulses. Thus, the ions are targeted at the detector, which is on top of the interaction chamber. The deflector comprises two regions: the ion extraction region and the ion steering region. The laser-generated ions are extracted by the electric field created between the *repeller plate* (bottom plate in Fig. 6.2), to which a voltage of +300 V is applied, and the *diafragm* (middle ring in Fig. 6.2), to which a voltage of +220 V is applied. The upward trajectory of the extracted ions is corrected by the weaker electric field formed by the diafragm and the *mesh* (grounded) (upper plate in Fig. 6.2). The ions pass through a drift region of 20 cm and then are detected by *microchannel plate*s whose amplification ranges between 10^6 and 10^8. It is well-known that the nonrelativistic kinetic energy of charged particles is proportional to the charge and the potential difference. Mathematically, this relationship is expressed by the equation:

$$\frac{1}{2}mv^2 = eU \tag{6.2}$$

Since the R2PI experiments are concerned with singly ionized molecules and molecular complexes and the applied electric field in the TOF is the same for all ions, the above equation can be recast to demonstrate that the arrival time of the ions at the detector is proportional to the square root of their mass:

$$t \propto \sqrt{m} \tag{6.3}$$

Thus, the measured arrival time can be easily transformed into ionic mass. By using referent molecular systems (e. g. C_6H_6), the proportionality constant has been determined to be 2.70 $\mu s.u^{-2}$.

6.2.2 Laser System

The laser equipment encompasses two functional laser units, presented schematically in Fig. 6.3.

- *broadband tuneable dye laser*, which is used as a source both for the excitation and ionization photons in one-colour low-resolution experiments, and as a source for the ionizsation photons in two-colour high-resolution experiments.
- *pulsed amplified narrow-band single-mode continuous wave* (cw) *ring dye laser*, which provides the excitation photons for the two-colour high-resolution measurements.

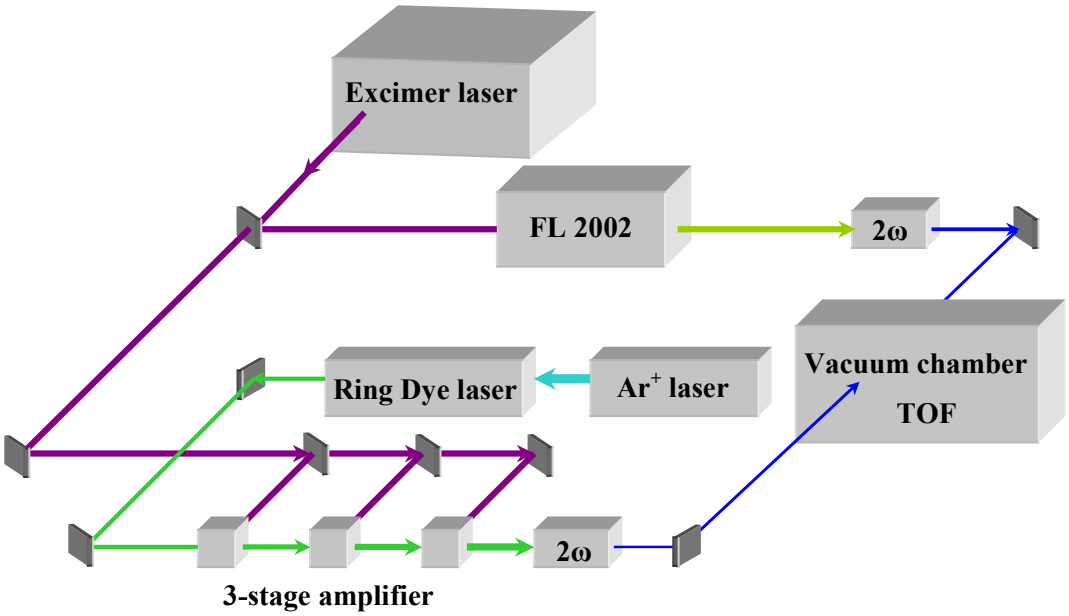

Figure 6.3: *Schematic representation of the laser system for low- and high-resolution resonance enhanced two-photon ionization experiments.*

Ionization Laser

The ionization photons are produced by frequency doubling in abeta-barium-borate (BBO) or potassium-dihydrophosphate (KDP) crystal of the output pulses of a commercial tuneable broadband dye laser (Lambda Physik FL2002) with a linewidth of 0.4 cm^{-1} (FWHM) . This laser has an *oscillator* and an *amplifier*. The frequency tuning is performed by tilting of a diffraction grating, which plays also the role of a high-reflective rear mirror of the oscillator. Both oscillator and amplifier are pumped transversely by a XeCl excimer laser (Lambda Physik EMG 203 MSC) generating pulses at 308 nm with an energy of 230 mJ and duration of *ca.* 18 ns (FWHM). The

frequncy-doubled dye laser pulses have an energy of the order of 1 mJ. The so-produced UV laser pulses pass through a telescopic system before they enter the vacuum chamber. This allows for the laser spot size at the interaction point with the molecular beam to be controlled.

Single Mode cw Ring Dye Laser

The narrow-band single-mode cw laser is a ring dye laser (COHERENT CR-699-21) operating with Rhodamine 6G for the range between 550 and 610 nm, and with Coumarin 521 for the range between 510 and 550 nm. It generates cw laser beam with a bandwidth of 2 MHz and an output power ranging from 200 to 500 mW, depending on the pump laser power and the dye used. Single seamless scans within 30 GHz (1 cm^{-1}) are routinely performed. The pump source for the ring laser is an Ar^+ ion laser (COHERENT INNOVA 400) operating at its strongest lines at 488 nm (for Rhodamine 6G) and 514 nm (for Coumarin 521). The pump power varies between 4 W and 6 W.

Pulsed Amplification

Pulsed amplification was invented by Hänsch and Wallenstein [189, 190], first realized by Salour [191], and applied to molecular spectroscopy by Riedle et *al*. [192]. The output of the single-mode ring laser is pulsed amplified in a three-stage homebuilt amplifier. The latter consists of three dye cells. The seeding cw beam goes through the three cells where it is transversely amplified by the pulses of the excimer laser described above (see Sec. 6.2.2). The energy of the excimer-laser pulses is not distributed evenly at the three cells but in proportion 10:20:70 starting from the first one. There are pinholes and interference filters down the seeder beam path to prevent generation of amplified spontaneous emission . The so-amplified high-resolution laser pulses are coupled into a (BBO / KDP) for *second harmonic generation* (SHG). The frequency doubled pulses are nearly Fourier [193–195]. Their frequency bandwidth is *ca*. 70-100 MHz, pulse duration 18-20 ns and maximum energy 0.5-1.0 mJ. They are then laced through a telescopic system, similar to the one used for the broadband laser pulses (see Sec. 6.2.2), prior to being steered into the vacuum chamber (see Sec. 6.2.1 and Fig. 6.2) where they counterpropagate with the pulses from the broad-band dye laser and overlap with them in space and time at the crossing point with the molecular beam.

Frequency Measurement and Relative Calibration

The absolute frequency of the spectra is measured automatically with a wavemeter (ATOS 007), which is characterized by a precision of $\Delta\nu/\nu=10^{-8}$ and absolute frequency measurement of

0.003 cm^{-1}. The relative calibration of the high-resolution spectra is performed by simultaneous recording of the fringe pattern of a confocal Fabry-Perot interferometer whose free spectral range is 150.09590 MHz.

6.2.3 Control of the Experiment. Data Acquisition System

For the laser pulses and the cooled molecules to arrive simultaneously at the interaction point, the opening of the nozzle and the excimer laser pulse generation must be concerted. The coordination is realized by a master trigger that sends trigger pulses to the nozzle controller (it can control the nozzle opening (typically 50 μs) and hence, the quantitity of the ejected molecular species) and a delay generator (STANFORD RESEARCH SYSTEMS DG 535). The latter determines the time after the nozzle opening at which the excimer laser must produce a shot. This is the time necessary for the ejected from the nozzle molecules to drift the distance from the nozzle to the interaction point with the laser pulses. This delay can be manually controlled and optimized for every particular case. To minimize the effect of the temporal jitter of the excimer laser, its pulses activate a photodiode, which serves as a trigger setting time zero for the TOF and the data acquisition system.
The data acquisition system consists of three boxcar integrators (STANFORD RESERCH SYSTEMS SR 280) and a personal computer (PC). The boxcar integrator integrates the ion signal within the specified time gate whose width is usually 50 ns or 100 ns. The signal is digitized and recorded on a PC.
The laser scan (both for low- and high resolution experiments), the recording of the absolute frequency markers, the relative calibration with the Fabry-Perot interferometer, and the data acquisition system are controlled by a homemade software operating in LabVIEW environment.

6.3 Data Analysis of Dense Highly Resolved Spectra: Computer-Aided Rotational Fit Based on Genetic Algorithms

The high-resolution UV spectra of the vibronic bands of large-sized molecules are usually quite congested. They normally feature densely spaced peaks which are formed by aggregation of rotational lines. That is why, the conventional method of single rotational line assignment is not feasible. For the correct interpretation of the experimental data and extraction of relevant scientific information such as rotational constants and transition moment (TM)!ratio, one has to resort to special computer-assisted fitting techniques. There exist several approaches to the fitting of experimental spectra, and all of them employ well-established procedures for finding maxima

in a multidimensional parameter space. They include *simulation annealing*, *downhill simplex method*, *gradient method*, etc. [196]. These methods have been successfully implemented in the analysis of highly resolved spectra of isolated molecules and molecular complexes in the gas phase [197–199]. Usually, they provide very reliable and accurate data on rotational constants, transition moment (TM)!ratio, rotational temperature, etc. in cases when the cross correlation between the experimental and theoretical spectra manifests a prominent maximum. This occurs, mostly, when the experimental spectra are not too dense and exhibit a well-expressed structure. A drawback of these algorithms is that they may adhere to a local maximum and miss the global one, which makes them strongly dependent on the choice of the starting values of the parameters. A step further to overcome this problem, is the development of fitting routines based on *genetic algorithms* (GA), which have been successfully applied to the analysis of highly resolved spectra with densely spaced peaks or with a low signal-to-noise ratio [139, 200–205], and it has been even applied to the high-resolution spectra of pliant biologically relevant molecules and their complexes [201, 205]. A new software package employing genetic algorithms has been developed in our group. The methodology of the computer-aided rotational fitting routine based on genetic algorithms is schematically described in Fig. 6.4.

As an initial step, the program generates several trial solutions based, in most cases, on arbitrary values of the participating parameters. Any trial solution is referred to as an *individual*. Any set of trial solutions is termed *population*. The size of the population, i.e., the number of solutions in a given set, is a free parameter and it can be user-defined. Normally, this number depends on the particular problem and varies between several tens to several hundreds. After a population has been created, there comes the second step, the *evaluation*. The quality can be ranked and a special number called *fitness* is used as an indicator for the quality. Usually, the fitness is normalized and it takes on values in the range between zero and one. As a figure of merit for the quality of the trial solutions is used the comparison of any of the simulated spectra with the experimental one. The comparison is based, usually, either on cross correlation or on least squares fit. Experience shows, however, that cross correlation yields better results. When the spectra are completely different, the fitness tends to zero, and vice versa, when the spectra are very similar, the fitness converges to one. When the quality estimation is over there comes the *selection* step, in which of all initially generated spectra only the fittest ones are selected and subjected to a further treatment. The number of selected and preserved spectra is a free parameter. The selected spectra are allowed to bring forth a new generation through the processes of *reproduction* [200]. This process generates two new solutions; each of them having features from either of the parent ones. Some *mutations* using *random number generator* are applied to the new generation. This operation is necessary since it exploits the whole multidimensional space and prevents clinging of the solution to a local maximum. When the described procedure is repeated iteratively, it ultimately yields the best solution. Very often, it is necessary that the contribution of the peaks in P and R branches, respectively, be emphasized. For this purpose, the experimental spectrum is multiplied by a specially designed weighting function prior to being cross correlated with any

of the synthesized spectra. This approach has turned out to be successful in many cases. To augment the efficiency of the fitting routine, the explored multidimensional volume can be restricted by imposing some constraints to the possible values of the fitted parameters. To enhance the power of this method, in principle, several auxiliary techniques can also be employed [200]. They include *elitism* and *hybridization*. The elitism prevents the best individuals from a certain generation from crossover and mutation and passes them on to the next generation intact. This option increases the efficiency of the global optimization algorithm. The hybridization is a combination of several optimizing strategies depending on the particular optimization problem. The hybridization may considerably enhance the capability of the program when some specific features of the task are utilized.

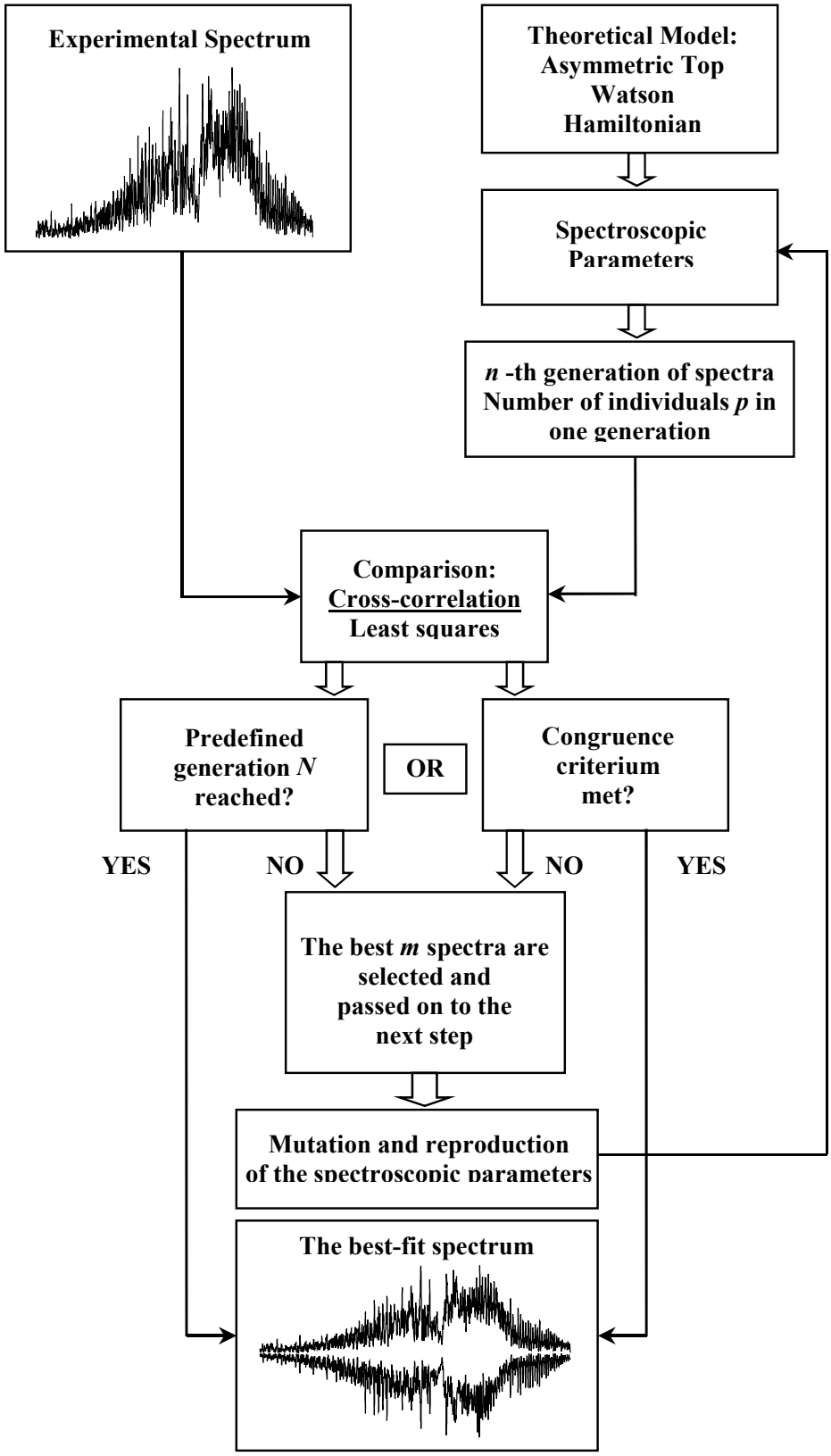

Figure 6.4: *Block diagram of the computer-assisted rotational fit routine based on genetic algorithms.*

Part III

Results and Discussion

Chapter 7

Evidence for a C-H$\cdots\pi$ Type Weak Ineraction: 1:1 Complex of Styrene with Acetylene

S. Chervenkov, P. Q. Wang, J. E. Braun, T. Chakraborty, and H. J. Neusser, Phys. Chem. Chem. Phys. **9**, 837, (2007).

The 1:1 complex of styrene with acetylene has been studied by mass selective low- and high-resolution UV R2PI spectroscopy combined with genetic-algorithm-based computer-aided fit of the spectra with partial rotational resolution and high level ab initio quantum chemistry calculations. Two stable conformeric geometries of the 1:1 complex of styrene with acetylene have been theoretically found: one with acetylene binding to styrene as a proton donor and one with acetylene acting as a proton acceptor. From the analysis of the vibronic structure of the $S_1 \longleftarrow S_0$ spectrum and the fit of the highly resolved spectrum of the 0_0^0 origin band of the complex, it is shown that the favoured conformation is the one in which acetylene binds to the benzene ring of styrene through formation of a nonconventional hydrogen bond of C-H$\cdots\pi$ type with no marked change of the transition moment orientation of styrene. The styrene moiety remains planar and the acetylene molecule is tilted by a small angle of 4° relative to the C_6 symmetry axis of the benzene ring, most likely, due to the reduced symmetry of the benzene ring π electrons rather than to a direct interaction with the vinyl group.

7.1 Introduction

Dimeric molecular complexes which are bound by weak π-hydrogen bonding interactions, a classical prototype of which is the benzene-water mixed dimer, have attracted a lot of attention for spectroscopic investigation in recent years. The species serve as models to investigate the details of the π-hydrogen bonding interaction potentials, which are believed to play a vital role in supramolecular assemblies and crystal engineering [206, 207]. The weakest of this nonconventional hydrogen bonding is the C-H$\cdots\pi$ type, wherein a CH group is the hydrogen bond *donor* [39]. The delicateness of the interaction can be recognized by comparing the acid dissociation constants of alkanes, e.g., the pK_a of methane is 49 [208], with those of conventional hydrogen bond donors, e.g., OH of water (pK_a = 15.74). A recent high level *ab initio* calculation on hydrogen-bonded acetylene-ethane complex, performed by Tsuzuki et *al*. [209], predicts that the binding energy is only 1.82 kcal/mol (629 cm^{-1}). Thus, hardly can the species be distinguished from a typical van der Waals complex and hence can be placed at the borderline of the two categories of interactions. Nevertheless, there are experimental evidences for the existence of such a C-H$\cdots\pi$ hydrogen bond; it is supposed to be important in crystal packing and molecular recognition [39, 210]. The acidity of CH groups is largely enhanced in alkynes e.g., pK_a of acetylene is 25 [208]. Thus, the dimeric complex of acetylene (C_2H_2) with benzene (Bzn) is easily formed in a supersonic jet expansion and the complex has been the subject of several spectroscopic studies in recent years [38, 41, 211, 212]. Fujii et *al*. [41] have recently performed an IR-UV double resonance spectroscopy measurement on the Bzn·C_2H_2 mixed dimeric complex and their results reveal that the antisymmetric C-H stretching vibration of the C_2H_2 moiety exhibits a large red shift (22 cm^{-1}) in the complex and the shift shows a positive correlation with the π-electron density of the phenyl ring, which in turn indicates that the C-H bond of C_2H_2 is bound to the π-electrons of the ring. Quantum chemistry calculations predict that the C_2H_2 moiety is placed on the C_6 axis of the benzene ring and calculated stabilization energy (MP2 calculation extrapolated at the basis set limit incorporating coupled cluster CCSD(T) correction terms) is 2.83 kcal/mol (978 cm^{-1}). In the present study, the vibronically and rovibronically resolved electronic spectra for the $S_1 \longleftarrow S_0$ transition of a 1:1 complex of acetylene (C_2H_2) with styrene (ST) has been measured in a supersonic jet expansion. The goal is to explore how the intermolecular interaction potential, which is manifested in the resolved electronic spectrum, is affected on increasing the *acceptor* π-electron density of the phenyl group by vinyl substitution. The structure and the atom labels of the ST·C_2H_2 complex are shown in Scheme 7.1.

In the case of the 1:1 complex of acetylene with Bzn, the 6_0^1 transition of the latter shows only a single peak in both FE [211] and R2PI spectra [38, 211, 212]. The upper limit of the binding energy of the complex in the S_1 state has been estimated to be 680 cm^{-1} by comparing the dispersed fluorescence spectral features of the complex as a function of the excitation excess energy. In contrast, the R2PI spectrum of the 1:1 Bzn·H_2O complex is complicated because of

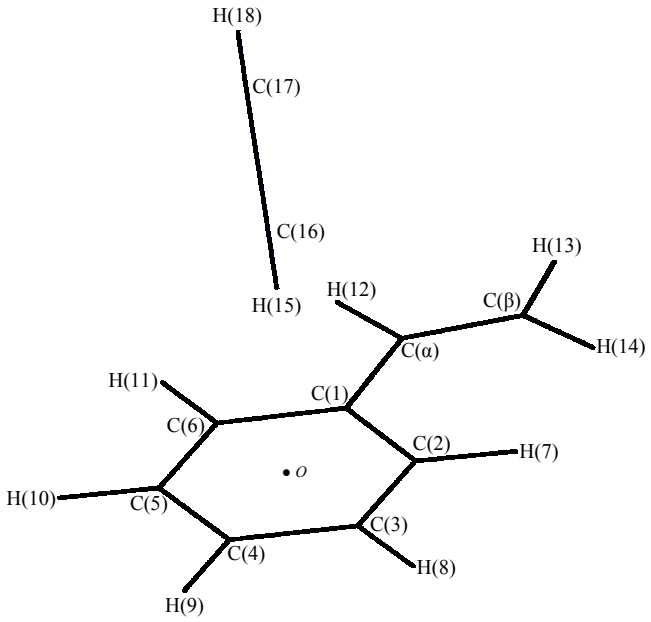

Figure 7.1: *Atom labels of the ST·C_2H_2 complex. O is the geometrical centre of the benzene ring.*

large-amplitude tumbling motion of the water molecule on the surface of the benzene ring [213]. With vinylbenzene (ST) as the hydrogen bond acceptor and H_2O as donor, the one-colour R2PI spectra for the $S_1 \longleftarrow S_0$ transition of the clusters have been measured recently by Mahmoud et *al*. [214]. The signal for the 1:1 complex appears very weak. The 0_0^0 band shows a blue shift of 22 cm^{-1} compared to bare ST, which can be compared with +50 cm^{-1} shift for the Bzn·H_2O 1:1 complex. The large-sized clusters exhibit extensive fragmentation following the two-photon ionization and this behaviour is similar to that of the Bzn·H_2O large-sized clusters.

On the other hand, we have recently shown that on substituting the *para* position of ST by a fluorine atom, the fragmentation channel following the two-photon ionization of the 1:1 ST·H_2O complex is completely blocked and the intensity of the vibronic bands of the 1:1 complex appears to be quite strong [203].

In the present case, there are several possible sites for binding of the C_2H_2 molecule with ST. We have discerned these possibilities using high-resolution spectroscopy. Quantum chemistry calculations at the MP2 and B3LYP level of theory with an extended basis set have been performed to substantiate the experimental results.

7.2 Experiment and Data Processing

The low-resolution spectra of ST and its single and double complexes with C_2H_2, as well as the high-resolution spectra of ST and the ST·C_2H_2 complex have been measured by R2PI spectroscopy with mass selection in a supersonic jet-cooled molecular beam!supersonic using the experimental set up thoroughly descrbed in Sec. 6.2. ST was bought from Fluka with a purity of 96% and used without further purification. No heating was used. The ST vapours were entrained in Ar mixed with C_2H_2 at a backing pressure of 3 bar. The Ar^+ ion laser was operating at 514 nm yielding output power of 4 W necessary to pump the ring dye laser. The latter was using Rhodamine 6G dye achieving an output power of 300 mW.
For the analysis and interpretation of the measured highly resolved spectra of the ST monomer and the ST·C_2H_2 complex, the computer-assisted fitting routine based on genetic algorithms (see Sect. 6.3) has been employed. For the fits of both spectra, 500 generations with 500 individuals in each have been used. The attained best-fit cross correlations are 98% and 95% for the ST monomer and the ST·C_2H_2 complex, respectively.

7.3 Results

7.3.1 *Ab initio* Calculations

Ab initio quantum chemistry calculations both for the styrene monomer and its complex with C_2H_2 have been performed at the MP2 and B3LYP DFT level of theory for the ground, S_0, electronic state, and at CIS for the excited, S_1, electronic state, respectively, with 6-311++G(*d*, *p*) basis set using Gaussian 03 programme package [70]. The structural and inertial parameters of the ST monomer for the ground, S_0, and the first excited, S_1, electronic state, respectively, and the transition moment ratio, are listed in Table 7.1.

To find the energetically most preferred binding sites of C_2H_2 to ST, a grid search with a single point energy calculation was performed for the ground, S_0, electronic state. In this search the position of the C_2H_2 moiety was scanned along two mutually orthogonal circumferences with a common origin located at the centre of the benzene ring thus mapping a sphere around the ST molecule. The azimuthal angle about the long benzene axis, C(1)-C(4), was scanned from 0 to 180° by a step of 20°, and the azimuthal angle about the short axis was scanned from 0 to 360° by a step of 20°. Totally 360 points were explored. The two lowest-energy conformations were selected and subjected to a full structural optimization. The resulting structures include one out-of-plane, herein referred to as Conformer I, and one in-plane, designated as Conformer II. In Conformer I, C_2H_2 is located above the benzene ring of ST in an upright position and acts

Parameter	ST monomer			ST·H_2O					
	S_0		S_1	S_0				S_1	
	MP2	B3LYP	CIS	MP2		B3LYP		CIS	
				I	II	I	II	I	II
-ΔE_e^N	-	-	-	5.03	2.71	0.97	0.39	11.04	10.40
-ΔE_e^B	-	-	-	2.63	1.56	0.24	0.09	-	-
r_1 C(1)-C(α), Å	1.47	1.47	1.40	1.47	1.47	1.47	1.47	1.40	1.40
r_2 C(α)-C(β), Å	1.35	1.34	1.39	1.35	1.35	1.34	1.34	1.39	1.39
r_3 H(15)$\cdots O$, Å	-	-	-	2.37	-	2.86	-	3.16	-
r_4 C(16)$\cdots$H(11), Å	-	-	-	-	2.92	-	3.27	-	3.43
r_5 H(16)$\cdots$H(12), Å	-	-	-	-	2.98-	-	3.54	-	3.49
r_6 C(17)$\cdots$H(11), Å	-	-	-	-	3.03	-	3.34	-	3.50
r_7 H(17)$\cdots$H(12), Å	-	-	-	-	2.95	-	3.62	-	3.51
α_1 C(2)C(1)C(α), deg	121.8	123.2	121.1	121.6	122.4	123.2	123.2	121.1	121.2
α_2 C(1)C(α)C(β), deg	124.8	127.6	124.4	124.2	125.1	127.6	127.6	124.4	124.3
α_3 $n\cdots$C(16)-C(17), deg	-	-	-	32.0	7.0	3.5	7.6	15.8	3.6
τ_1 C(β)C(α)C(1)/C(α)C(1)C(2), deg	-30.1	-0.6	0.0	-32.8	-26.4	0.8	0.6	-0.2	0.0
τ_2 C(α)C(1)C(2)/C(1)C(2)C(3), deg	1.8	0.0	0.0	2.7	2.3	0.0	0.0	0.6	0.0
TM ratio $\mu_a^2 : \mu_b^2 : \mu_c^2$	-	-	100:0:0	-	-	-	-	27:73:0	26:73:1
A, GHz	5.0770	5.1968	4.9674	1.3675	1.7686	1.3517	1.6416	1.3562	1.7484
B, GHz	1.5445	1.5388	1.5986	1.1243	0.7656	0.8188	0.6823	0.7431	0.6539
C, GHz	1.2001	1.1872	1.2094	0.8061	0.5558	0.6344	0.4954	0.5879	0.4887

Table 7.1: *Binding energies and typical geometrical parameters for the ST monomer and the ST·C_2H_2 complex obtained from ab initio calculations for the ground, S_0, and the first excited, S_1, electronic state at the MP2/6-311++G (d, p) and B3LYP/6-311++G (d, p) level of theory, respectively. ΔE_e^N and ΔE_e^B are the binding energies (kcal/mol) without and with countepoise corrections for the basis set superposition error (BSSE), respectively. n stands for the normal to the benzene ring.*

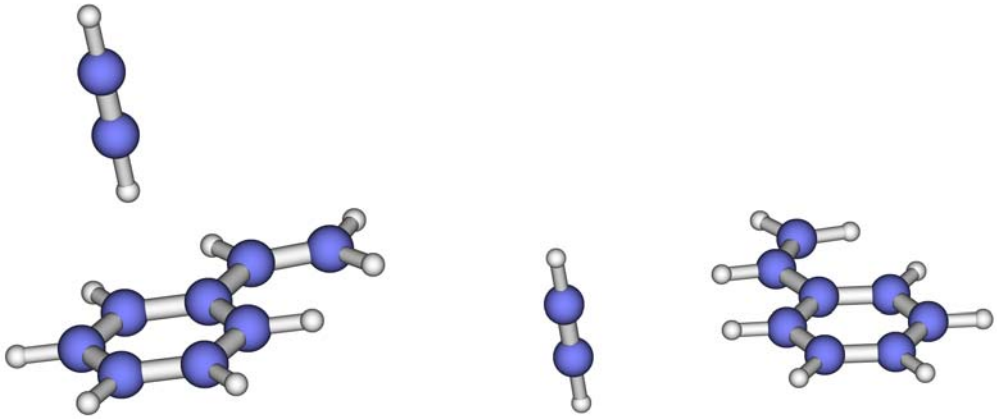

(a) Conformer I (0.0)

(b) Conformer II (0.15 kcal/mol)

Figure 7.2: *Electronic ground state, S_0, structures for the two lowest-energy conformers of the ST·C_2H_2 complex optimized at the B3LYP/6-311++G (d, p) level of theory. The relative energies (kcal/mol) calculated at the same level are given in parentheses. Details and comparison with the MP2/6-311++G (d, p) calculations are presented in Table 7.1.*

as a donor!proton. In Conformer II, C_2H_2 is almost perpendicular to the plane of the benzene ring and binds to the latter sideways, acting as a . (see Fig. 7.2). The most important structural parameters obtained from the geometry optimization both for ground, S_0, and the first excited, S_1, electronic state, respectively, and the binding energy without and with counterpoise correction [215] for the basis set superposition error (BSSE) for the two conformations are summarized in Table 7.1. Conformer II is less stable than Conformer I by 1.07 kcal/mol (MP2) and 0.15 kacl/mol (B3LYP), respectively. For the optimized structures, I and II, in the excited, S_1, electronic state, the vibrational frequencies have been calculated. For Conformer II, however, one negative frequency (-3.4 cm^{-1}) was obtained and though the applied stringent constraints on the energy threshold the negative frequency persisted. This is an indication that most likely the observed structure corresponds to a on a very flat excited state potential surface resulting in a small negative frequency. The frequencies corresponding to the excited state of Conformer I are positive, and they are compared with the observed vibrational bands in the low-resolution spectrum of ST·C_2H_2.

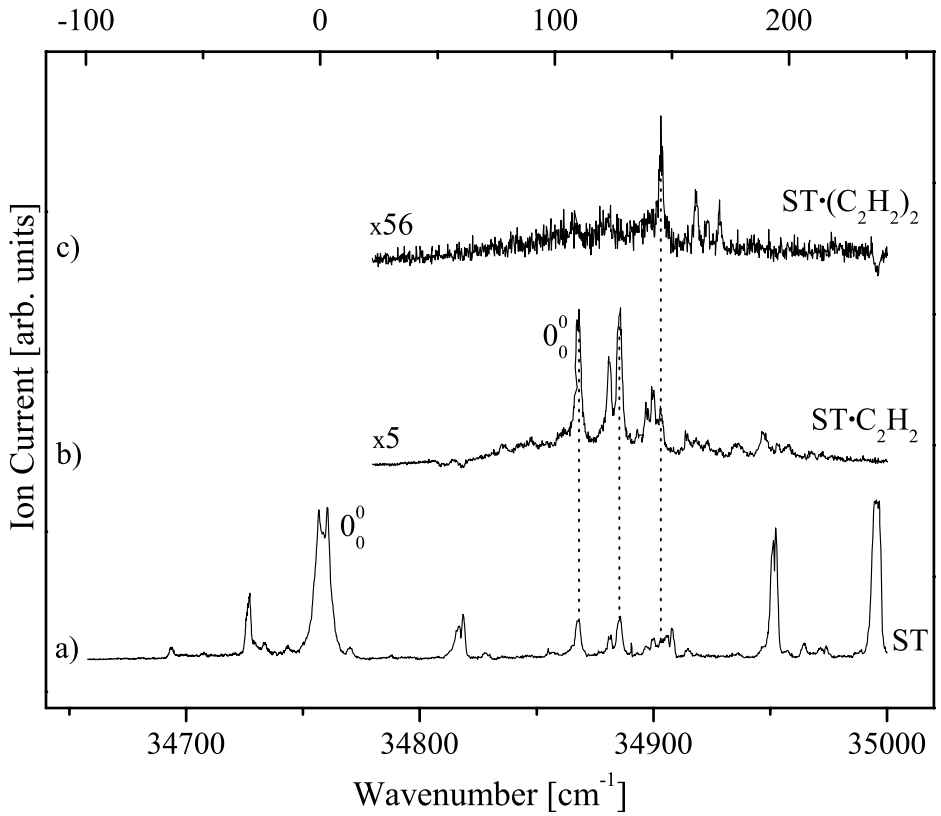

Figure 7.3: *Low-resolution one-colour R2PI spectra of the $S_1 \longleftarrow S_0$ electronic transition of jet-cooled ST and its complexes with C_2H_2 measured at their mass channels: (a) ST monomer (m/z = 104), 0_0^0 origin band is at 34 758 cm^{-1}; (b) ST·C_2H_2 complex (m/z = 130 cm^{-1}), 0_0^0 origin band is at 34868 cm^{-1}; (c) ST·$(C_2H_2)_2$ complex (m/z = 156), 0_0^0 origin band is at 34 903 cm^{-1}. They have been normalized to the intensity of the main band of the ST monomer. Corresponding peaks are designated by vertical dashed lines.*

7.3.2 Vibronic Spectra of the ST·C_2H_2 Cluster

Figure 7.3 shows the low-resolution one-colour R2PI spectra of the $S_1 \longleftarrow S_0$ electronic transition of a) ST monomer (m/z = 104), b) ST·C_2H_2 complex (m/z = 130), c) ST·$(C_2H_2)_2$ complex (m/z = 154). The vertical dashed lines indicate the corresponding peaks in the ST monomer spectrum descending from fragmentation of its complexes with C_2H_2.

The blue-shifted bands in the ST spectrum at 110 cm^{-1}, 122 cm^{-1}, and 126 cm^{-1} result from fragmentation of the ST·C_2H_2 complex and the one at 144 cm^{-1} descends from fragmentation of the ST·$(C_2H_2)_2$ complex. The ST monomer spectrum compares well with the one from Mahmoud et *al*. [214]. The origin band of the ST·C_2H_2 complex is 110 cm^{-1} blue-shifted relative to the origin band of the ST monomer. This means that in the first excited, S_1, electronic state the

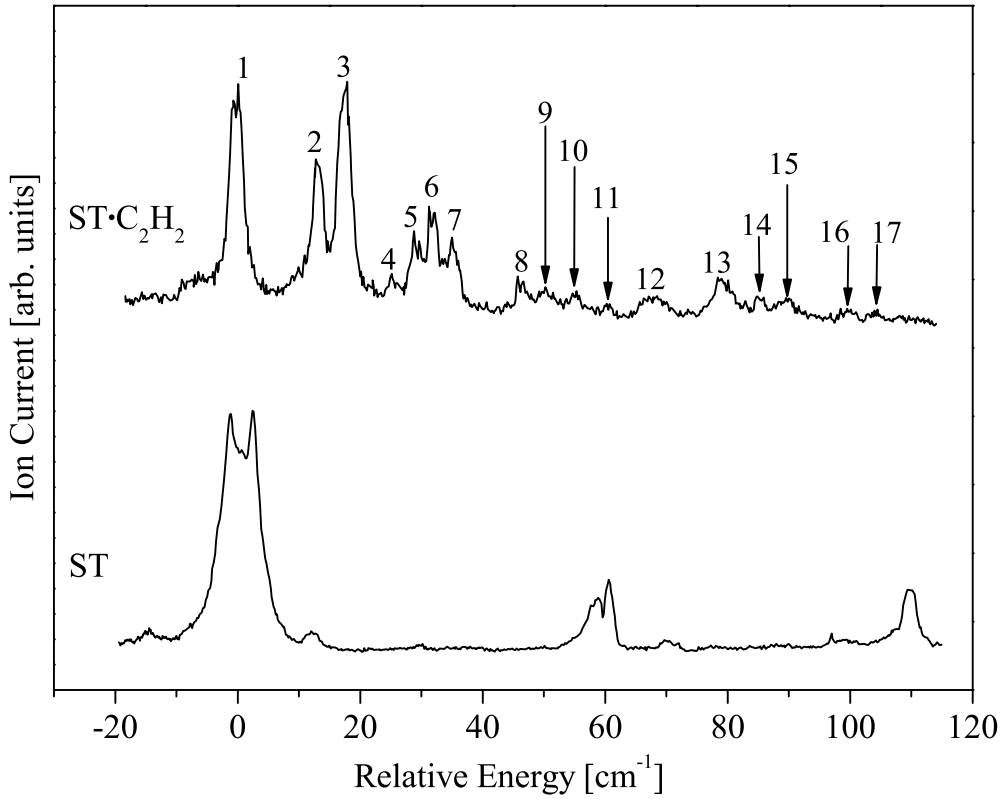

Figure 7.4: *Low-resolution one-colour R2PI spectra of the $S_1 \longleftarrow S_0$ electronic transition of jet-cooled ST·C_2H_2 complex (top) recorded at m/z = 130 mass channel and ST monomer (bottom) recorded at m/z = 104 mass channel as a function of the relative excitation energy above the individual electronic origin. The $S_1 \longleftarrow S_0$, 0_0^0 origin band of the St·C_2H_2 complex is located at 34 867 cm^{-1} and the one of ST is at 34 759 cm^{-1}. The experimental band positions are summarized in Table 7.2.*

complex is destabilized compared to the ground electronic state. This effect is typical also for the hydrated complexes of ST [214] in contrast to the van der Waals clusters, as can be observed in the case of the ST·Ar complex [216, 217].

In Fig. 7.4, the low-resolution R2PI spectra of the ST monomer and the ST·C_2H_2 complex are plotted with a common origin position as a function of the relative excitation energy. In this way the features arising from the intermolecular vibrations in the ST·C_2H_2 complex can be easily identified. It is obvious that all peaks in the low-frequency region up to *ca*. 100 cm^{-1} in the spectrum of the ST·C_2H_2 complex do not have counterparts in the vibronic spectrum of the ST monomer and hence can be attributed to intermolecular vibrational bands of the cluster. The peaks at 11 cm^{-1} and 60 cm^{-1} have been assigned to the vibronic band 29_1^1 and the cross-sequence band $41_0^1 42_1^0$ of ST, respectively [214]. The experimental vibrational frequencies of the ST·C_2H_2 complex are listed in Table 7.2, where the corresponding theoretical frequencies obtained from

the vibrational analysis of the excited, S_1, electronic state of Conformer I are also shown. A

Peak No	Exp.position, cm^{-1}	Calc. position, cm^{-1} Conformer I	Assignment
1	0	0	0_0^0
2	12.7	**11**	A *Bending*
3	17.8	**13**	B *Bending*
4	25.0	22	2A
5	28.7	24	A + B
6	31.1	**34**	C *Stretching*
7	34.9	-	Fragmentation
8	45.6	**45**	D *Swinging*
9	50.1	48/52	B + C or 3B
10	55.2	56	A + D
11	60.2	**58**	E *Swinging*
12	68.4	69	A + E
13	78.3	78	C + D
14	84.8	-	Fragmentation
15	89.9	90	2D
16	99.4	**98**	F
17	104.4	103	D + E

Table 7.2: *Experimental and calculated(CIS/6-311++G (d, p)level of theory) intermolecular vibrational frequencies of the ST·C_2H_2 complex. A uniform scale factor of 0.94 has been applied to all vibrational frequencies of Conformer I. Capital Latin letters from A through E designate the fundamental vibrational modes. F refers to the intramolecular bending mode of the vinyl group in ST. For details of the assignment, see text.*

uniform scale factor of 0.94 has been used for all theoretically predicted vibrational frequencies. There is a good agreement between the experimental and the theoretical band positions of Conformer I. The strongest single peak has been assigned as the origin band of the ST·C_2H_2 complex. The vibrational assignments of the observed vibronic bands are presented in the last column of Table 7.2.

7.3.3 High Resolution Spectrum of the 0_0^0 Origin Band of ST·C_2H_2

ST Monomer

As a first step towards the investigation of the ST·C_2H_2 complex, we measured the high-resolution R2PI spectrum of the ST monomer. The resulting R2PI spectrum of the $S_1 \longleftarrow S_0$ band of the

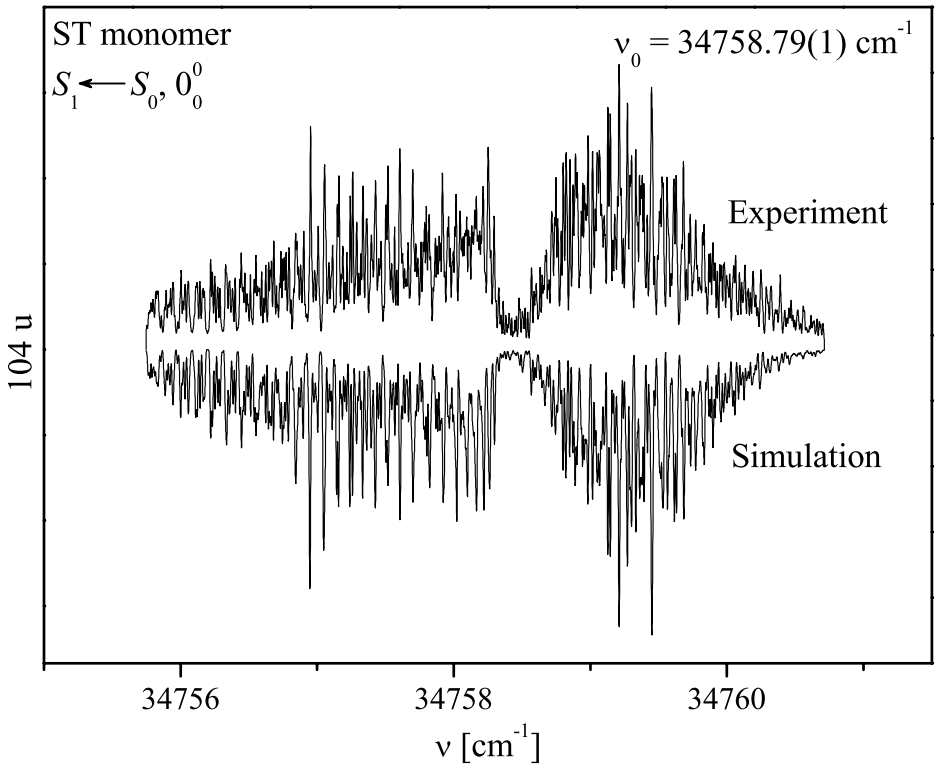

Figure 7.5: *High-resolution two-colour UV R2PI spectrum of the $S_1 \longleftarrow S_0$, 0_0^0 origin band of ST recorded at m/z=104 mass channel with the rotationless transition located at 34 758.79(1) cm^{-1}. Upper trace: experimental spectrum. Lower inverted trace: the best-fit simulated spectrum yielding the constants listed in Table 7.3. For details, see text.*

ST monomer located at 34758.79(1) cm^{-1} measured at its mass (m/z=104) channel is depicted in Fig. 7.5 (upper trace).

Its structure measured at spectral resolution of 110 MHz is very similar to that measured previously using fluorescence detection [218]. The obtained best-fit rotational constants are in a very good agreement with the ones from microwave [219] and fluorescence detection [218] experiments. They produce only a small inertia defect (-0.68 amuÅ and 0.20 amuÅ for the ground, S_0, and the first excited, S_1, electronic state, respectively). This result affirms the planar structure of the ST monomer both in the ground and the first excited electronic state. The relatively large error in the values of the experimental rotational constants corroborate the conclusion of Lombardi and co-workers [220] that the spectrum is not sensitive to changes in the absolute values of the rotational constants. The best-fit spectrum is shown in Fig. 7.5 (lower inverted trace). The achieved cross correlation in this case is as high as 98%. Though not apparent from the appearance of the spectrum, it is almost completely *a* type with a very small *b* contribution. The rotational temperature has been found to be 13 K and this is the reason for the relatively broad

spectrum spanning over more than 5 cm^{-1}. The final results of the GA fit of the high-resolution spectrum are summarized in Table 7.3.

Rotational constant	Ground State S_0		Excited State S_1	
	GHz	cm^{-1}	GHz	cm^{-1}
A	5.175(130)	0.1726(43)	4.993(128)	0.1666(43)
B	1.546(37)	0.0516(13)	1.532(37)	0.0511(12)
C	1.193(33)	0.0398(11)	1.173(34)	0.0391(11)
$\Delta I = I_c^0 - I_a^0 - I_b^0$, amuÅ^2	-0.68		-0.20	
Transition moment ratio $\mu_a^2 : \mu_b^2 : \mu_c^2$	97:3:0			
Origin ν_0 , cm^{-1}	34758.79(1)			
Temperature T , K	13.6(7)			
Best-fit cross correlation (%)	98			

Table 7.3: *Experimental rotational constants, transition moment ratio, origin band position, and rotational temperature of the ST monomer from the GA- based computer-aided fit of the highly resolved spectrum (Fig. 7.5) of the $S_1 \longleftarrow S_0$ 0_0^0 origin band (see Fig. 7.3and Fig. 7.4) of ST (for details, see text). The numbers in parentheses represent one standart deviation in units of the least significant quoted digit. The uncertainty of the relative values of μ_a^2, μ_b^2, and μ_c^2 is 2%.*

ST·C_2H_2 Complex

The highly resolved spectrum of the ST·C_2H_2 complex is shown in Fig. 7.6 (upper trace). Its quality is not so good as the one of the ST monomer because of the low signal intensity. The spectrum is superimposed on a background and covers more than 3.5 cm^{-1}. It differs completely in structure from the spectrum of the ST monomer in Fig. 7.5.

The spectrum can be referred to as a hybrid *a* and *b* type, the latter being the dominating contribution. It has a narrow central dip, a weak Q branch, and well expressed P and R branches with irregularly densely spaced aggregations of rotational peaks with a minimum linewidth of *ca*. 250 MHz (FWHM). As in the case of the ST monomer, we employed the GA fitting routine to analyse this spectrum. The stick spectrum was generated using asymmetric top Watson Hamiltonian [221–223]. The maximum rotational quantum number J considered for the calculations was 40. The simulated spectrum was obtained by convolution of the stick spectrum with a Gaussian-shaped line with a linewidth of 150 MHz (FWHM). The optimum linewidth used to fold the stick spectrum is slightly broader than the spectral resolution of our experiment [110 MHz (FWHM)]. We tentatively attribute this to saturation effects rather than to a short lifetime of the excited, S_1, electronic state. The rotational temperature has been determined to be 9.2 K, which is lower than that of the ST monomer. A plausible explanation is that only the sufficiently cold species of the

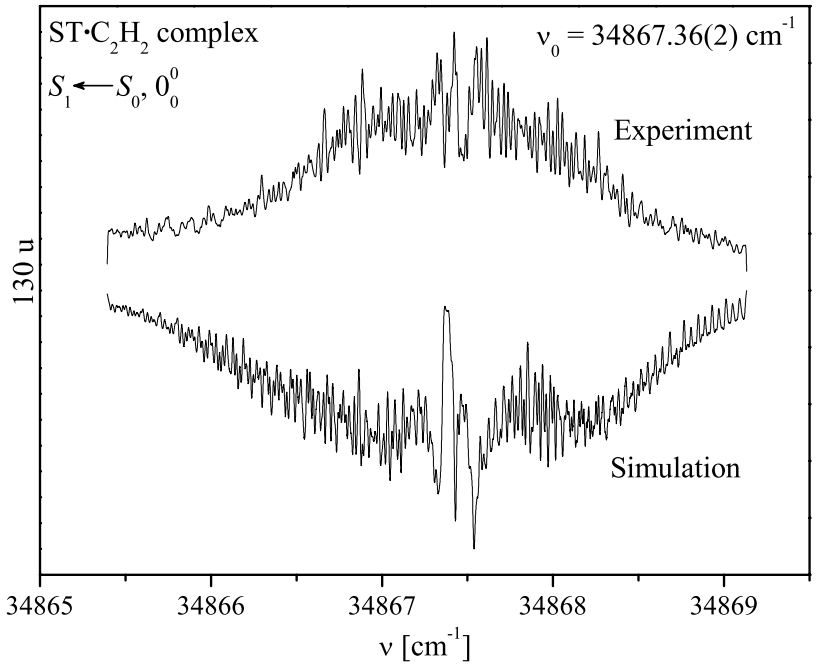

Figure 7.6: *High-resolution two-colour UV R2PI spectrum of the $S_1 \longleftarrow S_0$, 0_0^0 origin band of the ST·C_2H_2 complex recorded at m/z = 130 mass channel with the rotationless transition located at 34 867.36(2) cm^{-1}. Upper trace: experimental spectrum. Lower inverted trace: the best-fit simulated spectrum yielding the constants listed in Table 7.4 (for details, see text).*

complex of ST and C_2H_2 survive under molecular beam conditions and hence can be observed. The experimentally deduced transition moment ratio is 22:78:0, which is a clear manifestation of the hybrid character of the spectrum. The resulting rotational constants for both ground, S_0, and first excited, S_1, electronic state together with the other molecular parameters are presented in Table 7.4.

7.4 Discussion

The planarity of the ST monomer has been a subject of debate and extensive experimental [218–220, 224–228] and theoretical [229–232] investigations for a long time. Our experimental high-resolution results convincingly support the conclusion of Pratt and co-workers [218] that ST is planar in both ground, S_0, and first excited, S_1 electronic state. The inertia defect from our experiment (-0.68 amuÅ as well as those from microwave experiments [219] and highly resolved fluorescence excitation experiments [218] only slightly deviate from zero. This finding is in line with the predicted flat torsional potential about the C(1)-C(α) bond of ST in the ground state [30, 219, 229, 231] and might be an indication that the energy minimum is at a nonszero but

Rotational constant	Ground State S_0		Excited State S_1	
	GHz	cm^{-1}	GHz	cm^{-1}
A	1.3731(330)	0.0458(11)	1.3671(360)	0.0456(12)
B	0.905(23)	0.03018(75)	0.894(20)	0.02982(66)
C	0.6886(69)	0.02297(23)	0.687(18)	0.02292(61)
Transition moment ratio $\mu_a^2 : \mu_b^2 : \mu_c^2$	22:78:0			
Origin ν_0, cm^{-1}	34 867.36(2)			
Temperature *T*, K	9.2(5)			
Best-fit cross correlation (%)	95			

Table 7.4: *Experimental rotational constants, transition moment ratio, origin band position, and rotational temperature of the ST·C_2H_2 complex from the GA- based computer-aided fit of the highly resolved spectrum (Fig. 7.6) of the $S_1 \longleftarrow S_0$ 0_0^0 origin band (see Fig. 7.3and Fig. 7.4) of ST (for details, see text). The numbers in parentheses represent one standart deviation in units of the least significant quoted digit. The uncertainty of the relative values of μ_a^2, μ_b^2, and μ_c^2 is 5%.*

small torsional angle. Theoretically, planarity of ST in the ground electronic state, however, has been found only by DFT B3LYP calculations (cf. Table 7.1). The calculation at the MP2 level with 6-311++G(*d*, *p*) basis set yields nonplanar structure. The theoretical modelling of ST in the first excited electronic state at CIS/6-311++G (*d*, *p*) level of theory predicts completely planar geometry. The rotationally resolved spectrum of the ST monomer is sensitive to alterations of the transition moment ratio [201, 218]. The experimentally found orientation of the TM vector is in line with the predictions of our *ab initio* calculations on the excited electronic state. This demonstrates that the CIS method with 6-311++G (*d*, *p*) basis set can adequately describe the electronic excitation in a system with an unsaturated group covalently bonded to a phenyl ring.

The origin band of the ST·C_2H_2 complex is blue-shifted by 110 cm^{-1} relative to the origin band of the ST monomer. This is a typical behaviour for π-bonded systems [13, 25–27, 29, 30, 233–241], which suggests that most likely C_2H_2 binds to ST via formation of a C-H$\cdots\pi$ hydrogen bond between the terminal C-H group of C_2H_2 and the π electrons of the phenyl ring in ST. On the grounds of the *ab initio* calculated binding energies, the structure where C_2H_2 is the proton donor (Conformer I) is the favoured one. The good agreement between the predicted theoretical frequencies (see Table 7.2) and the observed vibronic bands (see Fig. 7.3 and Table 7.2) is a further argument in addition to the energy considerations that Conformer I produces the measured spectrum. This finding is in accord with the results for similar weakly bound molecular complexes [41, 43, 45, 211, 214, 242]. The blue shift in the case of the ST·C_2H_2 complex is bigger compared to the corresponding blue shifts in the ST·H_2O complex [214]. This demonstrates that upon electronic excitation the ST·C_2H_2 cluster is destabilized more than the ST·H_2O com-

plex. As seen, the ST·C_2H_2 complex (m/z=130) undergoes an efficient fragmentation into the mass channel of ST (m/z=104) similar to the ST·H_2O cluster (m/z=122) [214]. In the case of one-colour experiments the most straightforward explanation for the fragmentation might be the high excess energy of the ionization photon above the dissociation limit in the cluster ion. The observed efficient fragmentation also in the case of the two-colour high-resolution experiments suggests that the fragmentation mechanism of the ST·C_2H_2 complex is the same as in the case of ST·H_2O, i.e., the fragmentation results from a structural change between the neutral and the ionic cluster [214] as the polarizable part of the C_2H_2 π electrons confined between the two carbon atoms would try to reorient the ST species. This leads automatically to high excess energy after an efficient ionization resulting in a subsequent fragmentation. From the analysis of the fragmentation pattern and the frequency assignments, we can infer that C_2H_2 binds to ST as a proton donor forming a C-H$\cdots\pi$ bond with its CH group and the π electrons of the benzene ring. The alternative structure, in which C_2H_2 acts as a proton acceptor and bonds via its delocalized π electrons to one H atom from the benzene ring and one H atom from the vinyl group (Conformer II), has not been observed in our experiment. It is worthwhile to note that a similar binding pattern has been theoretically predicted also for Bzn·C_2H_2 complex [43,45]. This structure has been found to pertain a very flat potential surface and it corresponds to a local potential minimum . Very small negative values for the lowest vibrational frequencies of stationary point structures in vicinity of the minimum have been observed, which correlates well with the *ab intio* predicted negative vibrational frequency for Conformer II of the ST·C_2H_2 complex (see Sec. 7.3.1).

The most stringent and detailed information on the structure of the C-H$\cdots\pi$ bound complex of ST and C_2H_2 can be retrieved from the analysis of its highly resolved UV spectrum with partial rotational resolution. As seen from Table 7.1, the theoretical investigations at the MP2 and B3LYP model theories predict different values for the tilting angle (α_3 $n\cdots$C(16)-C(17)) of the C_2H_2 moiety and the torsion of the vinyl group (τ_1 C(β)C(α)C(1)/C(α)C(1)C(2)) for the more stable Conformer I. It merits discussion whether the torsion of the side chain predicted by the MP2 calculation results from an interaction between the attached C_2H_2 moiety or it is a computational effect similar to the one in the case of the ST monomer where the MP2 theory fails to predict the experimentally confirmed planarity. In the MP2 calculated structure of Conformer I, the torsion of the vinyl group is accompanied also by a significant tilting of C_2H_2 relative to the perpendicular *n* to the benzene ring plane in direction to the side chain. This suggests an interaction between the π electrons of the vinyl group with the ones of C_2H_2. The inertial parameters of this structure, however, deviate noticeably from the ones deduced from the fit of the highly resolved spectrum of ST·C_2H_2. The experimental rotational constants for the electronic ground state, on the other hand, agree best with the ones resulting from the B3LYP calculations. In the latter, the C_2H_2 moiety is only slightly tilted from the perpendicular to the benzene ring plane. Obviously, in this geometry the relevant binding interaction is that between C_2H_2 and

the π electrons of the benzene ring. It is worth to note that the torsion of the side chain in the MP2 optimized geometries both for ST and ST·C_2H_2 is almost the same (cf. Table 7.1), which eliminates a possible influence of C_2H_2 on the torsion of the side chain in ST. This observation, in conjunction with the discrepancy between the experimental and the MP2 theoretical constants for Conformer I, leads to the implication that the vinyl group bending out of the benzene ring plane is a computational artefact. Thus, we can confidently conclude that the structure of the ST·C_2H_2 complex observed under conditions of molecular jet expansion is closest to the one predicted at the B3LYP level of theory.

The transition moment ratio found from the fit of the highly resolved spectrum (μ_a^2:μ_b^2:μ_c^2 = 22:78:0) is substantially different from the one of ST (μ_a^2:μ_b^2:μ_c^2 = 97:3:0) but is in excellent accord with the one theoretically predicted for the ST·C_2H_2 complex, Conformer I. Since C_2H_2 is a nonpolar molecule and the interaction with the π electrons of the ring is weak, it is anticipated that the formation of a complex between ST and C_2H_2 will not alter the orientation of the transition moment vector of ST. To probe this statement, we calculated the projections of the *ab initio* found TM vector of the ST·C_2H_2 onto three mutually perpendicular unit vectors with a common origin at the centre of the benzene ring. The three unit vectors have been defined to be collinear with the short and long benzene ring axes, and the C_6 symmetry axis, respectively. The result is that in Conformer I, the TM vector is polarized almost completely along the long axis of the phenyl ring, i.e., no deviation of the TM vector upon complexation between ST and C_2H_2 occurs within the accuracy of the experiment. Thus, the different TM ratio of the ST·C_2H_2 complex is a pure mass effect coming about because of the rotation of the principal axis system due to the attachment of C_2H_2.

It is instructive also to compare the binding pattern and the interactions in ST·C_2H_2 with those of similar systems. Mahmoud et *al*. [214] have shown that in the case of the ST·H_2O complex H_2O binds out of the plane of the benzene ring along the C(1)-C(α) bond. It interacts both with the π electrons of the phenyl ring and with those of the vinyl group, the latter interaction being slightly stronger. The stronger interaction of H_2O with the vinyl group determines the small blue shift (21.5 cm^{-1}) [214]. Unlike the case of the Bzn·H_2O complex [243], in ST·H_2O, the water moiety is strongly shifted towards the side chain due to the additional interaction with the vinyl group. This clearly demonstrates that ST provides two binding sites for proton donors: the π electrons of the phenyl ring and the π electrons of the vinyl group. The discussed binding pattern of ST·H_2O is similar to the one characterizing the T-shaped structure observed in Bzn·$(C_2H_2)_2$ [41]. Regarding π electrons, the vinyl group is similar to C_2H_2 where the π electron density forms a ring around and perpendicular to the C(16)-C(17) bond [45, 244]. This similarity lends a ground for treating the interactions in the ST·C_2H_2 complex in a fashion similar to the Bzn·$(C_2H_2)_2$complex. It has been found [45, 244] that the most stable structures of the Bzn·$(C_2H_2)_2$ complexes when both

C_2H_2 moieties are on the same side of the benzene ring are the T-shaped ones: the two C_2H_2 molecules form a bond between the C-H group of one of the moieties and the π electrons of the other one. We would expect a similar interaction also between C_2H_2 and the vinyl group, if such existed, i.e., one of the C-H groups of C_2H_2 should point to the π electrons of the vinyl group. The lack of an H atom directed towards the π electrons of the vinyl group precludes the formation of an H$\cdots\pi$ vinyl group bond in the case of ST$\cdot C_2H_2$. This brings the conclusion that in the conjugated system of the benzene ring and the vinyl group in ST, the benzene ring is the stronger proton acceptor from nonpolar molecules such as C_2H_2. In a simpler complex, Bzn$\cdot C_2H_2$, the C_2H_2 moiety lies on the C_6 symmetry axis binding to Bzn through a C-H$\cdots\pi$ bond [45, 242], a pattern established also for the case of ST$\cdot C_2H_2$. The tilting of the C_2H_2 moiety in ST$\cdot C_2H_2$ relative to the perpendicular axis to the benzene ring is brought about by the asymmetry of the π electron density of the benzene ring due to their conjugation with the π electrons of the vinyl group rather than to a direct interaction between C_2H_2 and the vinyl group. The stronger interaction of the C_2H_2 moiety with the benzene ring in ST$\cdot C_2H_2$ compared to ST$\cdot H_2O$ determines also the bigger blue shift.

7.5 Summary and Conclusions

The weakly bound complex of ST with C_2H_2 has been studied by mass selective low- and high-resolution UV R2PI spectroscopy in combination with computer-assisted rotational fit analysis and high-level *ab initio* calculations with extended basis sets. Two stable conformers of the ST$\cdot C_2H_2$ complex have been found by a grid search and subsequent structural optimization in the ground state at the MP2/6-311++G (*d, p*) and B3LYP/6-311++G (*d, p*) level of theory, respectively. In the lowest-energy conformer, C_2H_2 donates a proton to the π electrons of the benzene ring of ST thus forming a nonspecific hydrogen bond of C-H$\cdots\pi$ type. In the second lowest-energy geometry, C_2H_2 binds to ST sideways being a proton acceptor from two benzene-ring H atoms. Only one conformational structure has been identified in the molecular beam from the fit of the highly resolved spectrum of ST$\cdot C_2H_2$ measured at its parent mass (m/z = 130) channel and has been assigned to the ST$\cdot C_2H_2$ conformer in which C_2H_2 is a proton donor. All other bands of reasonable intensity have been assigned as vibrational states of the ST monomer by comparison with the results from the CIS/6-311++G (*d, p*) calculations. In neither of the two conformers, however, does the binding pattern of C_2H_2 to ST make the interaction between C_2H_2 and the vinyl group of ST feasible. The experimental results on the ST$\cdot C_2H_2$ complex are satisfactorily reproduced by the B3LYP-optimized structure where the C_2H_2 moiety is slightly tilted to the benzene ring plane with ST being planar. The latter is in agreement with the planarity of the ST monomer again confirmed by our high-resolution experiment. The observed small tilting of the C_2H_2 moiety descends from the asymmetry of the π electrons of the benzene ring due to

their conjugation with the ones of the vinyl group. No change of the TM orientation of ST has been observed upon the cluster formation with C_2H_2. The different TM ratio in the ST·C_2H_2 complex compared to that in ST is a mass effect arising from the attachment of C_2H_2. The binding pattern of C_2H_2 to ST, the formation of a C-H$\cdots\pi$-type hydrogen bond, and the traits of such type of interaction support the results obtained for similar systems, e.g., Bzn·C_2H_2. This result clearly demonstrates that though the conjugation and the competition between the two π-electron systems, the one of the phenyl ring and the one of the vinyl group, the phenyl ring remains the preferred binding site for C_2H_2.

Chapter 8

van der Waals Bonding to a Molecule with π-electron Conjugation: Complex Between Styrene and Ar

S. Chervenkov, P. Q. Wang, T. Chakraborty, H. J. Neusser, Z. Phys. Chem. **221**, 1 (2007).

Combining high-resolution mass-selective resonance-enhanced two-photon ionization spectroscopy analysed by genetic-algorithm-based computer-assisted rotational fit and high-level ab initio calculations we were able to determine the structure and the transition moment orientation of the styrene-Ar complex. The results demonstrate that Ar binds to the benzene ring of styrene. The binding site of Ar is 3.42 Å *above the benzene-ring plane and is close to the C_6 symmetry axis of the aromatic ring, but slightly shifted to the vinyl group, which implies that the binding pattern is perturbed by the presence of the bonded to the benzene ring vinyl group. The transition moment ratio of the styrene-Ar complex is considerably different from the one of bare styrene, this being a purely mass effect stemming from the reorientation of the principal axes of inertia upon the cluster formation. The red shift of the 0_0^0 origin band of the styrene-Ar_2 complex is almost twice that of the single complex, indicating that the red-shift additivity rule holds in this case. On this basis we conclude that the second Ar atom is bound to the opposite side of the benzene ring.*

8.1 Introduction

Complexes between substituted benzene molecules and noble-gas atoms serve as prototype systems for exploration of microsolvation processes and weak van der Waals interactions with π-electron systems, which play an important role in liquids and supramolecular assemblies. These systems have been a subject of intense scientific interest over the last two decades [14, 17, 27, 210, 245–248]. A considerable insight into the nature of this type of weak interactions has been achieved both by spectroscopic experiments [17–19, 23, 88, 205, 245, 247, 249–259] and advanced theoretical modelling [258, 260–266]. Most of the systems considered to date include clusters between a noble-gas atom and a molecule with a single π-electron system. Thus, in this case, the binding pattern of the noble-gas atom to the host molecule is predominantly determined by the aromatic ring that contains the π electrons, and is weakly perturbed by the presence of the benzene ring substituent. Molecules containing an unsaturated carbon bond in a side chain covalently bound to a single benzene ring constitute an interesting class of species whose intrinsic properties are determined by the conjugation and further delocalization of the two π-electron systems [42]. Such molecules pose an interesting issue on the preferred binding site of the noble gas atom, which can serve as a signature for the degree of electronic conjugation. The simplest among the above-mentioned class of molecular species is styrene, which consists of a benzene ring and a vinyl group covalently bound to it. It is known that ST exhibits a strong mesomeric effect and hence due to the electronic density delocalization the benzene ring is no longer expected to be the only possible nesting site for a van der Waals bonded noble-gas atom. On the other hand, a binding site off the benzene-ring plane can serve as a convenient probe for the planarity of ST, which has been debated for a long time.

In this chapter, the investigations of the complex of ST and Ar and ST and two Ar are presented. The experimental results include one-colour low-resolution R2PI spectra measured at the mass channels of the ST monomer and the ST·Ar complexes as well as the rotationally resolved two-colour spectrum of the of the origin band of ST·Ar along with the fitted spectrum. To support the experimental findings, we performed high-level quantum chemistry *ab initio* calculations on the structure and the energetics of the ST·Ar complex in both ground, S_0, and first excited, S_1, electronic state. The π-electron interaction in ST is a challenge to *ab initio* calculations because of the orbital delocalization. A possible consequence is the torsion of the side chain, which has been discussed for a long time [219, 220, 225, 226, 228, 229, 232]. Microwave and high-resolution UV spectroscopy have been used to investigate the planarity of the ST monomer. Here, we suggest a much simpler method to check the planarity based on the possible slightly different binding sites of an Ar atom (up and down) in case of an out-of-plane tilted side chain. It is based on the nonequal binding energies in case of two different out-of-plane binding sites of Ar, which should lead to a small splitting of the red-shifted electronic origin bands. In this work we

demonstrate the application of this very accurate and sensitive approach to the case of ST.

8.2 Experiment and Data Processing

Both low-resolution spectra of ST, ST·Ar, and ST·Ar_2 complexes as well as the high-resolution spectrum of the ST·Ar complex have been measured by R2PI with mass selectivity in a supersonic molecular beam. The experimental set up has been described in detail in Sec. 6.2. ST was bought from Fluka with a purity of 96% and used without further purification. The low-resolution spectra of the three species, ST, ST·Ar, and ST·Ar_2, were recorded under the same experimental conditions, whereas the highly resolved spectrum of the ST·Ar complex was obtained after an optimization of the backing pressure and the nozzle-to-skimmer distance. The backing pressure was varied in the range between 2 and 3 bar, and a nozzle orifice of 300μm was used. The skimmer-to-nozzle distance was optimized within the limits of 5 and 7 cm. The Ar^+ ion laser was operating at 514 nm yielding output power of 4 W necessary to pump the ring dye laser. The latter was using dye achieving an output power of 300 mW.

The analysis of the highly resolved spectrum of the ST·C_2H_2 spectrum has been performed with the computer-assisted fitting routine based on genetic algorithms, described in detail in Sec. 6.3. A stick spectrum was generated employing the asymmetric top Watson Hamiltonian [221, 222] and a maximum quantum number J equal to 20. The best-fit spectrum of the ST·Ar complex was produced after a fit using 200 iterations with 200 individuals. The achieved cross correlation is 96%.

8.3 *Ab Initio* Calculations

Ab initio quantum chemistry calculations at the MP2/cc-pVTZ level of theory for the structure and at the MP2/6-311++G (*d*, *p*) level of theory for the frequencies in the ground, S_0, electronic state of the ST·Ar complex have been performed using Gaussian 03 programme package [70]. The present study involves weak van der Waals interactions and this warrants electron correlation methods with extended basis sets to be used. The torsional angle about the C(1)-C(α) (see Fig. 8.1) bond was kept fixed (0 deg) during the ground state structural optimization. The optimized structure of the ST·Ar complex in the ground, S_0, electronic state is depicted in Fig. 8.1. The most important structural parameters obtained from the *ab initio* calculations for the ground, S_0, electronic state are summarized in Table 8.1. The three lowest vibrational frequencies along with their assignments are also presented in Table 8.1 for comparison with the frequencies of the three blue-shifted bands observed in the one-colour low-resolution spectrum in Fig. 8.2.

Structural and inertial parameters MP2/cc-pVTZ		Vibrational analysis MP2/6-311++G (*d*, *p*)	
		Frequency, cm^{-1}	Assignment
h, A	3.42	11.7	Long axis *bending*
s_1, A	0.24	26.2	Short axis *bending*
s_2, A	0.02	34.2	*Stretching*
A, GHz/cm^{-1}	1.34753/0.04495		
B, GHz/cm^{-1}	1.02483/0.03418		
C, GHz/cm^{-1}	0.75026/0.02503		

Table 8.1: *Structural and inertial parameters: distance from the Ar atom to the benzene-ring plane, h, projections of the Ar atom onto x and y axes of the benzene-ring-fixed coordinate system, s_1, and s_2, respectively, and rotational constants for the ground, S_0, electronic state of the ST·Ar complex calculated at the MP2/cc-pVTZ level of theory. Vibrational analysis: the three lowest intermolecular vibrational frequencies of the ST·Ar complex and their assignments calculated at the MP2/6-311++G(d, p) level of theory.*

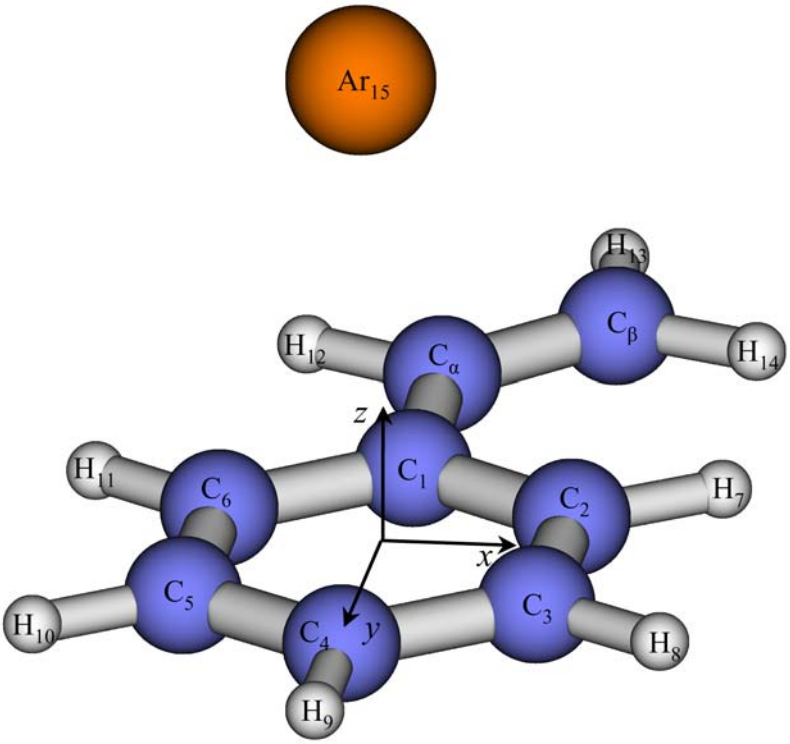

Figure 8.1: *Electronic ground state, S_0, structure of the ST·Ar complex optimized at the MP2/cc-pVTZ level of theory. The xyz coordinate system is the benzene-ring-fixed coordinate system with its origin pinned at the centre of the benzene ring. The z axis is parallel to the C_6 symmetry axis of benzene. For details, see Table 8.1.*

8.4 Experimental Results

8.4.1 Low Resolution Spectra

Figure 8.2 shows the mass discriminated low-resolution one-colour R2PI spectra of the $S_1 \longleftarrow S_0$ electronic transition of a) ST monomer when measured at the mass of m/z = 104, b) ST·Ar complex (m/z = 144), and c) ST·Ar_2 complex (m/z = 184). The vertical dashed lines indicate the corresponding red-shifted bands in the ST monomer spectrum originating from fragmentation of its complexes with Ar. The 0_0^0 origin band of the ST·Ar complex is red-shifted by 31 cm^{-1} relative to that of bare ST, and the origin band of the ST·Ar_2 complex is red-shifted by 64 cm^{-1}. It is seen that a detachment of a single Ar atom brings about the small red-shifted band observed at the mass channel of the ST·Ar complex. The observed red shift of the ST·Ar complex is in a good agreement with the one observed by Jortner and co-workers [216]. The low-resolution spectra of both ST·Ar and ST·Ar_2 exhibit bands to the high energy side of the respective origins corresponding to low-frequency intermolecular vibrations of the complexes. The blue-shifted bands of the ST monomer have been discussed in a recent publication by our group [42].

8.4.2 High Resolution Spectrum

For determination of the structure of the ST·Ar complex, the high-resolution spectrum of the 0_0^0origin band has been recorded and analysed. The experimental spectrum with partial rotational resolution of the ST·Ar complex is presented in Fig. 8.3 (upper trace). The spectrum sits on a background and spans over 3 cm^{-1}. Its overall profile is significantly different from that of the ST monomer spectrum [42]. The spectrum can be referred to as a hybrid type. It has a prominent Q branch, a weak central dip, and well pronounced P and R branches composed of irregularly spaced clumps of rotational lines with a minimum linewidth of 250 MHz (FWHM). To analyse the spectrum, we employed the GA fitting routine described in Sec. 8.2. The simulated spectrum was obtained after convolution of the stick spectrum with a Gaussian-shaped line with a linewidth of 220 MHz (FWHM), which is larger than the spectral resolution of our experiment (110 MHz (FWHM)). We attribute this to saturation effects. The rotational temperature has been determined to be 6 K, which is lower than that for the ST monomer [42]. We propose two reasonable explanations: either the observed ST·Ar complex descends from fragmentation of larger clusters (ST·Ar_n, n≥2) and the obtained temperature is a result of evaporative cooling or this is an indication that only sufficiently cold cluster species can survive under molecular jet conditions. The transition moment ratio, $\mu_a^2 : \mu_b^2 : \mu_c^2$, is 47:52:1. The inertial parameters for the ground and the first excited electronic state along with the molecular characteristics are listed in Table 8.2.

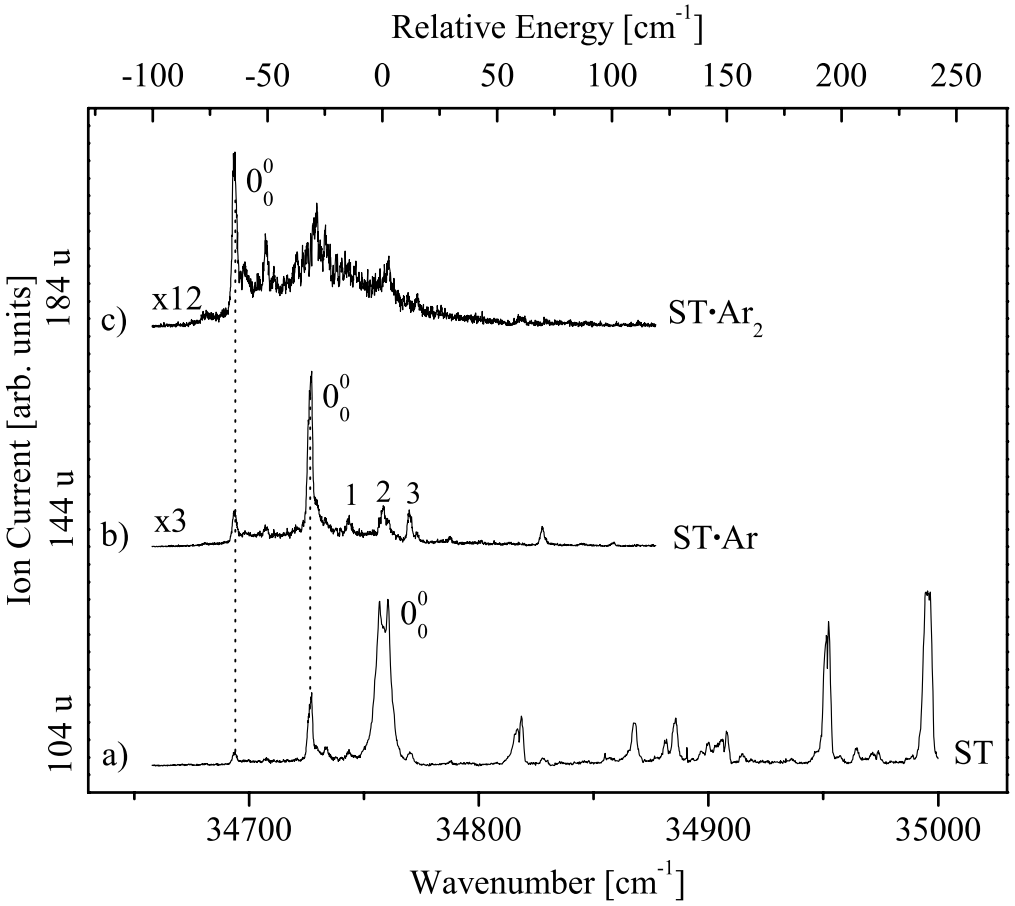

Figure 8.2: *Low-resolution one-colour R2PI spectra of the $S_1 \longleftarrow S_0$ electronic transition of jet-cooled ST and its complexes with Ar measured at their mass channels: a) ST monomer (m/z = 104), 0_0^0 origin band is at 34 758 cm^{-1}; b) ST·Ar complex (m/z = 144), 0_0^0 origin band is at 34727 cm^{-1}. The blue-shifted intermolecular vibronic bands are designated by 1, 2, and 3, respectively; c) ST·Ar_2 complex (m/z = 184), 0_0^0 origin band is at 34 693 cm^{-1}. The vertical dashed lines indicate the fragmentation of the clusters leading to a signal at the ST·Ar and the ST monomer mass channel.*

8.5 Discussion

The planarity of the ST monomer has been a subject of intense debate over the past three decades. Microwave experiments have shown that ST is planar in the ground electronic state [219]. This has been confirmed also by rotationally resolved LIF experiments [218] and high-resolution R2PI experiments in our laboratory [42]. The latter have ascertained planarity of ST also in the first excited electronic state. It is reasonable to assume that due to the weak van der Waals interaction, the attachment of an Ar atom to a molecule does not alter the structure of the latter neither does its transition moment orientation [205]. For this reason, the complexation with Ar can serve as a

Parameter	Ground state S_0		Excited state S_1	
	GHz	cm^{-1}	GHz	cm^{-1}
A	1.337(14)	0.04461(46)	1.3179(81)	0.04396(27)
B	1.0343(78)	0.03450(26)	1.1152(87)	0.03720(29)
C	0.7600(66)	0.02535(22)	0.7198(63)	0.02401(21)
TM ratio				
$\mu_a^2 : \mu_b^2 : \mu_c^2$		47:52		
Origin, ν_0, cm^{-1}		34726.597(3)		
Temperature T, K		7.5(3)		
Best-fit				
cross correlation (%)		96		

Table 8.2: *Experimental rotational constants, transition moment ratio and band origin frequency of the ST·Ar complex resulting from the fit of the rotational structure of the $S_1 \longleftarrow S_0$ electronic transition (see Fig. 8.3). The numbers in parentheses represent one standard deviation in units of the least significant quoted digit. The uncertainty for the relative values of μ_a^2, μ_b^2, and μ_c^2 in the transition moment ratio is 2%.*

very sensitive probe for planarity of aromatic molecules. If such a molecule is nonplanar, the two binding sites of Ar on both sides of the benzene ring are not completely equivalent thus leading to slight differences of the binding energies for the two conformers, as we have recently demonstrated for the case of the complex between 2-phenylethanol and Ar [205]. This shows up as two different $S_1 \longleftarrow S_0$ origin band transitions of the complex separated by 2 cm^{-1} corresponding to the two binding patterns. For the shorter side chain of ST, even a smaller splitting should be expected, particularly for a small torsional angle about the C(1)-C(α). On the contrary, if the host molecule is completely planar, the two binding sites of Ar on both sides of the benzene ring are completely undistinguishable leading to the appearance of a single origin band. In the case of ST·Ar neither splitting of the 0_0^0 origin band nor appearance of a second peak in the vicinity of the first one in the low-resolution spectrum measured at the cluster mass channel have been observed. However, a small splitting can be recognized only under high resolution conditions as has already been shown for the case of the complex between 2-phenylethanol and Ar [42]. Figure 8.3 clearly shows that the measured rotational structure is explained by a single vibronic band and no splitting is observed within the effective linewidth of 250 MHz. This is a clear evidence for the planarity of the ST monomer. The three blue-shifted vibronic bands 1, 2, and 3, in the low-resolution spectrum of the ST·Ar cluster (see Fig. 8.2) are satisfactorily reproduced by the frequency analysis of the theoretically optimized structure of the complex (see Sec. 8.3 and Table 8.1), and they are assigned as long-axis (along y axis) bending , short-axis (along x axis) bending, and stretching (parellel to z axis) vibrations, respectively. This result is a further confirmation for the structural assignment of the observed ST·Ar complex. The small differ-

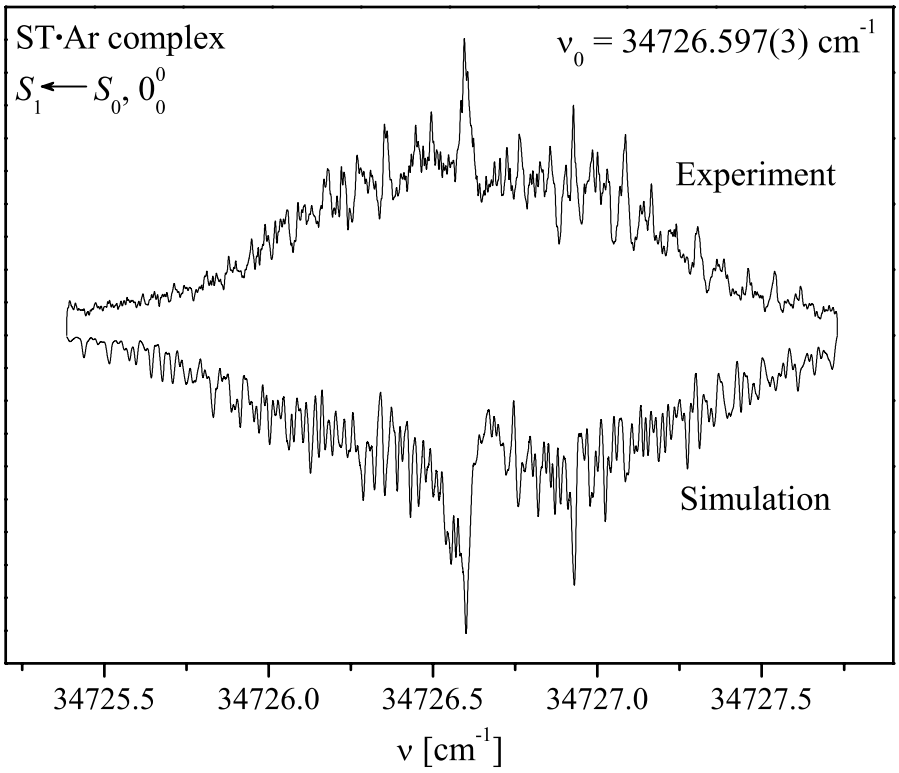

Figure 8.3: *High-resolution two-colour UV R2PI spectrum of the $S_1 \longleftarrow S_0$, 0_0^0 origin band of the ST·Ar complex recorded at m/z=144 mass channel with the rotationless transition located at 34726.597(3) cm^{-1}. Upper trace: experimental spectrum. Lower inverted trace: the best-fit simulated spectrum yielding the constants listed in Table 8.2 (for details, see text).*

ence between the experimental and theoretical vibrational frequencies is not surprising bearing in mind the pronounced of this type of intermolecular vibronic modes, which ususally mars the accuracy of the theoretical predictions.

The origin band of the ST·Ar_2 complex is red-shifted twice (64 cm^{-1}) as much as the red shift of the ST·Ar complex (31 cm^{-1}). This is a clear manifestation of the additivity rule, which holds when no three-body interaction is present, i.e., the second Ar atom binds to the opposite side of the benzene ring of ST without being affected by the presence of the other Ar atom through a deformation of the π electrons of the benzene ring. It is obvious that upon ionization the ST·Ar_2 complex undergoes an efficient fragmentation which brings forth the red-shifted peak at the ST·Ar mass channel.

Since ST possesses two π-electron systems, it provides two possible out-of-plane binding sites for Ar. The observed red shift of the origin band of the ST·Ar complex, however, is typical for Ar complexes in which the Ar atom is bound to the benzene ring, e.g., toluene [267]. More

detailed information on the structure of the complex can be obtained from the analysis of the highly resolved spectrum in conjunction with quantum chemistry *ab initio* calculations. The rotational constants found from the fit of the high-resolution spectrum are in accord with the ones predicted by the MP2/cc-pVTZ theory for the structure where Ar is situated above the benzene ring. The analysis of this structure reveals that the Ar atom does no longer lie on the C_6 symmetry axis of the benzene ring but is shifted by 0.24 Å towards the vinyl group. There is no appreciable displacement along the short axis of benzene. We attribute the shift along the long axis of the benzene ring to the reduced symmetry of the benzene ring π-electron system due to the conjugation with the π electrons of the vinyl group rather than to a direct interaction between the Ar atom and the vinyl group. The TM ratio of the complex ($\mu_a^2 : \mu_b^2 : \mu_c^2 = 47 : 52 : 1$) is different from the one of the ST monomer ($\mu_a^2 : \mu_b^2 : \mu_c^2 = 97 : 3 : 0$) [42]. We have proved that this is a pure mass effect resulting from the attachment of Ar and leading to an axis switching, and the binding of Ar does not influence the orientation of the TM relative to the frame of the benzene ring.

8.6 Summary and Conclusions

The van der Waals complex between ST and Ar has been studied by high-resolution mass selective R2PI spectroscopy combined with rotational fitting spectral analysis based on genetic algorithms and high-level *ab initio* quantum chemistry calculations. The results show that the Ar atom is located above the benzene ring of styrene in vicinity to the C_6 symmetry axis of the aromatic ring. The complex is bound by a weak van der Waals interaction between the Ar atom and the π electrons of the benzene ring. The complexation pattern is slightly affected by the presence of the bonded to the benzene ring vinyl group and the π electronic delocalization of the styrene moiety. The manifestation of this influence is the shorter distance from the Ar atom to the benzene ring compared to the benzene·Ar complex and the small shift of Ar in direction to the vinyl group. It has been shown that the orientation of the transition moment of styrene remains unaffected by the complexation with Ar. The comparison between the observed blue-shifted vibronic bands in the low-resolution spectrum of the ST·Ar complex with the results of the theoretically calculated vibronic frequencies of the cluster ascertains that those bands correspond to intermolecular bending and stretching vibrations . No splitting of the main band of the ST·Ar complex has been observed neither in the low- nor in the high-resolution spectrum, which demonstrates that styrene is planar. In addition to the ST·Ar complex, the structure of the ST·Ar_2 complex has been briefly discussed on the basis of the experimentally observed red shift of its 0_0^0 electronic transition. The latter is almost twice as much as the one of the single cluster, which implies that the additivity rule applies in this case. This is an indication that the second Ar atom binds to the other side of the benzene ring with a neglible through-ring interaction with the first

Ar atom.

In conclusion, we have demonstrated that the combination of high-resolution mass selective resonance-enhanced two-photon ionization spectroscopy, rotational analysis based on genetic algorithms, and *ab initio* quantum chemistry calculations is a powerful approach towards the investigation of weakly bound complexes. It is capable of providing reliable information on the structure of such complexes and thus allows for the understanding of the subtle interplay between the effects involved in the stabilization of the complex. In addition, the attachment of a noble-gas atom to a molecule provides an efficient and sensitive method for probing its planarity/nonplanarity by detecting under high resolution a possible small splitting of the origin band electronic transition observed in case of nonequivalent binding sites for nonplanar molecules.

Chapter 9

Evidence for a σ-type Hydrogen-Bonded Dimer: High Resolution UV Spectroscopy of *p*-Fluorostyrene-Water

S. Chervenkov, P. Q. Wang, J. E. Braun, S. Georgiev, H. J. Neusser, C. K. Nandy, and T. Chakraborty, J. Chem. Phys. **122**, 244312 (2005).

Ab initio calculations predict four stable conformational structures of the singly hydrated cluster of p-fluorostyrene: two out-of-plane with π- and two in-plane with σ-type intermolecular hydrogen bonding between p-fluorostyrene and water. Mass selective resonance enhanced two-photon ionization high-resolution (100 MHz FWHM laser bandwidth) spectroscopy has been employed to partially resolve the rotational structure of the 0_0^0 origin band of the $S_1 \longleftarrow S_0$ electronic transition. A computer-aided fit based on genetic algorithms has been used to analyse the experimental high-resolution spectrum and to determine the observed conformational structure. The good agreement between the experimental and the simulated spectra of the 0_0^0 band and the assignment of the other prominent bands as inter- and intramolecular vibrational progressions clearly demonstrates that the anti in-plane conformer is the most abundant one in the molecular beam. The existence of the σ-type hydrogen bond between p-fluorostyrene and water manifests that the electron attracting effect of fluorine dominates over the releasing mesomeric effect of the vinyl group and thus a π-type hydrogen bonding with the aromatic ring is not favoured in this case.

9.1 Introduction

Gas-phase clusters consisting of aromatic molecules and protic solvents have attracted a lot of attention aiming at the understanding of the microscopic details of hydrophobic interactions, which play a vital role in determination of the structure and function of proteins, micelles and biological membranes. In this context, aromatic molecule-water clusters are the most studied prototypical systems, and considerable amount of spectroscopic and computational data concerning the structure and dynamics of such clusters have been accumulated over the years [3, 13, 240, 268]. For a comparative estimate of interactions between different groups and their effects on structures, it is essential to investigate aromatic systems with various substitutions at different sites of the aromatic ring. The investigations of fluorine-substituted compounds are of particular interest because, in spite of being the highest electronegative element, the crystal structure data indicate that covalently bonded fluorine atoms in organic molecules are very poor hydrogen bond acceptors [269]. Therefore, it is essential to investigate the hydrogen bonding with fluorinated compounds at molecular level. This chapter reports on our gas-phase spectroscopic studies of water binding to *p*-fluorostyrene (*p*-FST) in a cold supersonic jet expansion. This cluster is a suitable prototype for the investigation of molecular systems manifesting competing types of interaction. Two mutually counteracting effects are expected: the mesomeric effect of the vinyl group and the electron attraction by the electronegative fluorine atom.
The vibronically resolved $S_1 \longleftarrow S_0$ electronic spectrum of the 1:1 dimeric complex of *p*-FST and water was measured by one-colour R2PI method in a linear time-of-flight mass spectrometer. For theoretical predictions of possible structures of the complex in the electronic ground state, *ab initio* quantum chemistry calculations taking into account electron correlation have been performed. Theoretical calculations for the electronically excited state using the CIS method have been also performed. To identify the structure of the experimentally observed *p*-FST·H_2O cluster, a high-resolution two-colour R2PI experiment with mass selection has been carried out. It will be demonstrated that a comparative analysis of the partially rotationally resolved spectroscopic results with the theoretical predictions greatly enhances the unambiguous determination of the realized experimental structure and elucidates the influence of the fluorination on the hydrogen-bonding properties of this class of molecules.

9.2 Experiment and Data Processing

Both low- and high-resolution experimental spectra of the *p*-FS·H_2O complex were measured through R2PI spectroscopy with mass selection in a supersonic jet-cooled molecular beam. The experimental set up is described in detail in Sec. 6.2. The cold molecular beam was produced by adiabatic expansion of the mixture of *p*-FST and water vapours at room temperature seeded in

Ar buffer gas at a backing pressure of 3 bar through a pulsed nozzle with an orifice diameter of 300 μm. The molecular beam was passed through a skimmer with an orifice diameter of 1.5 mm before reaching the interaction point with the laser beams 5cm downstream from the skimmer.

The highly resolved two-colour R2PI spectrum of the *p*-FST·H_2O complex was analized by employing the computer-aided rotational fitting technique based on genetic algorithms descripbed in Sec. 6.3. The values of the parameters used in this particular case are as follows: the number of generations was 1000, and the number of individuals was 1500. The achieved cross correlation was as high as 96%.

9.3 Results and Discussion

9.3.1 *Ab Initio* Calculations

For a detailed discussion of the high-resolution spectra of the experimentally observed 1:1 *p*-FST·H_2O cluster, *ab initio* quantum chemical calculations were started from various chemically reasonable binding sites of water to the *p*-FST molecule. The geometries were calculated at the RHF, B3LYP DFT and at the level using Gaussian 03 suite of programmes [70]. A full optimization of the geometries was carried out using 6-311G (*d*, *p*) basis set. Figure 9.1 shows the optimized structures of the four lowest-energy conformers. The basis set superposition errors (BSSE) in the binding energy in each case was corrected by the counterpoise method of Boys and Bernardy [215]. The energy minima corresponding to these structures are verified noting that all vibrational frequencies calculated by the DFT method using B3LYP/6-311+G (2*d*, 2*p*) basis set are positive. Calculated energies at different levels and some key geometrical parameters of the isomeric species are presented in Table 9.1.

It is seen that compared to the π-hydrogen species, the in-plane σ- hydrogen bonded complexes are more stable at all levels of theory.
It is well-known that the explicit inclusion of electron correlation is essential to get more reliable geometries of benzene-containing complexes. That is why we, performed our calculation at the MP2 level, too. But as far as the binding energy is concerned for the 1:1 *p*-FST·H_2O conformers, the B3LYP level of calculation is more reliable than the others. From Table 9.1 one can see that for conformer III and conformer IV (here, the OH group of the water molecule is involved in the formation of a six-membered ring with the F-C-C-H of the aromatic ring of the *p*-FST molecule) the binding energy is almost the same but for the two out-of-plane conformers the binding energy is smaller by 0.54 kcal/mol for conformer II and 0.74 kcal/mol for conformer I. Recently, Brutschy and coworkers [270] have shown that the in-plane structures for the 1:1 fluorobenzene·water and *p*-difluorobenzene·water clusters are more stable than the out-of-plane

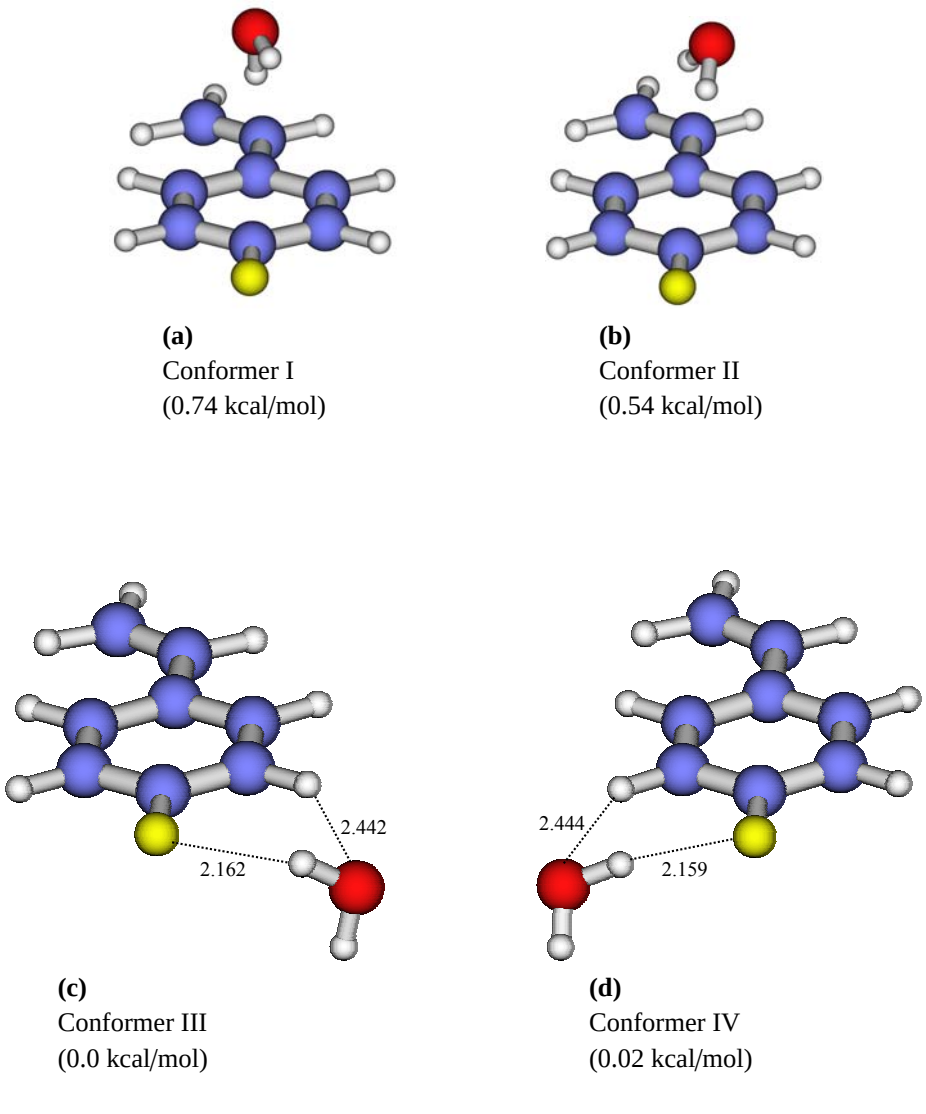

(a)
Conformer I
(0.74 kcal/mol)

(b)
Conformer II
(0.54 kcal/mol)

(c)
Conformer III
(0.0 kcal/mol)

(d)
Conformer IV
(0.02 kcal/mol)

Figure 9.1: *Geometries of the four lowest-energy conformers of the 1:1 p-FST·H_2O complex, optimized at the B3LYP/6-311G (d, p) level of theory. The relative energies (kcal/mol) calculated at the same level are given in parentheses.*

	MP2/6-311G (*d*, *p*)				HF/6-311G (*d*, *p*)				B3LYP/6-311G (*d*, *p*)				CIS/6-311G (*d*, *p*)			
	I	II	III	IV	I	II	III	IV	I	II	III	IV	I	II	III	IV
$-\Delta E_e^N$	4.44	6.01	6.17	6.18	3.16	3.64	4.32	4.33	3.61	3.92	5.13	5.14	4.23	5.82	6.03	6.04
$-\Delta E_e^B$	1.21	1.70	1.71	1.71	1.27	1.44	1.87	1.89	1.31	1.51	2.03	2.05	1.20	1.63	1.66	1.64
$R_{H\cdots\Phi_F}$	$\cdots$	$\cdots$	2.186	2.186	$\cdots$	$\cdots$	2.196	2.191	$\cdots$	$\cdots$	2.161	2.159	$\cdots$	$\cdots$	2.221	2.222
$R_{O\cdots\Phi_H}$	$\cdots$	$\cdots$	2.456	2.456	$\cdots$	$\cdots$	2.529	2.532	$\cdots$	$\cdots$	2.442	2.434	$\cdots$	$\cdots$	2.509	2.511
$R_{H\cdots\Phi}$	3.202	3.14	0.320	0.310	3.291	3.251	0.321	0.316	3.111	3.050	3.181	3.161	3.311	3.221	0.291	0.292
$R_{H\cdots\Phi}$	2.423	2.541	$\cdots$	$\cdots$	2.483	2.512	$\cdots$	$\cdots$	2.428	2.465	$\cdots$	$\cdots$	2.589	2.610	$\cdots$	$\cdots$
$R_{H_{NB}\cdots\Phi}$	3.324	2.902	1.262	1.243	3.311	2.983	1.262	1.257	3.168	2.886	1.264	1.261	3.334	3.043	1.271	1.254
R_{OH}	0.962	0.962	0.961	0.961	0.942	0.942	0.942	0.942	0.963	0.963	0.964	0.964	0.951	0.953	0.952	0.953
$R_{OH_{NB}}$	0.961	0.961	0.959	0.959	0.941	0.941	0.941	0.941	0.962	0.962	0.963	0.963	0.952	0.951	0.954	0.953
Θ_{HOH}	101.4	101.5	101.7	101.8	104.8	104.8	105.2	105.2	103.1	103.2	103.3	103.3	102.5	102.3	102.9	102.8
A	1718	1977	3210	2529	1686	1949	3301	2574	1676	1891	3223	2553	1701	1961	3179	2532
B	804	809	598	648	810	715	584	633	810	794	600	648	794	802	585	626
C	700	742	506	517	692	657	498	509	699	717	507	518	683	731	495	502

Table 9.1: *Binding energies and selected geometrical parameters of the four energetically most favourable conformers of the p-FST·H_2O complex calculated by ab initio quantum chemistry methods. All energies are given in kcal/mol, distances in Angstrom (Å), angles in degrees. $-\Delta E_e^N$ and $-\Delta E_e^B$ represent the binding energies without and with basis set superpoition error (BSSE) correction, respectively. $R_{H\cdots\Phi_F}$ is fluorine to the water hydrogen (hydrogen-bonded) atom distance for conformers III and IV. $R_{O\cdots\Phi_H}$ is the water oxygen to the nearest p-FST hydrogen atom distance for conformers III and IV. $R_{O\cdots\Phi}$, $R_{H\cdots\Phi}$, $R_{H_{NB}\cdots\Phi}$ are the water oxygen , hydrogen (hdrogen-bonded), nonhydrogen-bonded hydrogen atom to the aromatic ring plane distance, respectively. R_{OH}, $R_{OH_{NB}}$, Θ_{HOH} are the water distances and bond angles, respectively. A, B, C are the rotational constants in MHz.*

π hydrogen-bonded structures. In the case of the *p*-FST·H_2O complex, the same result is found for the in-plane conformers for all levels of calculation. The strength of stabilization of the in-plane conformers is due to the electrostatic interactions of the fluorine atom with the water hydrogen atom. Though the vinyl group acts as an electron donor to the aromatic ring, the fluorine atom pulls over the electron density from the benzene ring. As a result, the π-electron cloud density is decreased in the fluorinated styrene and hence the binding energy is smaller for the π-bonded out-of-plane conformers.

In conformer I, one of the O-H bonds of water is π-hydrogen bonded. The distance of the H atom of water from the aromatic plane is 2.423 Å, 2.480 Å, 2.428 Å at the MP2, HF, and B3LYP levels, respectively, which is comparable to the previous experimental values from the high-resolution spectroscopy of the centre-of-mass separations between benzene and water: 3.32±0.07 Å [271], 3.329 [272], and 3.347±0.005 [273], given the O-H bond length in water is 0.96 Å [273]. The centre of mass of the water molecule is shifted towards the vinyl group. In conformer II, both H atoms of the water molecule are directed towards the π electrons of the aromatic ring and the centre of mass is shifted towards the vinyl group. The distance of the oxygen atom from the aromatic ring in this conformation is 3.14 Å. In conformers III and IV, the complex is nearly planar, the oxygen atom is only 0.3 Å off the plane of the aromatic ring and one of the water H-O bonds points to the electronegative fluorine atom. The F$\cdots$H distance in both conformers is the same, 2.186, 2.190, 2.161 Å at the MP2, HF, and B3LYP levels, respectively, and these values are similar to what has been calculated by Tarakeshwar et*al*. in the case of the fluorobenzene$\cdots$water (FBzn·H_2O) complex [270]. The rotational constants are also listed in Table 9.1.

For the excited state calculation, the CIS method with the same basis set, 6-311G (*d*, *p*), was used. For the geometry optimization in the excited state, the ground state geometries were taken as inputs for each of the conformers. The binding energies predicted by such calculations for the four isomeric geometries of the cluster are presented in Table 9.1. The calculation shows that the excited-state binding energies for all the discussed conformers are smaller than the ones of the ground state thus demonstrating that the complex destabilizes in the excited state compared to the ground state. In summary, from the theoretical calculations, one expects that a planar structure will be the most stable one. However, because of the small differences in the binding energies of the predicted conformers, in particular of conformers III and IV, a reliable identification of the realized structure in the beam cannot be made. For this reason, a high-resolution experiment of the 0_0^0 origin band of the $S_1 \longleftarrow S_0$ electronic transition of the cluster was carried out.

9.3.2 Vibronic Spectra of the *p*-FST·H_2O Cluster

Figure 9.2 (upper trace) shows the one-colour R2PI spectrum of the $S_1 \longleftarrow S_0$ electronic transition of *p*-FST·H_2O up to an excess energy of 900 cm^{-1} recorded by selecting the ion signal at the

parent (m/z = 140) mass channel. The R2PI spectrum of the *p*-FST monomer (m/z = 122) [274] (see Fig. 9.2 (lower trace)) was measured to identify the additional features arising due to the intermolecular vibrations of the cluster. Both spectra are shown with a common origin position as a function of the relative excitation energy. The spectrum for the mass channel of m/z = 158, which corresponds to the *p*-FST·$(H_2O)_2$ cluster, was also recorded simultaneously (not shown here) to check whether part of the signal at m/z = 140 resulted from fragmentation of larger clusters. In this way, it was verified that all the sharp features in the top spectrum (Fig. 9.2 (upper trace)) are exclusively due to *p*-FST·H_2O. The 0_0^0 band of the *p*-FST·H_2O complex (34416 cm^{-1}) is blue-shifted by 104 cm^{-1} from that of the *p*-FST monomer (34312 cm^{-1}). The low-frequency bands at 51, 84 and 102 cm^{-1} are due to intermolecular vibrations. The 102 cm^{-1} band can be assigned as the overtone of the mode bringing forth the 51 cm^{-1} band, and the feature at 84 cm^{-1} must correspond to a different mode. Our DFT/B3LYP/6-311+G (2*d*,2*p*) calculations predict for conformer III that in the ground state, the lowest two intermolecular vibrational frequencies of the complex are 42 and 74 cm^{-1}, and they correspond to the out-of-plane and in-plane twisting of the two molecular moieties. Thus, the 51 and 84 cm^{-1} bands can be assigned to these two intermolecular modes . The vibronic bands corresponding to the intramolecular modes of the solute *p*-FST in the complex are indicated by dotted vertical lines. It is seen that the frequencies of these vibrations are rather insensitive to water binding.

Another notable feature of the spectrum is that the electronic origin (0_0^0) and other vibronic bands (e. g. 84 and 89) of the cluster appear as doublet. The separation between the two subbands at the origin is *ca*. 5 cm^{-1}. An immediate explanation of the splitting is that it can be due to an internal rotation of the weakly bound water molecule, similar to what has been observed before in the case of benzene-water clusters [269, 275]. To test this the one-colour R2PI spectrum of the *p*-FST·D_2O complex was measured at its parent mass (m/z = 142) channel. Part of this spectrum, containing the 0_0^0 origin band profile of the $S_1 \longleftarrow S_0$ electronic transition of *p*-FST·D_2O at 34421.0 cm^{-1}, is shown in the inset of Fig. 9.2. It shows that the splitting in the deuterated complex is 5 cm^{-1}, and is the same as that of the hydrated cluster. Therefore, the possibility that an internal rotation or tunnelling are the reason for the observed splitting is ruled out. Other reasons could be sequence transitions or transitions corresponding to a different conformer of the complex. We have measured the spectrum under various cooling conditions of the nozzle expansion and noticed that the relative intensities of the subbands remain practically unaltered. Therefore, it is possible that the two subbands correspond to the electronic origin of two different conformational isomers of the dimeric species. Such an assignment would be consistent with our *ab initio* calculations predicting two planar conformers with almost the same binding energy (see next Section).

The resonant two-photon ionization spectra of unsubstituted styrene-water complexes (ST·$(H_2O)_n$) have been measured recently by Mahmoud et *al*. [214]. The $S_1 \longleftarrow S_0$ origin of the complex exhibits a blue shift by only 21 cm^{-1} with respect to the isolated monomer. This shift is five times

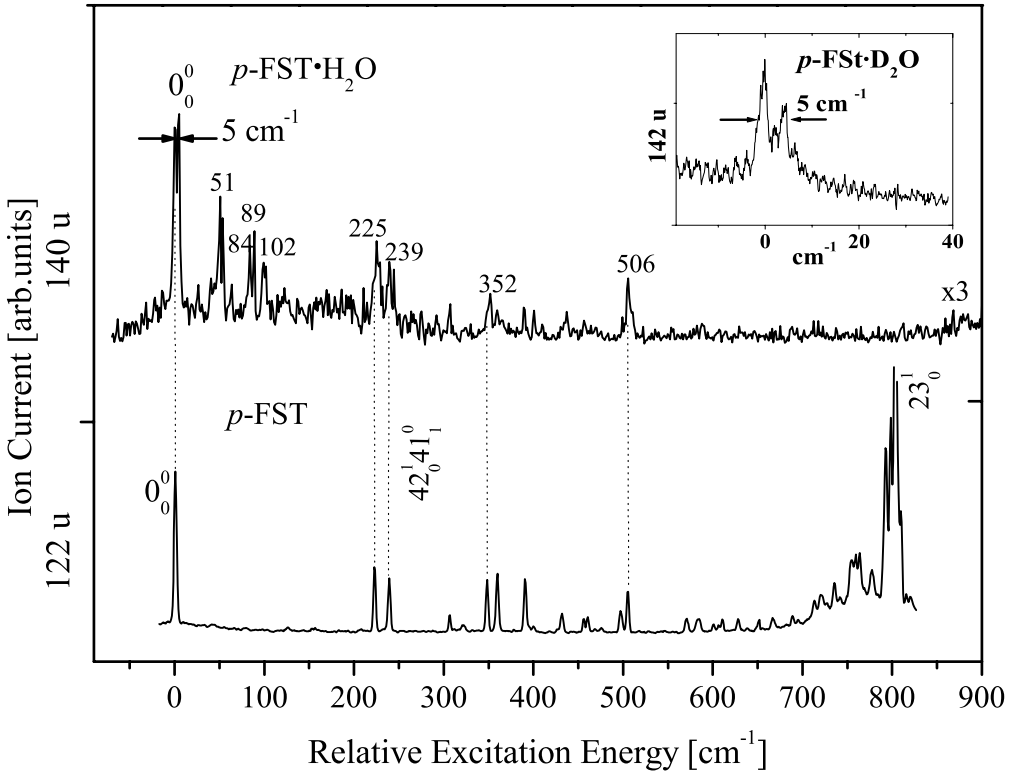

Figure 9.2: *R2PI spectrum of the $S_1 \longleftarrow S_0$ transition of jet-cooled p-FST (top) recorded at m/z = 140 mass channel and pFST·H_2O (bottom) recorded at m/z = 122 mass channel as a function of the relative excitation energy. The $S_1 \longleftarrow S_0$ 0_0^0 origin band of the p-FST·H_2O complex is at 34 416 cm^{-1}. The inset shows the profile of the $S_1 \longleftarrow S_0$ origin band of p-FST·H_2O at 34 421 cm^{-1} recorded at m/z = 142 mass channel.*

smaller than that in the *p*-FST·H_2O cluster. Furthermore, the higher ST·$(H_2O)_n$ clusters [$n > 1$] show extensive fragmentations and the band intensities of the 1:1 cluster appear in the spectrum very weakly [214]. Such fragmentation behaviour has been also reported for benzene-water clusters. On the contrary, the 1:1 *p*-FST·H_2O cluster is quite stable and no fragment signal was noticed in the monomer mass channel when the excitation frequency of the laser was scanned across the 0_0^0 band of the *p*-FST·H_2O complex. This provides an indication that the binding pattern of water to *p*-FST is different from that ofs ST. Mahmoud et *al*. have performed an *ab initio* quantum chemistry calculation for structural prediction of the ST·H_2O complex using a relatively low level of theory (HF/6-31+G (2*d*, *p*)), which favoured a π-hydrogen-bonded complex where both of the water hydrogen atoms point to the aromatic π-electron cloud. To our knowledge, no high level theoretical calculation has been attempted so far on the ST·H_2O cluster system.

It is instructive to compare the observed spectral blue shift of the 0_0^0 band of the *p*-FST·H_2O dimer (104 cm^{-1}) with the ones of the fluorobenzene·water (+118 cm^{-1}) [270,276], *p*-difluorobenzene·water

(+167 cm^{-1}) [277], and benzene-water (+50 cm^{-1}) 1:1 complexes [275]. Because of the increasing blue shift, it appears that fluorination of the aromatic ring destabilizes the excited electronic states of the above 1:1 clusters with water, compared to their respective ground states. Recently, we have performed a complete active space self-consistent field (CASSCF) calculation on *p*-FST and related systems in the ground and excited states. The results show that the partial charge on the electronegative F atom in *p*-FST monomer is smaller in S_1 than in S_0 electronic state [278]. Thus, the prediction of the CASSCF calculation provides a qualitative explanation for the observed blue shifting of electronic transition energy of the *p*-FST·H_2O complex, assuming that the O-H bond of water is σ-hydrogen-bonded to the F atom of the *p*-FST in the complex. A more rigorous calculation is required to explain the trends of the blue shift among the different fluorobenzene·water clusters mentioned here. Recently, Brutschy and co-workers have investigated the binding of water molecules to fluorobenzene using infrared ion-depletion spectroscopy [276]. In the FBzn·H_2O cluster, the IR spectral features of the water ν_1 and ν_3 modes are quite simple, and unlike the benzene-water complex, no splitting of these bands has been observed. In the latter complex, the antisymmetric stretching mode (ν_3) of the water exhibits a complex spectral splitting due to its simultaneous rotation and rocking motions about the six-fold axis of the benzene ring [213]. On the basis of these contrasts in spectral pattern in the two systems, the authors have inferred that the water molecule in the FB·H_2O complex is symmetrically placed on top of the ring wherein both hydrogen atoms point to the aromatic π-electron cloud. The simple IR spectrum of the FBzn·H_2O complex was interpreted as due to hindrance of the water rotation by the local dipole moment induced by the fluorine atom. However, in a later theoretical study, Tarakeshwar, et *al*. suggested a co-planar structure for the complex, in which the O-H of the water molecule forms a six-membered H-bonded (σ-type) ring system with the F-C-C-H of the phenyl ring. In the present case of the *p*-FST·H_2O system, the reduced π-electron density on the ring due to the electron attracting fluorine atom can be partially compensated by the electron releasing mesomeric effect of the vinyl group. As a consequence, the π- and σ- type hydrogen bonding of water with the solute *p*-FST could be equally probable and this is consistent with the predictions of only a small energy difference made by our *ab initio* theoretical calculations (see Table 9.1). From the calculation of the binding energies alone, it is not possible to identify the structure of the *p*-FST·H_2O cluster present in the molecular beam. To identify the realized structure and to provide additional information to the ongoing discussion on the type of the hydrogen bonding in fluorinated aromatic molecule-water complexes, high-resolution experiments on *p*-FST·H_2O were performed.

9.3.3 High Resolution Spectrum of the 0_0^0 Origin Band of the *p*-FST·H_2O Cluster

The high-resolution spectrum of the 0_0^0 origin band of the *p*-FST·H_2O cluster located at 34416.004(5) cm^{-1} and measured at its mass (m/z = 140) channel is depicted in Fig. 9.3 (upper trace). The spectrum is characterized by well-pronounced P and R branches, and a weak central Q branch. It features a prominent central dip and a typical periodic structure in the P branch. The spectrum is referred to as a hybrid *a* and *b* type [94]. The observed peaks are formed by aggregations of single rotational lines and their smallest width is about 300 MHz. This necessitated the application of the computer-assisted fit (see Sect. 6.3) of the experimental spectrum to derive the rotational constants and the transition moment ratio. To aid the GA fit, described in Sec. 6.3, the four positions of the water molecule with respect to the benzene ring as predicted by the *ab initio* calculations were assumed and used as starting geometries: two in-plane, and two out-of-plane, respectively. In the first step, a reasonable fit was achieved only for the *anti* in-plane conformer. For further improvements, a planarity condition for this conformer was imposed to the fitting program as a physical constraint restricting the multidimensional search space. The result of this fit is also presented in Fig. 9.3 (lower inverted trace). It was obtained by convoluting the theoretical stick spectrum by a Gaussian profile with a linewidth of 220 MHz.

The rotational energy levels were calculated on the basis of the asymmetric top Watson Hamiltonian [221–223]. Both rotational band contour and most of the typical features of the experimental spectrum are well reproduced by the simulation. The broad linewidth of 220 MHz necessary to convolute the stick spectrum making it match the experimental one is tentatively ascribed to a saturation of the observed transitions rather than to a lifetime broadening. The resulting rotational constants for the ground, S_0, and the first excited, S_1, electronic states, and the transition moment ratio are listed in Table 9.2.

The rotational temperature has been found to be 5.5 K. The transition moment ratio is $\mu_a^2 : \mu_b^2 : \mu_c^2$ = 55:45:0, which agrees with the hybrid character of the spectrum. On the basis of the best fit of our highly resolved spectrum obtained by employing the parameters of conformer III as starting conditions for the fit, one infers that the measured signal of the 0_0^0 origin band of the *p*-FST·H_2O cluster originates from this conformer. This is in accord with the theoretical predictions showing that this is the most stable conformer. The experimentally found transition moment ratio of the *p*-FST·H_2O complex (*a*:*b* = 55:45) is different, though not very much, from the one of the bare molecule ($\mu_a^2 : \mu_b^2 : \mu_c^2$ = 67:33:0) [279]. This finding can be interpreted merely as a mass effect causing a rotation of the coordinate frame due to the attachment of the water molecule. The direction of the transition moment with respect to the aromatic ring is not changed by the σ-hydrogen-bonding of the water molecule. This explanation asserts that there are no pronounced electronic effects involved in the microsolvation by the attachment of one water molecule, and what is observed is a local excitation of the *p*-FST monomer remaining unaffected by the water

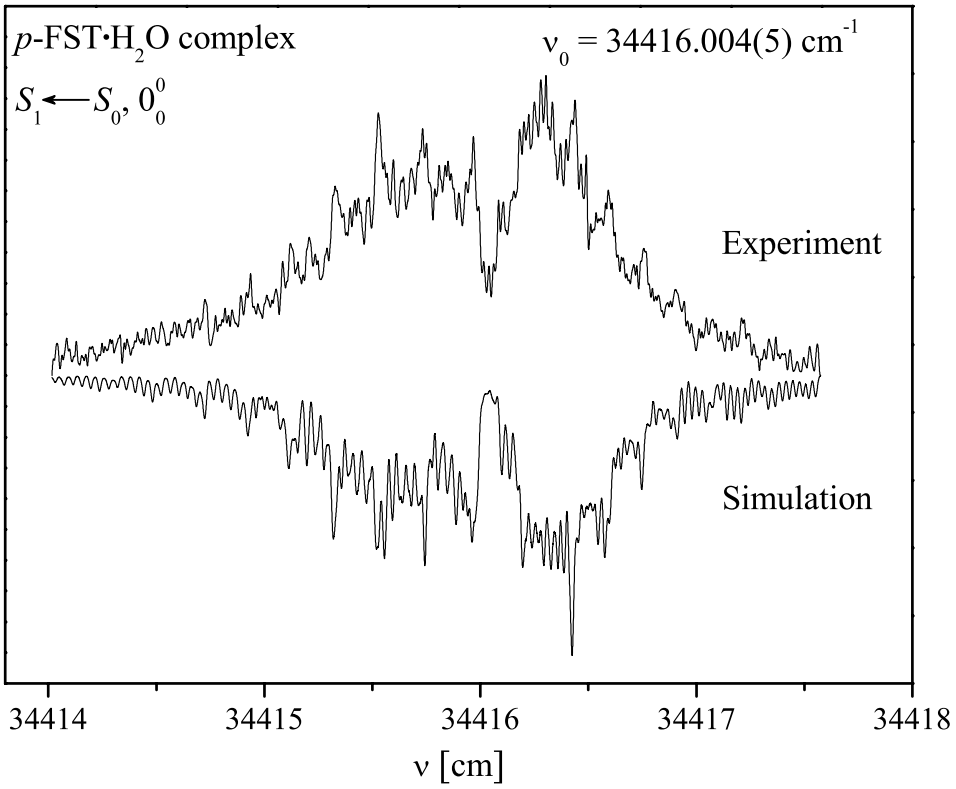

Figure 9.3: *Highly resolved spectrum of the 0_0^0 origin band of the $S_1 \longleftarrow S_0$ electronic transition of the pFST·H_2O cluster at ν_0 = 34416.004(5) cm^{-1} recorded at m/z = 140 mass channel. Upper trace: experimental spectrum. Lower inverted trace: the best-fit simulated spectrum yielding the constants listed in Table 9.2. For details, see text.*

Rotational Constant	Ground state S_0		Excited state S_1	
	MHz	cm^{-1}	MHz	cm^{-1}
A	3215(12)	0.10924(40)	3211(15)	0.10713(52)
B	592(15)	0.01977(51)	586(16)	0.01957(55)
C	502(11)	0.01674(37)	496(12)	0.01655(40)
TM ratio, $\mu_a^2 : \mu_b^2 : \mu_c^2$	55:45:0			
Origin ν_0, cm^{-1}	34 416.004(5)			

Table 9.2: *Experimental rotational constants of the p-FST·H_2O cluster giving rise to the 0_0^0 origin band of the $S_1 \longleftarrow S_0$ electronic transition (see Fig. 9.2). The rotational constants and the transition moment ratio were obtained through computer-aided fit of the highly resolved spectrum (Fig. 9.3) of this conformer (for details, see text). The numbers in parentheses represent one standard deviation in units of the least significant digit. The uncertainty for the relative values of μ_a^2, μ_b^2, and μ_c^2 in the TM ratio is 4%.*

complex formation. This conclusion conforms to the recent high-resolution results of Pratt and coworkers [133] on the *p*-difluorobenzene·water complex where the structure of the complex is also planar and the attachment of water does not influence the orientation of the transition moment relative to the monomer reference frame. To explain the nature of the second peak of the origin band located 5 cm^{-1} to the blue side (34421 cm^{-1}) of the main peak, a high-resolution experiment also for this peak was carried out. The lower ion signal intensity, however, did not allow us to measure a well-resolved spectrum and for this reason, the rotational fit analysis described above was not applicable in this case. Comparing the measured rotational contour of this band with the ones simulated with the parameters for the two out-of-plane conformers (I and II) and for conformer IV without making a fit, it was found that the spectrum of the in-plane conformer IV exhibits the closest similarity with the experimental result. On this basis, we tentatively assert that the blue-shifted sub-band can be the origin band of the *gauche* in-plane conformer (conformer IV).

9.4 Summary and Conclusions

Both low- (0.4 cm^{-1}) and high-resolution (0.003 cm^{-1}) R2PI spectra with mass selection of the singly hydrated cluster of *p*-fluorostyrene have been presented. Calculations at the RHF, B3LYP and MP2 levels of theory using 6-311G (*d, p*) basis set predict four stable conformers: two out-of-plane and two in-plane , the latter being more stable than the former by an energy of only about 0.5 kcal/mol. A reasonable fit of the high-resolution spectrum of the 0_0^0 origin band of the $S_1 \longleftarrow S_0$ electronic transition was only produced by employing the rotational constants of the *anti* in-plane conformer (conformer III) as starting parameters. For this reason, we infer that conformer III is the most abundant one in the molecular beam. From the measured transition moment ratio we find that the binding of water does not cause a reorientation of the transition moment with respect to the aromatic ring, which implies that σ-bound water does not induce a noticeable π-electron structure rearrangements. The gross rotational structure of the second 5 cm^{-1} blue-shifted peak of the main band is more similar to the rotational structure characteristic for an in-plane configuration rather than to the more different rotational contour of a π-hydrogen bonded out-of-plane conformer. In this way, we rule out the possibility of an out-of-plane conformer and tentatively explain the origin of this sub-band either as due to a sequence transition of the *anti* in-plane conformer or due to the *gauche* in-plane conformer. This means that due to the subtle interplay between the electron attraction of the electronegative fluorine atom and the electron releasing mesomeric effect of the vinyl group both π- and σ-type hydrogen bonding of water with *p*-fluorostyrene are feasible but the energetically slightly favoured σ-type hydrogen bonding of the water proton with the fluorine atom is dominating in this case.

Chapter 10

Specific and Nonspecific Interactions in a Flexible Molecule: 2-phenylethanol and its Complex with Argon

S. Chervenkov, R. Karaminkov, J. E. Braun, H. J. Neusser, S. S. Panja, and T. Chakraborty, J. Chem. Phys. **124**, 234302 (2006).

The conformational structure and transition moment orientation in 2-phenylethanol and its 1:1 clusters with argon have been determined by high-resolution R2PI spectroscopy in combination with genetic-algorithm-based computer-aided rotational fit analysis and ab initio quantum chemistry calculations. The results clearly demonstrate that the gauche structure of 2-phenylethanol, which is stabilized by the intramolecular π-hydrogen bond between the folded side chain and the benzene ring, is the most abundant in the cold molecular beam. In this conformer the transition moment is rotated by 18° from the short axis of the aromatic ring. Two distinct 1:1 complexes of 2-phenylethanol with argon in a cis- and trans- configuration with respect to the side chain have been found. By employing the Kraitchman analysis it has been found that the structure of the 2-phenylethanol moiety and the orientation of the transition moment do not change after the complexation with argon within the experimental accuracy. From the measured band intensities, it can be concluded that in addition to the dispersion interaction of the argon atom with the aromatic ring a hydrogen-bond-type interaction with the terminal OH group of the side chain stabilizes the cis structure of the 1:1 complex of 2-phenylethanol with argon.

10.1 Introduction

2-phenylethanol (2-PE) is the hydroxy analogue of the simplest aromatic amine neurotransmitter, 2-phenylethylamine. The molecule consists of an aromatic ring and a flexible side chain with a terminal alcoholic group. In recent years, much effort has been devoted to understanding the conformational behavior of a variety of such flexible biomolecules in the gas phase. Under isolated conditions, the molecular conformation is determined by a balance of interactions between different groups within the molecules. However, to perform biological functions, the molecule has to dock to a receptor site where the binding, mostly, occurs through noncovalent interactions, like hydrogen bonding as well as pure dispersion interactions. Therefore, it is of paramount importance to know not only the most favorable conformations of the bare biomolecules [126, 127, 129, 180, 201, 280–287] but also their conformational preferences in the presence of other species [126, 129, 160, 280, 288].

In the case of bare 2-PE, recent spectroscopic measurements and theoretical calculations [126, 160, 283, 284, 287] indicate that its most favoured conformation in the electronic ground state corresponds to a *gauche* geometry. The primary factor that stabilizes this conformeric structure is a nonclassical π-hydrogen bonding of the terminal alcoholic group of the side chain with the aromatic ring. Calculations indicate that the binding energies of such hydrogen bonds are nearly an order of magnitude smaller compared to the classical X-H$\cdots$Y type hydrogen bonds (see Sec. 1.4). However, recent measurements in our group using mass selective threshold ionization spectroscopy have shown that the binding energy of the intermolecular π- hydrogen-bonded indole-benzene complex is in the range of *ca*. 1600 cm^{-1}, which is similar to the classical hydrogen bond energy [153, 289]. A direct identification and assignment of the *gauche* structure of 2-PE by rotationally resolved UV spectroscopy is still missing. Here, high-resolution measurements of the main band allowing for an unequivocal identification of the respective conformational structure of 2-PE are presented. Furthermore, in the present study, as a first step, the 1:1 complex of 2-PE with Ar has been chosen as a convenient model system to learn how the subtle balance of π- hydrogen bonding and dispersion interactions determine the preferred conformation of this dimeric adduct. The method of high-resolution UV spectroscopy has been used here for the first time to investigate the structure of the 1:1 Ar complex of such a flexible side-chain-containing biologically relevant molecule. In this way, one is able to compare this result with previous high-resolution spectroscopy results of clusters of benzene (Bzn) with Ar [248, 253]. For the latter, it has been demonstrated that a (1|1) type conformation in which one Ar atom is on top of either side of the aromatic ring is favoured over the (2|0) type conformation, even though the (2|0) configuration may be stabilized by the Ar-Ar interaction [253]. In the Bzn·Ar case, both sites are completely equivalent. Similarly, in the present case of 2-PE, for the preferred binding site, we have to consider not only the nonspecific interaction of Ar with the aromatic ring but also the specific hydrogen-bond-type interaction with the OH group of the side

chain [160, 288]. There are three distinct possibilities that must be considered: *i*) preserving the *gauche* conformation of the side chain, the Ar atom can bind to the aromatic ring at the opposite side of the OH, *ii*) the Ar atom is attached to the ring on the same side of the OH group, and *iii*) the Ar atom binding to the aromatic ring makes the side chain change its structure, assuming an extended geometry. To ascertain which scenario(s) is realized in the conditions of the cold molecular beam, high-resolution experiments have been carried out.

10.2 Experiment and Data Processing

The low-resolution spectra of 2-PE and its complexes with Ar as well as the high-resolution spectra of 2-PE and the 2-PE·Ar complex have been measured by R2PI spectroscopy with mass selection in a supersonic jet-cooled molecular beam using the experimental set up thoroughly descrbed in Sec. 6.2. The Ar^+ion laser was operating at 488 nm yielding output power of 4 W necessary to pump the ring dye laser. The latter was using Coumarin 521 dye achieving an output power of 250 mW.

For the analysis and interpretation of the measured highly resolved spectra of the 2-PE monomer and the 2-PE·Ar complex, the computer-assisted fitting routine based on genetic algorithms (see Sec. 6.3) has been employed. For the fits of both spectra, 500 generations with 500 individuals in each were used. The attained best-fit cross correlations are 97% and 95% for the 2-PE monomer and the 2-PE·Ar complex, respectively.

10.3 Experimental Results

10.3.1 Low Resolution Spectrum

The low-resolution one-colour R2PI spectrum in the vicinity of the origin of the $S_1 \longleftarrow S_0$ electronic transition of the 2-PE monomer is shown in Fig. 10.1. It was recorded under water-free conditions by selecting the ion signal at the parent (m/z = 122) mass channel. During the scan, no signal at smaller mass channels was observed, which demonstrates that (unlike ephedrine [201]) 2-PE does not fragment upon ionization even under the conditions of a one-colour experiment with a total excitation energy of 75200 cm^{-1}. This is not surprising since an excess energy of 3690 cm−1 above the adiabatic ionization energy (AIE) is expected from the data for the AIE (71550 cm^{-1}) published recently by Weinkauf et *al*. [290]. The absorption of several photons in the 2-PE cation is not expected for the small laser intensities that were used. The spectrum in Fig. 10.1 is dominated by a high-intensity peak A, which has been interpreted

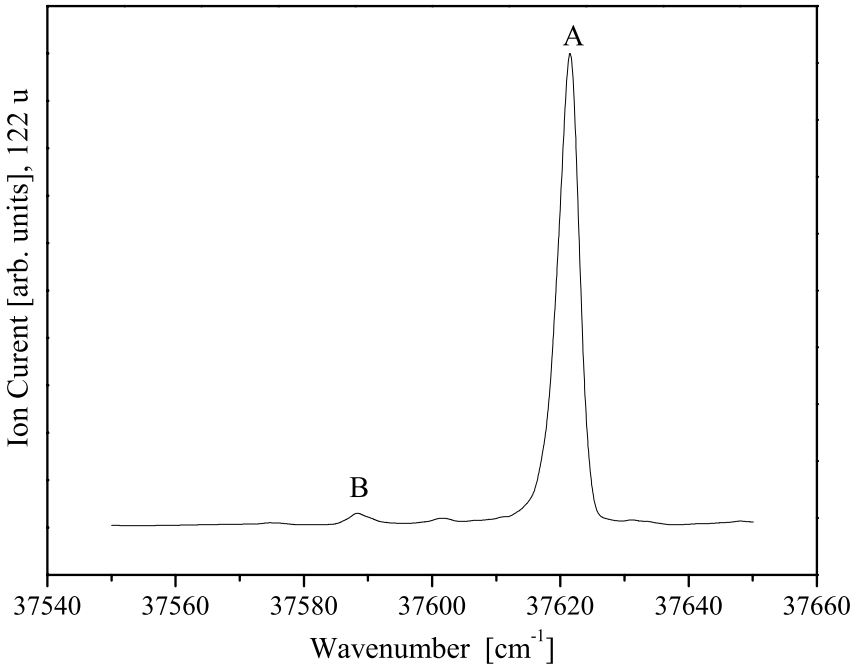

Figure 10.1: *One-colour R2PI spectrum of the $S_1 \longleftarrow S_0$ electronic transition of 2-PE seeded in Ar, and recorded at the monomer (m/z=122) mass channel. Peak A is the strongest band in the $S_1 \longleftarrow S_0$ spectrum. For explanation of peak B, see text.*

as the origin band of the most abundant conformer of the 2-PE monomer [126, 160, 284, 287]. A number of weaker features on the blue side (not shown in Fig. 10.1) have also been observed, and they are supposed to originate from vibrational modes of the same conformer, from different conformers, or else, from hydrated complexes [160, 287]. It is interesting to observe also a weak band B, which is red-shifted by *ca*. 30 cm^{-1} with respect to the main band. There are two possible explanations for its appearance: *i*) due to hot bands or *ii*) resulting from the 2-PE·Ar complex after fragmentation since no signal at the 2-PE·Ar mass (m/z=162) channel was detected. The red shift of this band is similar to the red shifts measured for other aromatic molecule-Ar clusters [87], and for this reason, the second explanation appears to be more plausible. Experiments using He as a carrier gas were attempted but in this case the band in question was not observed. To demonstrate the *gauche* structure of the 2-PE monomer giving rise to the main band A and to investigate the structure of the 2-PE·Ar complex, high-resolution R2PI experiments of the two discussed bands combined with *ab initio* calculations were performed.

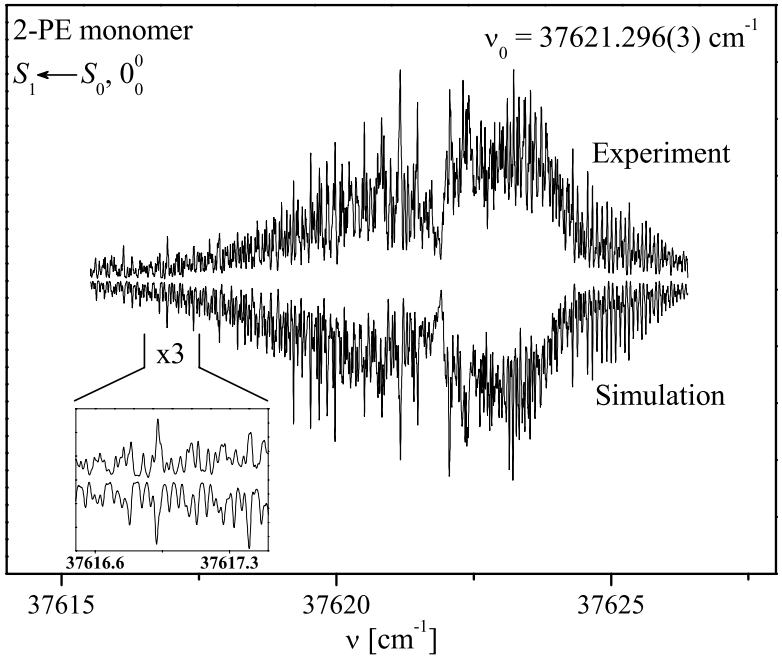

Figure 10.2: *High-resolution two-colour UV R2PI spectrum of peak A in Fig. 10.1. It is assigned as the $S_1 \longleftarrow S_0$ 0_0^0 origin band of the gauche conformer of 2-PE with the rotationless transition centred at 37621.296(3) cm^{-1}. The spectrum is recorded at m/z=122 mass channel. Upper trace: experimental spectrum. Lower inverted trace: the best-fit simulated spectrum yielding the constants listed in Table 10.1 (for details, see text). The inset shows a magnified portion of the experimentally highly resolved spectrum and the best-fit simulated spectrum.*

10.4 High Resolution Spectra

10.4.1 Main Band

The highly resolved UV spectrum of the strongest band A at 37621 cm^{-1} of the 2-PE monomer is shown in Fig. 10.2 (upper trace). It manifests a pronounced rotational structure covering a range of about 10 cm^{-1}, indicating a relatively high rotational temperature in the molecular beam. It is worth to point out, however, that the excitation of high J levels did not deteriorate the quality of the rotational structure of the band. The spectrum is characterized by a central dip, a weak central Q branch on the red side of the dip, and very well pronounced P and R branches. The spectrum reveals a hybrid *a*-, *b*-, and *c*- type character with the *b* contribution dominating. It does not feature single rotational lines but rather aggregations of the latter forming sharp peaks with FWHM of about 150 MHz. The rotational constants for the ground, S_0, and the first excited, S_1, electronic state as well as the transition moment ratio, the rotational temperature and the 0_0^0 position, ν_0, have been determined by the computer-assisted procedure described

in Sec. 6.3. The fit was started with the rotational constants in the ground state known from microwave experiments [283] and restricting the search space for these constants within 0.5 % of their initial value. The search space for the rotational constants in the excited state and that for the other parameters was retained broader. The resulting theoretical stick spectrum was convoluted using a Gaussian line shape with a FWHM of 150 MHz. The best-fit simulated spectrum is also shown in Fig. 10.2 (lower inverted trace). There is a close match in both peak positions and peak intensities, as seen in the inset of Fig. 10.2, showing a magnified part of the spectrum. The experimentally obtained values of the rotational constants, the transition moment ratio, and the rotational temperature are detailed in Table 10.1.

Rotational constant	Ground State S_0		Excited State S_1	
	GHz	cm^{-1}	GHz	cm^{-1}
A	3.3380(74)	0.11134(25)	3.2377(54)	0.10800(18)
B	1.0835(71)	0.03614(24)	1.0673(69)	0.03560(23)
C	0.9589(54)	0.03199(18)	0.9340(57)	0.03116(19)
TM ratio $\mu_a^2 : \mu_b^2 : \mu_c^2$	18:74:8			
Origin ν_0 , cm^{-1}	37621.296(3)			
Temperature T , K	12.5(3)			
Best-fit cross correlation (%)	97			

Table 10.1: *Experimental rotational constants, transition moment ratio, origin band position ν_0, and rotational temperature, T, of the gauche conformatin of the 2-PE monomer resulting from the GA- based computer-aided fit of the highly resolved spectrum of the $S_1 \longleftarrow S_0$ 0_0^0 origin band (see Fig. 10.1 and Fig. 10.2) (for details, see text). The numbers in parentheses represent one standard deviation in units of the least significant quoted digit. The uncertainty for the relative values of μ_a^2, μ_b^2, and μ_c^2 in the transition moment ratio is 4.*

The deviation of our experimental ground state rotational constants from those found from microwave experiments [283] is within the accuracy of the fit of our experiment. There is a very good agreement between the values of the rotational constants in Table 10.1 and those found by *ab initio* calculations for the *gauche* conformer [126, 283] for both the ground, S_0, and the first excited, S_1, electronic state. On the other hand, the experimental transition moment ratio from this high-resolution R2PI experiment ($\mu_a^2 : \mu_b^2 : \mu_c^2$ = 18:74:8) differs considerably from the one theoretically predicted at the CIS/6-31G (*d*) level [126] ($\mu_a^2 : \mu_b^2 : \mu_c^2$ = 2:96:2). It differs also from the theoretical predictions at the CIS/6-31G (*d*, *p*) level (see Table 10.3), the theoretical results asserting that the transition moment ratio is oriented along the *b* principal axis of inertia. The transition moment ratio obtained on the basis of the low-resolution rotational band contour analysis of Ref. [160] ($\mu_a^2 : \mu_b^2 : \mu_c^2$ = 0:88:12) also differs from the discussed high-resolution spectroscopy result, though the disagreement in this case is less pronounced. It is interesting to point out the discrepancy in the *a* and *c* contributions. While the low-resolution band contour

analysis states there is no *a* type contribution and there exists a weak *c* type, the high-resolution results clearly show that there are both *a* and *c* -type components of the highly resolved spectrum. To explain the discrepancies of the transition moment orientation, *ab initio* quantum chemistry calculations with an extended basis set of the S_1 excited electronic state of the 2-PE monomer at the CIS/6-311++G (*d*, *p*) level of theory were performed. The transition moment ratio in this case is $\mu_a^2 : \mu_b^2 : \mu_c^2$ = 19:72:9, and it conforms very well to the experimental result obtained from the fit of the highly resolved spectrum.

10.4.2 Red-shifted Band

In Fig. 10.3, the weak band B at 37589 cm^{-1} is shown when measured under high resolution at m/z=122. Assuming that it originates from a 1:1 complex of 2-PE with Ar, an attempt was made to measure the high-resolution spectrum of this band at the 2-PE·Ar complex mass (m/z = 162) channel. Unfortunately, even under the conditions of the two-colour experiment with a stepwise decrease of the energy of the ionization photon, a strong enough signal at this mass channel was not sobserved, and for this reason, the highly resolved spectrum of band B was recorded at the 2-PE monomer mass (m/z = 122) channel. Only under high resolution, it becomes apparent that this band consists of two subbands, shown in the upper trace of Fig. 10.3 a) and in Fig. 10.3 b), respectively, which are not resolved as separate features in the low-resolution spectrum of Fig. 10.1. Their rotational structures are similar to each other but completely different from the one of the strongest peak A, shown in Fig. 10.2. Both highly resolved spectra in Fig. 10.3 feature a very intense central Q branch. The stronger peak, shown in Fig. 10.3 a), has a steep rise on the red side and a typical shading on the high-energy side. In addition, it features weak P and R branches composed of very well-resolved regularly spaced features. Therefore, the spectrum in Fig. 10.3 a) can be referred to as a predominantly *c* type, which is completely different from the *b*-type main band A in Fig. 10.2. The Q branch of the weaker subband seems to have a reversed shading with the steep rise on the blue-energy side (See Fig. 10.3). In this case, the P and R branches are very weak and noisy, and with a somewhat different, less regular, structure compared to that of the stronger subband but the overall profile is very similar to the one of the spectrum in Fig. 10.3 a), and the weaker subband can be assigned also as a predominantly *c* type.

To analyse both spectra, the automated fit based on genetic algorithms described in Sec. 6.3 was applied. The first step is to find reasonable starting values for the rotational constants. Constraints on the starting values of the rotational constants in the ground state were imposed. This was done in the following way: A plausible reason for the different rotational structure is a switching of the principal axes of inertia if a heavy atom is attached to the 2-PE molecule in an out-of-benzene-ring-plane position. Then, the *c* axis of the complex does no longer coincide with the *c* axis of the monomer. This implies that even if it is assumed that no change of the orientation of the transition moment relative to the 2-PE molecular framework occurs upon complexation with Ar, the

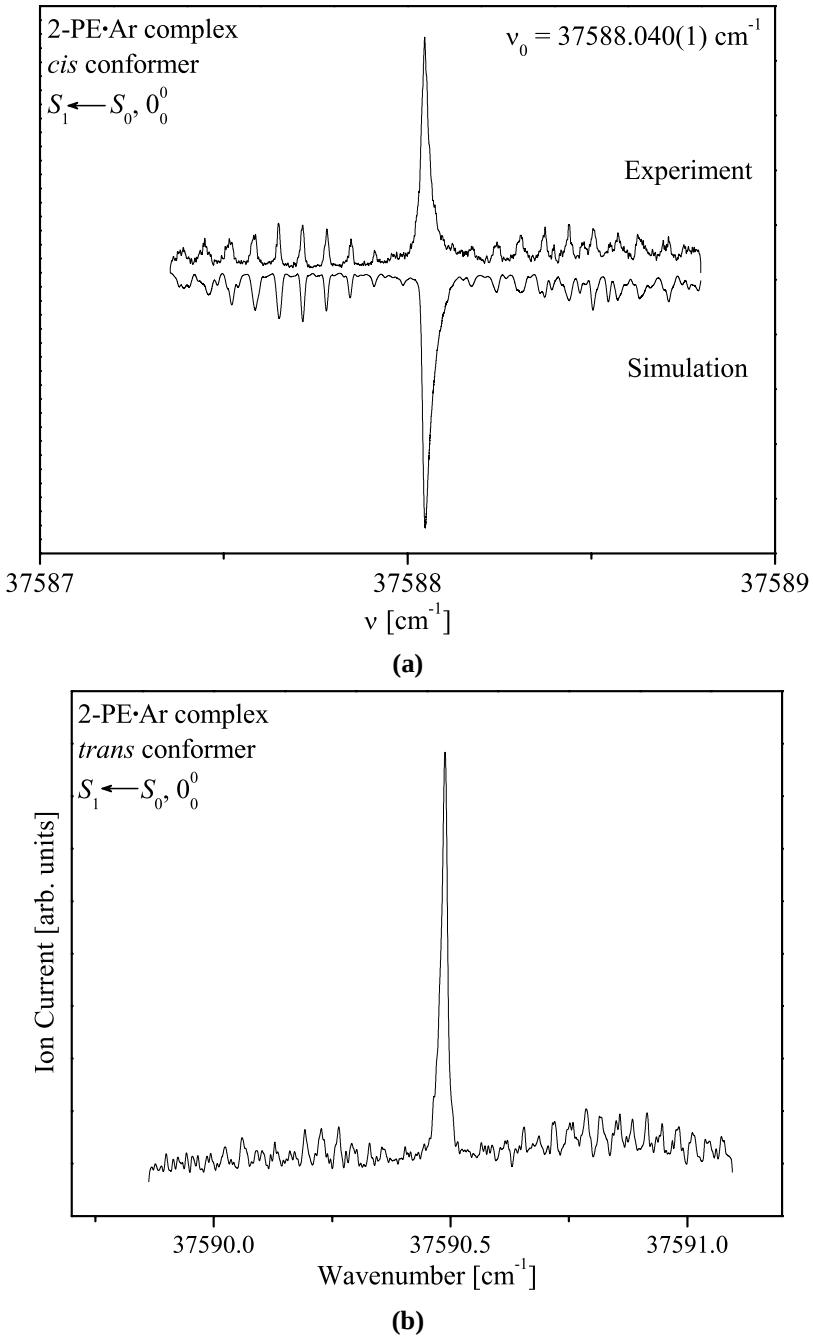

Figure 10.3: *High-resolution two-colour UV R2PI spectrum of peak B in Fig. 10.1. The disclosed two subbands are assigned to two different 2-PE·Ar complexes: (a) cis-complex (ν_0 = 37588.040(1)cm^{-1}) and (b) trans-complex (ν_0 = 37590.5cm^{-1}). Upright spectra in (a) and (b): experimental spectra. Inverted spectrum in (a): the best-fit simulated spectrum yielding the constants listed in Table 10.2*

projections of the transition moment onto the principal axes of inertia of the 2-PE·Ar cluster will be different, which leads to a different transition moment ratio and hence to a different rotational band structure [94]. Assuming that the two subbands originate from fragmentation of a 2-PE·Ar complex, two feasible positions of the Ar atom with respect to the benzene ring are reasonable: *i*) the Ar atom is atop of the benzene ring on the side of the side chain (*cis* cluster conformer) , and *ii*) the Ar atom is on the other side of the benzene ring located on its C_6 symmetry axis (*trans* cluster conformer) . The distance between the Ar atom and the benzene ring was taken from Refs. [87, 291]. For these two configurations, two sets of rotational constants were obtained, which were used to calculate the corresponding rotational band structures. The so-produced two spectra exhibit the same rotational band type but their rotational structures are different for the two sets of starting values: the one with the Ar adjacent to the side chain (*cis* configuration) displaying a regular structure with peak spacing close to the one of the experimental spectrum of the stronger subpeak (Fig. 10.3 a) while the calculated spectrum for the *trans* configuration of Ar showing irregularly more closely spaced peaks in both P and R branches, resembling the pattern of the weaker experimental sub-band (Fig. 10.3 b). These two sets were used as starting parameters for the GA fits of the experimental spectra. The FWHM of the Gaussian line used to convolute the stick spectra was 150 MHz. Unfortunately, because of the insufficient quality of the experimental spectrum, the fit of the weaker (higher-energy) subband did not yield reliable results. The rotational constants from the fit of the band in Fig. 10.3 a) for the ground, S_0, and the first excited, S_1, electronic states , respectively, the transition moment ratio, the rotational temperature, T, and the exact position of the 0_0^0 transition for the *cis* configuration are summarized in Table 10.2. The best-fit spectrum for this configuration is presented in Fig. 10.3 a) (lower

Rotational constant	Ground State S_0		Excited State S_1	
	GHz	cm^{-1}	GHz	cm^{-1}
A	1.018(10)	0.03396(34)	1.0451(92)	0.03486(31)
B	0.954(11)	0.03182(38)	0.9330(56)	0.03112(19)
C	0.6187(51)	0.02064(17)	0.6293(52)	0.02099(17)
TM ratio $\mu_a^2 : \mu_b^2 : \mu_c^2$	14:3:83			
Origin ν_0 , cm^{-1}	37588.040(1)			
Temperature T , K	2.2(3)			
Best-fit cross correlation (%)	95			

Table 10.2: *Experimental rotational constants, transition moment ratio, origin band position ν_0, and rotational temperature T of the cis conformatin of the 2-PE·Ar complex resulting from the GA- based computer-aided fit of the highly resolved spectrum of the $S_1 \longleftarrow S_0$ 0_0^0 origin band (see Fig. 10.3) (for details, see text). The numbers in parentheses represent one standart deviation in units of the least significant quoted digit. The uncertainty for the relative values of μ_a^2, μ_b^2, and μ_c^2 in the transition moment ratio is 5.*

inverted trace) along with the respective experimental spectrum (upper trace). It reveals a very close match to the experimental one both in peak positions and peak intensities. The found transition moment ratio for this peak is $\mu_a^2 : \mu_b^2 : \mu_c^2 = 14{:}3{:}83$. In the case of the weaker subband, a reasonable visual agreement between the experimental spectrum and a spectrum simulated with the rotational constants of the *trans* structure of the 2-PE·Ar complex with transition moment orientation fixed to that of the 2-PE monomer is observed. On this basis and by the red shift, one can tentatively assign the *trans* 2-PE·Ar complex as giving rise to the second subband. It is interesting to point out that the rotational temperature found for the *cis* 2-PE·Ar complex ($T = 2.2K$) (by the appearance of the spectrum it is very likely that the rotational temperature of the weaker subband is similar) is significantly lower than that for the 2-PE monomer ($T = 12.5K$). The explanation of this finding is that in the case of the 2-PE·Ar complex, due to the low binding energy only the sufficiently cold species survive under the conditions of the molecular beam and give rise to the observed spectrum.

10.5 Theoretical Results

10.5.1 *Ab Initio* Results

To support the structural analysis of the 2-PE·Ar complex, a series of *ab initio* structural optimizations using Gaussian 03 suit of programmes [70] were performed. The high-resolution experiments of this work clearly demonstrate that the strongest band A in the UV spectrum originates from the most stable and the most abundant conformation of 2-PE, i.e., the *gauche* structure, in which the side chain is bent towards the benzene ring (see Fig. 10.4). Because of the red shift of bands B from the main band A (*gauche* structure), it is plausible to assume that the Ar atom is attached to the *gauche* structure of 2-PE. Two feasible binding sites of the Ar atom to the *gauche* 2-PE have been considered: *i*) Ar located in vicinity to the C_6 symmetry axis of the benzene ring adjacent to the side chain (*cis* conformer, Fig. 10.5 a), and *ii*) Ar situated close to the C_6 symmetry axis of the benzene ring on the side opposite to the side chain (*trans* conformer, Fig. 10.5 b). As a first step, a full structural optimization of the ground state of the 2-PE *gauche* conformation of the monomer at the MP2/6-31G (*d*, *p*) level of theory was performed. The theoretical results at this level agree well with those present in the literature [126, 283]. In addition, a full structural optimization of the *gauche* conformation of 2-PE for the first excited, S_1, state at the CIS/6-31G (*d*, *p*) level of theory was carried out. The results of these optimizations, including some typical distances, planar and dihedral angles characterizing the shape and position of the side chain, are listed in Table 10.3. The dihedral angles defining the structure of the side chain are depicted in Fig. 10.4. The so-optimized structure of the 2-PE monomer was used as a starting point for the optimization of its dimers with Ar at the MP2/6-31G (*d*, *p*) level

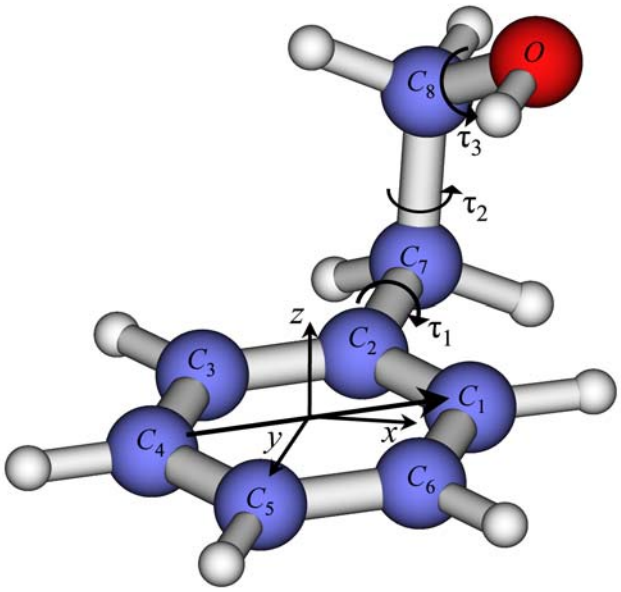

Figure 10.4: *Electronic ground state, S_0, structure of the gauche conformer of 2-PE optimized at the MP2/6-31G (d, p) level of theory. The xyz coordinate system is the benzene-ring-fixed coordinate system with its origin set in the centre of the benzene ring. The curved arrows designate the orientation of the dihedral angles defining the geometry of the side chain (see Table 10.3). The bold arrow shows the orientation of the transition moment relative to the benzene ring.*

of theory, the same as for the monomer, so that a direct comparison of the results is possible.

The optimized structures of the 2-PE·Ar complexes are shown in Fig. 10.5, and the results of the calculations are summarized in Table 10.4. It is obvious that in both structures the Ar atom is not displaced much from the benzene ring symmetry axis. Comparing the results of the structural optimizations of the 2-PE monomer and its two dimers with Ar, it is worth pointing out that the planar and the dihedral angles relevant to the side chain remain unchanged in both 2-PE·Ar conformers, *cis* and *trans* . This is a strong indication that the interaction of the Ar atom is predominantly with the π electronss of the benzene ring and the side-chain structure remains almost intact by the cluster formation. Furthermore, from the *ab initio* calculations, the distance of the Ar atom from the benzene ring plane, and the projections of the Ar atom upon the short and the long axis of the benzene ring for the two 2-PE·Ar complexes have been found. In both binding sites of Ar to 2-PE, this distance is larger (3.75 Å for the *cis* conformer and 3.68 Å for *trans* conformer, respectively) compared to the one in Bzn·Ar (3.58 Å (Ref. [291])), this difference being more expressed in the case of Ar binding next to the side chain (*cis* conformation). This result is not surprising from the viewpoint of the interaction of the benzene ring with the side chain moiety in the 2-PE monomer (*cis* conformer), as will be discussed in the next section.

	Ground state, MP2/6-31G (*d*, *p*)	Excited state, CIS/6-31G (*d*, *p*)
r(H(15)-C(1)), Å	2.55	2.74
α_1(C(2)C(7)C(8)), deg	111	113
α_1(C(7)C(8)O(9)), deg	112	113
α_1(C(8)C(9)C(15)),deg	106	109
τ_1(C(3)C(2)C(7)/C(2)C(7)C(8)), deg	88	90
τ_2(C(2)C(7)C(8)/C(7)C(9)O(9)), deg	61	65
τ_1(H(15)O(9)C(8)/O(9)C(8)C(7)), deg	299	297
A, Ghz / cm^{-1}	3.3359 / 0.11127	3.3584 / 0.11202
B, Ghz / cm^{-1}	1.1118 / 0.03709	1.0631 / 0.03546
C, Ghz / cm^{-1}	0.9637 / 0.03215	0.9192 / 0.03066
TM, $\mu_a^2 : \mu_b^2 : \mu_c^2$	···	1:98:1

Table 10.3: *Theoretical interatomic distances, r, planar angles, α, dihedral angles, τ, and rotational constants for the ground, S_0, and the first excited, S_1, electronic state of the gauche conformer of the 2-PE monomer calculated at the MP2/6-31G (d, p) and CIS/6-31G (d, p) level of theory, respectively. The transition moment ratio, TM, was obtained from a CIS/6-31G (d, p) calculation for the optimized excited state geometry of the 2-PE monomer.*

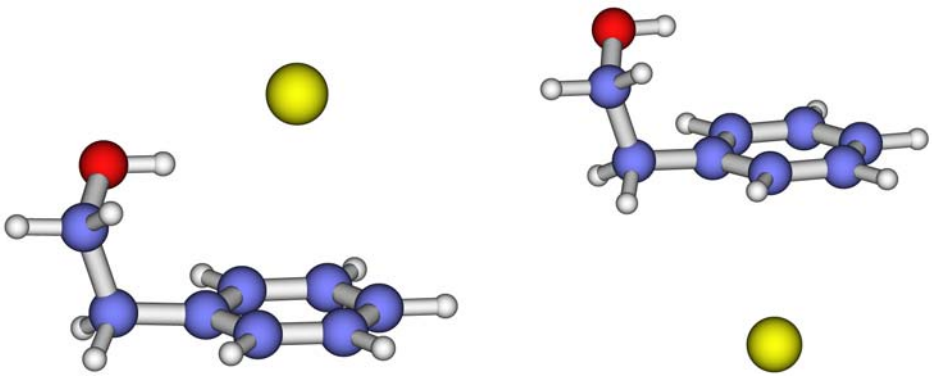

(a) **(b)**

Figure 10.5: *Electronic ground state, S_0, structure of the cis (a) and trans (b) conformer of the 2-PE·Ar complex optimized at the MP2/6-31G (d, p) level of theory.*

10.5.2 Kraitchman Equations

The Kraitchman equations (see Sec. 4.3) have been successfully applied to the analysis of many noble-gas clusters of benzene and benzene derivatives [87–89]. In the case of the flexible side chain molecule 2-PE, this method is also expected to provide reasonable results as the *ab initio* calculations show that the 2-PE molecule indeed does not undergo structural changes due to the complexation with Ar (see Table 10.4). The use of the Kraitchman equations and the comparison of the so-obtained results with those of the *ab initio* calculations can elucidate two important

	cis conformer,MP2/6-31G (*d*, *p*)	*trans* conformer, CIS/6-31G (*d*, *p*)
r(H(15)C(1)), Å	2.55	2.55
α_1(C(2)C(7)C(8)), deg	111	111
α_1(C(7)C(8)O(9)), deg	112	112
α_1(C(8)O(9)H(15)),deg	106	107
τ_1(C(2)C(3)C(7)/C(2)C(7)C(8)), deg	89	88
τ_2(C(2)C(7)C(8)/C(7)C(8)O(9)), deg	61	61
τ_1(H(15)O(9)C(8)/O(9)C(8)C(7)), deg	298	299
r(ArC(5)), Å	70	65
α_4(ArC_5C_2), deg	70	66
τ_4(ArC_5C_2/$C_5C_2C_6$), deg	3	-1
h, Å	3.74	3.68
s_1, Å	0.26	-0.02
s_2, Å	0.08	-0.23
A, Ghz / cm^{-1}	0.9779 / 0.0326	1.4409 / 0.0481
B, Ghz / cm^{-1}	0.9675 / 0.0323	0.5824 / 0.0194
C, Ghz / cm^{-1}	0.6143 / 0.0205	0.5017 / 0.0167

Table 10.4: *Theoretical interatomic distances, r, planar angles, α, dihedral angles, τ, distances from the Ar atom to the benzene ring plane, h, projections of the Ar atom onto x and y axes of the benzene-ring-fixed coordinate system, s_1 and s_2, respectively, and rotational constants for the ground, S_0, and the first excited, S_1, electronic state for the cis and trans conformers of the 2-PE·Ar complex calculated at the MP2/6-31G (d, p) level of theory.*

aspects: *i*) whether indeed the 2-PE molecule retains its structure after the cluster formation, and *ii*) to confirm the theoretical predictions. To use the Kraitchman equations, the rotational constants of the 2-PE monomer and the 2-PE·Ar complex must be known. As a first step, the *ab initio* rotational constants of the 2-PE monomer and 2-PE·Ar complex were used to calculate the Ar atom position from the Kraitchman equations. The resulting Ar position was compared with the theoretically predicted one and this comparison was used as a kind of test for the applicability of the Kraitchman equations in this case. The very good agreement between the two results reveals that the use of the Kraitchman equations is indeed justified in the present study. As a second step, the Kraitchman equations were employed to calculate the experimental Ar atom position using the experimental rotational constants of the 2-PE monomer (main band A) and its *cis* Ar complex (red-shifted band B) , respectively, obtained from the fits of the highly resolved spectra (see Figs. 10.2 and 10.5 a). There exist 8 positions of the substituted atom with respect to the parent molecule, all of them yielding the same set of rotational constants for the cluster. However, not all of these 8 positions are chemically feasible and hence some of them can be ruled out. That is why, only the position of the Ar atom which matches the one theoretically predicted has been considered. The coordinates of the Ar atom with respect to the COM principal axis system of the parent molecule were then transformed into three coordinates relative to the

	cis conformer			*trans* conformer
El. state	S_0		S_1	S_0
Method	Theor.	Expt.	Expt.	Theor.
h, Å	3.74	3.63(32)	3.53(29)	3.68
s_1, Å	0.26	[0.37]	[0.43]	-0.02
s_2, Å	0.08	[0.11]	[0.04]	-0.23

Table 10.5: *Distances from the Ar atom to the benzene ring plane, h, projections of the Ar atom onto x and y axes of the benzene-ring-fixed coordinate system, s_1 ans s_2, respectively, for the ground, S_0, and the first excited, S_1, electronic state for the cis conformer of the 2-PE·Ar complex obtained from the experimental results by employing the Kraitchman equations. The theoretical values of the above parameters for the ground, S_0, state for the cis and trans conformers, respectively, obtained from ab initio calculations at MP2/6-31G (d, p) level of theory are presented for comparison. The numbers in parentheses represent one standard deviation in units of the least significant quoted digit. The experimental values of the displacements s_1 and s_2 are given in square brackets: they are characterized by large deviations (more than 50%) and are presented in the table for completeness.*

benzene ring: distance from the benzene ring, *h*, and displacement along the short and the long axes of the benzene ring, s_1, and s_2, respectively. All these results for the *cis* 2-PE·Ar complex conformation are summarized in Table 10.5. Within the accuracy the agreement between the Ar position relative to the benzene ring derived from the Kraitchman equations and the one obtained from the *ab initio* calculations confirms the result from the *ab initio* calculations that no observable structural changes in the 2-PE monomer occur upon complexation with Ar.

10.5.3 Transition Moment Orientation

The orientation of the TM in a molecule or molecular complex is of importance since it provides information on the electron density distribution. The change of the transition moment orientation may be indicative for the presence of particular types of intra- and intermolecular interactions [292] and hence implications on the conformational structure of the species can be made. To investigate alterations of the TM orientation induced either by conformational distortions or by the attachment of another atom or molecule, one has to eliminate the mass effects, i.e., changing of the principal axes of inertia and hence the projections of the TM caused by the different mass distribution. Towards this end, in the case of the 2-PE monomer the projections of both theoretically predicted (*ab initio* calculations) and experimentally found (GA fit of the rotational structure) TM onto the three mutually orthogonal and normalized axes of a 2-PE molecular-framework-fixed coordinate system were calculated. The same approach was applied to the experimental TM of

	2-PE monomer		2-PE·Ar *cis* conf.
	Theor.	Expt.	Expt.
$\angle x$, deg	18	17(5)	15(5)
$\angle y$, deg	108	106(3)	104(3)
$\angle z$, deg	91	92(4)	93(6)

Table 10.6: *Angles between the transition moment vector and the three unit vectors, x, y, and z of the benzene ring for the 2-PE monomer and the cis conformer of the 2-PE·Ar complex (for details, see text). The numbers in parentheses represent one standard deviation in units of the least significant quoted digit.*

the 2-PE·Ar cluster. In the case of the 2-PE monomer, among the 8 principally possible orientations of the TM yielding the experimentally found TM ratio only one that matches the theoretical predictions was found and it was assigned to be the true TM. For the 2-PE·Ar complexes, no reliable *ab initio* results can be obtained at the level of calculation presented here. However, there exists an orientation of the transition moment deduced from the experimentally determined TM ratio of the *cis* 2-PE·Ar complex that coincides with that of the monomer (See Table 10.6). This result is very unlikely to be explained by an arbitrary coincidence. This means that the van der Waals interaction is too weak to cause a reorientation of the TM itself relative to the molecular framework due to the attachment of the Ar atom. As seen from Table 10.6, the theoretical TM angles relative to the aromatic-ring-fixed axes of the *gauche* conformation of the 2-PE monomer conform very well to the experimental ones within 1°. Their orientation is shown in Fig. 10.4. The observed clockwise rotation of 18° of the transition moment relative to the short benzene axis or the *b* principal axis of inertia of the 2-PE monomer gives rise to the appearance of the *a*-type contribution in the highly resolved spectrum in Fig. 10.2. The deviation of the TM from the short benzene axis can be explained by the interaction of the side-chain hydroxyl group with the π electrons of the benzene ring, which also stabilizes the *gauche* conformer . This interaction brings forward a redistribution of the electron density of the π electrons of the benzene ring, which induces the observed rotation of the transition moment. Such effect is not expected in the case of extended side chain conformations [126], as is shown for the similar system, 3-phenyl-1-propionic acid [292], where the electron density remains the same as in pure benzene. The deviation of the TM away from the short benzene axis can be considered as another evidence for the *gauche* structure of the 2-PE monomer .

10.6 Discussion

The analysis of the highly resolved rotational band structure of the main peak A in the $S_1 \longleftarrow S_0$ spectrum of 2-PE clearly demonstrates that it originates from the *gauche* conformer of 2-PE. Furthermore, the high-resolution spectroscopic investigation of the red-shifted peaks in the spectrum yields important information on the influence of the side chain on the Ar attachment, and vice versa. It has been shown that the two peaks are assigned to the $S_1 \longleftarrow S_0$ electronic origins of the 1:1 van der Waals complexes of 2-PE with Ar, and it is plausible to assume that they appear in the spectrum following fragmentation of the cluster ions generated by vertical ionization leading to a high excess energy above the adiabatic ionization energy and the dissociation threshold of the ionic complex, which is expected from the MATI measurements of the binding energy of Bzn·Ar complexes [293] to be around 575 cm^{-1}. The binding situation may be compared with that of the fairly related system consisting of 1:1 complex of 2-PE with water [160, 288]. Since there a water molecule is involved, the favorable binding sites are likely to be determined by suitability of specific hydrogen bond formations, while in the case of Ar binding to 2-PE, the nonspecific dispersion interaction must be considered. The IR-UV double resonance spectrum of the 2-PE·H_2O species indicates a formation of two isomeric hydrogen-bonded structures [160, 288]. In the first structure, the π-HO hydrogen bond of the *gauche* form of 2-PE is preserved and the water molecule binds to one of the lone pairs of the alcoholic oxygen atom. In the second conformer, the π hydrogen bond between the aromatic ring and the alcoholic OH is bridged by an intercalated water molecule. *Ab initio* quantum chemistry calculation at the MP2/6-31+G (*d*, *p*) level of theory predicts that the two isomeric forms are isoenergetic [160]. In view of these examples where the theoretical information on the energetics is not always sufficient to predict the realized structure, precise high-resolution measurements are necessary, as shown for the 2-PE·Ar complex. Now, the experimental results are compared with the ones of other known Ar complexes of monosubstituted benzene derivatives. The complex with the out-of-plane attachment of Ar used for the spectral simulation is in agreement with the spectral red shift for the $S_1 \longleftarrow S_0$ electronic excitation energy in comparison to other substituted and unsubstituted Bzn·Ar complexes having the same out-of-plane position of the Ar atom [87,294]. The high-resolution scan reveals that the 30 cm^{-1} red-shifted peak in the low-resolution R2PI spectrum actually consists of two adjacent peaks at 33.256 and 30.8 cm^{-1} with an intensity ratio of approximately 2:1. If one interprets the intensity ratio as resulting from a Boltzmann population, it can be inferred that the stronger peak reflects the more stable 2-PE·Ar conformer. This is in line with the somewhat larger red shift pointing to a slightly stronger binding energy. The stronger subband has been identified as the conformer with the Ar atom bound to the aromatic ring on the side of the side chain (*cis* conformer) by analysing the rotational band structure and comparison with the *ab initio* results. It is instructive to compare this spectral shift of the $S_1 \longleftarrow S_0$ transition energy with other Ar complexes of benzene derivatives. For example, the red shifts of the 1:1 and 1:2 complexes of

benzene (Bzn) with Ar are 21 and 41 cm^{-1} [253, 291], for the 1:1 complex of toluene , the shift is 26 cm^{-1} [295], for the 1:1 complex of *p*-fluorotoluene, the shift is 35 cm^{-1} [154], and for phenol, it is 33 cm^{-1} [296]. The result for the red shift of the peak at 31cm^{-1} of this work fits best to the one for phenol·Ar. From the experience of the 1:2 Bzn·Ar complex [253], one may assume initially that the Ar atom may prefer to bind with the aromatic ring on the opposite side of the OH group. However, there are two arguments against this possibility. The OH group of the side chain of this molecule is not oriented directly on top of the aromatic ring and there is room to accommodate an Ar atom on the side of the side chain. Secondly, spectroscopic measurements and theoretical calculations indicate that the Ar atom forms "hydrogen bonds" with water [296,297]. Therefore, in the present case, the Ar binding to the ring on the same side of the OH group is stabilized by dispersion interactions with the ring π-electron cloud and, possibly, also by the hydrogen bonding with the OH group of the alcoholic chain. On the other hand, only the dispersion interactions would be responsible for the binding stability of the *trans* conformer with Ar on the other side of the side chain . Thus, the minor species, which shows a smaller red shift of 30.8 cm^{-1}, and has been identified as the second isomeric form (*trans* conformer), is the one with the smaller binding energy and, expectedly, its red shift is very close to that of the toluene·Ar complex. *Ab initio* calculations at the MP2/6-31G (*d, p*) level of theory show that the two (*cis* and *trans*) structures of the 2-PE·Ar complex are almost isoenergetic, the *trans* one being with slightly higher binding energy (44 cm^{-1}). The so-calculated binding energy difference between the *cis* and *trans* conformations , however, is smaller than the expected accuracy at this level of theory. Therefore, one cannot use this theoretical result for making reliable energetic considerations and conclusions on the conformational preferences. This mode of binding can also be compared with those observed in phenol·water·Ar ternary complexes [297, 298]. As mentioned before, in the 1:1 Ar complex with phenol, the Ar atom binds with the π cloud of the aromatic ring and shows a red shift of 33 cm^{-1} in the electronic spectrum. However, in the phenol·water hydrogen-bonded dimer, wherein the water molecule binds at the phenolic OH site, the incoming Ar atom in the ternary complex prefers to attach at the hydrogen-bonded site and exhibits anomalous spectral shifts. The same situation can also arise in the present OH-π internally hydrogen-bonded molecule 2-PE: the Ar atom prefers to bind at the hydrogen-bonded site in lieu of the alternative possibility. However, the magnitude of the effect is expected to be smaller because of the much weaker OH-π hydrogen bond energy. It is assumed [126, 283] that the 2-PE *gauche* conformer is stabilized by a nonspecific interaction between the side chain and the benzene ring. This interaction causes a decrease of the electron density in the benzene ring thus weakening the van der Waals interaction with the Ar atom. Since the side chain induces a non-symmetrical change of the electron density of the benzene ring, this will lead to a displacement of the Ar atom from the C_6 symmetry axis, which is observed in the results from the *ab initio* calculations (See Table 10.5). The accuracy of the experimental displacements of the Ar atom found from the Kraitchman equations is not sufficient to clearly demonstrate this effect. The values of the displacements given in brackets in Table 10.5 are presented only for

completeness.

10.7 Summary and Conclusions

2-PE, the hydroxy analogue of the neurotransmitter molecule, 2-phenylethylamine and its 1:1 complex with Ar have been investigated by high-resolution resonance-enhanced UV two-photon ionization spectroscopy combined with *ab initio* quantum chemistry calculations. The results on the 2-PE monomer unambiguously demonstrate that its *gauche* conformation is the most abundant one in the jet-cooled molecular beam. This conformer is stabilized by a nonclassical π-type hydrogen bond between the folded side chain and the benzene ring. This statement is further supported by the finding from the high-resolution experiments that in this case the transition moment is rotated by 18° away from the short benzene axis, this being in a good agreement with the results of the extended basis set *ab initio* calculations (CIS/6-311++G (*d*, *p*)). This is a clear indication for a redistribution of the π-electron density in the benzene ring, which originates from the interaction between the OH group of the side chain with the benzene ring. Such effect is not expected in the case of the *anti* conformer of the same species , as demonstrated for *p*-hydroxy-3-phenyl-1-propionic acid [292], since the side chain is far away from the benzene ring moiety and the transition moment orientation remains parallel to the short axis of benzene, as is the case of unsubstituted benzene. Two closely spaced bands red-shifted from the origin band of the *gauche* conformer of the 2-PE monomer have been disclosed by high-resolution spectroscopy. They have been assigned to two distinct 1:1 complexes of the *gauche* 2-PE with Ar: Ar atom situated close to the C_6 symmetry axis of benzene on the side of the side chain (*cis* structure) , and Ar sitting close to the C_6 symmetry axis of benzene but on the opposite side of the side chain (*trans* structure). An important question in the description of protein folding is the influence of the surrounding on the molecular structure. It has been frequently discussed whether the attachment of atoms or molecules to a molecular moiety by intermolecular interactions can lead to a structural change in a molecule, particularly when it is flexible. Here, a prototype molecule with a flexible side chain has been investigated. *Ab initio* calculations and the application of the Kraitchman equations to the experimental rotational constants demonstrate that there occurs no structural change of the 2-PE monomer upon the cluster formation with Ar. The position of the Ar atom in both configurations (*cis* and *trans*) manifests that Ar binds to 2-PE via a dispersion interaction with the π electrons of the benzene ring. The small displacements of the Ar atom from the benzene-ring C_6 symmetry axis, mainly in the *cis* configuration , are a result from the interaction of the 2-PE side chain with the benzene ring leading to a breaking of the symmetry of the π electron density of the latter. It is worth pointing out that the theoretically found distance between the Ar atom and the benzene ring is slightly bigger in the case of the *cis* structure which points to a weaker dispersion interaction between the two moieties. This is a

reasonable result from the point of view that in this case the electron density on this side of the benzene ring is decreased due to the electronegativity of the side-chain OH group. This effect is less pronounced on the opposite side of the benzene ring. It is puzzling, however, that it is the *cis* structure which is more abundant in the molecular beam. One can tentatively explain this fact by assuming the existence of an additional hydrogen-bond type interaction between the Ar atom and the side-chain OH group, which contributes to probably higher binding energy in this case. To summarize, it has been shown that the attachment of a moiety bound by dispersion interaction does not noticeably change the structure of 2-PE, a molecule with a flexible side chain. From this finding, one may infer that the additional nonspecific dispersion interaction involving the π electrons of the aromatic ring does not interfere with the intramolecular hydrogen bonds stabilizing the conformational structure of the flexible molecule. This seems to be the case also for the hydrogen-bond type interaction of the Ar atom with the OH group of the side chain.

Chapter 11

Fragmentation and Conformation Study of Ephedrine by Low and High Resolution Mass Selective UV Spectroscopy

S. Chervenkov, P. Q. Wang, J. E. Braun, and H. J. Neusser, J. Chem. Phys. **121**, 7169 (2004).

The neurotransmitter molecule, ephedrine, has been studied by mass-selective low- and high-resolution UV resonance enhanced two-photon ionization spectroscopy. Under all experimental conditions, an efficient fragmentation upon ionization has been observed. The detected vibronic peaks in the spectrum are classified according to the efficiency of the fragmentation, which leads to the conclusion that there exist three different species in the molecular beam: ephedrine·water cluster and two distinct conformers. The two-colour two-photon ionization experiment with a decreased energy of the second photon leads to an upper limit of 8.3 eV for the ionization energy of ephedrine. The high-resolution (100 MHz) spectrum of the strongest vibronic peak in the spectrum measured at the fragment (m/z = 58) mass channel displays a pronounced and rich rotational structure. Its analysis by the use of a specially designed computer-aided rotational fit yields accurate rotational constants for the S_0 and S_1 states and the transition moment ratio, providing information on the respective conformational structure.

11.1 Introduction

In nature there exist many small and medium-sized molecules acting as regulators of various biochemical processes. A prominent class of such molecules comprises neurotransmitters [299, 300], which communicate information between neurons and play an important role in human body. Typical representatives of these molecules are dopamine, epinephrine (adrenalin), norepinephrine (noradrenalin), serotonin, histamine, glycine, glutamate, aspartate, and the class of ephedra, including ephedrine (EPD), norephedrine, and pseudoephedrine, etc. They have been a subject of intense investigations for more than 80 years since the first neurotransmitter, acetylcholine was discovered, and as a result, a wealth of information on their chemical and pharmacological properties is available nowadays. Neurotransmitters are very flexible molecules and this determines the variety of conformational structures they can assume. It is worth pointing out that the conformational structure can change drastically the properties of the respective molecule and its physiological action. For a better understanding of the interaction mechanisms between neurotransmitters and their receptors [301, 302] and for drug synthesis, a detailed study of the structure and the conformational preferences with precise experimental methods at molecular level is indispensable. A feasible experimental approach in this direction is the implementation of spectroscopic techniques of isolated molecules in the gas phase. On the other hand, the enhancement of the computational power provides a good opportunity for making theoretical predictions for most of the studied systems. In recent years, the use of various spectroscopic methods and *ab initio* calculations has yielded new results on a series of neurotransmitters, such as phenethylamine (PEA) [126, 180, 280–282, 287] and its hydrated clusters [288], 2-phenylethanol [126, 282, 287], phenylalanine [129], etc. Ephedrines comprise an interesting class of neurotransmitters. Simons and co-workers have explored ephedrine [127, 286], norephedrine [285], and pseudoephedrine [127], and their hydrated clusters [128] using mass-selected R2PI spectroscopy with conventional resolution, UV hole-burning, and IR ion-dip spectroscopy coupled with *ab initio* calculations. The authors have identified four conformational structures from the theoretical calculations and assigned them to the peaks observed in the vibrationally resolved R2PI spectrum.

This work presents new results on the mass-selected R2PI low- and the first high-resolution UV spectra of the ephedrine ($C_{10}H_{15}NO$) monomer. The low-resolution spectrum simultaneously recorded at two mass channels (parent (m/z = 165) and fragment (m/z = 58)) allows for classication of the bands with respect to their fragmentation ratio. In this way, the new investigation complements the existing information and provides new experimental data on the identification of the peaks. Furthermore, it provides the first high-resolution spectrum of the strongest band of the EPD monomer. On the basis of this spectrum with the help of computer assisted fitting algorithm, very accurate values of the rotational constants for the ground, S_0, and the first excited, S_1, electronic state, and reliable values of the transition moment ratios have been determined, which

provides a critical test for the theoretically predicted structures.

11.2 Experiment and Data Processing

The low-resolution spectra of EPD as well as its high-resolution spectrum were measured by R2PI with mass selectivity in a supersonic molecular beam. The experimental set up has been described in detail in Sec. 6.2. The species was heated up to 110° to produce it in a sufficient concentration in the molecular beam. Ar was used as a carrier gas at a stagnation pressure of 3 bar. The diameter of the used nozzle orifice was 300 μm.
The analysis of the highly resolved spectrum of the the EPD monomer was performed with the computer-assisted fitting routine based on genetic algorithms, described in detail in Sec. 6.3. The best-fit spectrum of the EPD monomer was produced after a fit using 650 iterations with 250 individuals. The achieved cross correlation is 96%.

11.3 Results and Discussion

11.3.1 Low Resolution Spectra

First, low-resolution ($\Delta\nu$ *ca*. 0.4 cm^{-1}) R2PI experiments with mass selectivity have been carried out to investigate the vibrational structure of the $S_1 \longleftarrow S_0$ spectrum of the EPD monomer. They reveal that the EPD monomer undergoes an efficient fragmentation upon ionization even in the case of a two-colour experiment. The resulting fragmentation has the mass of the side chain [$CH(CH_3)NHCH_2$] containing the amino group (m/z = 58). Such kind of fragmentation seems to contradict the general rule that the charge is located in the larger fragment with the lower ionization energy, yet however, it is typical for molecular systems containing methylmethyl group and amino groups in their side chains, since the presence of these groups leads to a stabilization of the side-chain cation [127, 303].

Ionization Energy

The initial explanation of the fragmentation behaviour of the EPD monomer was that the fragmentation occured in the cation, resulting from very high excess energy because the ionizsing photon in the R2PI led to a total excitation energy above the dissociation limit in the ionic state. This is likely the case in one-colour experiments, where the energy of the second photon is large and fixed [127]. To test this assumption, R2PI two-colour experiments with different smaller

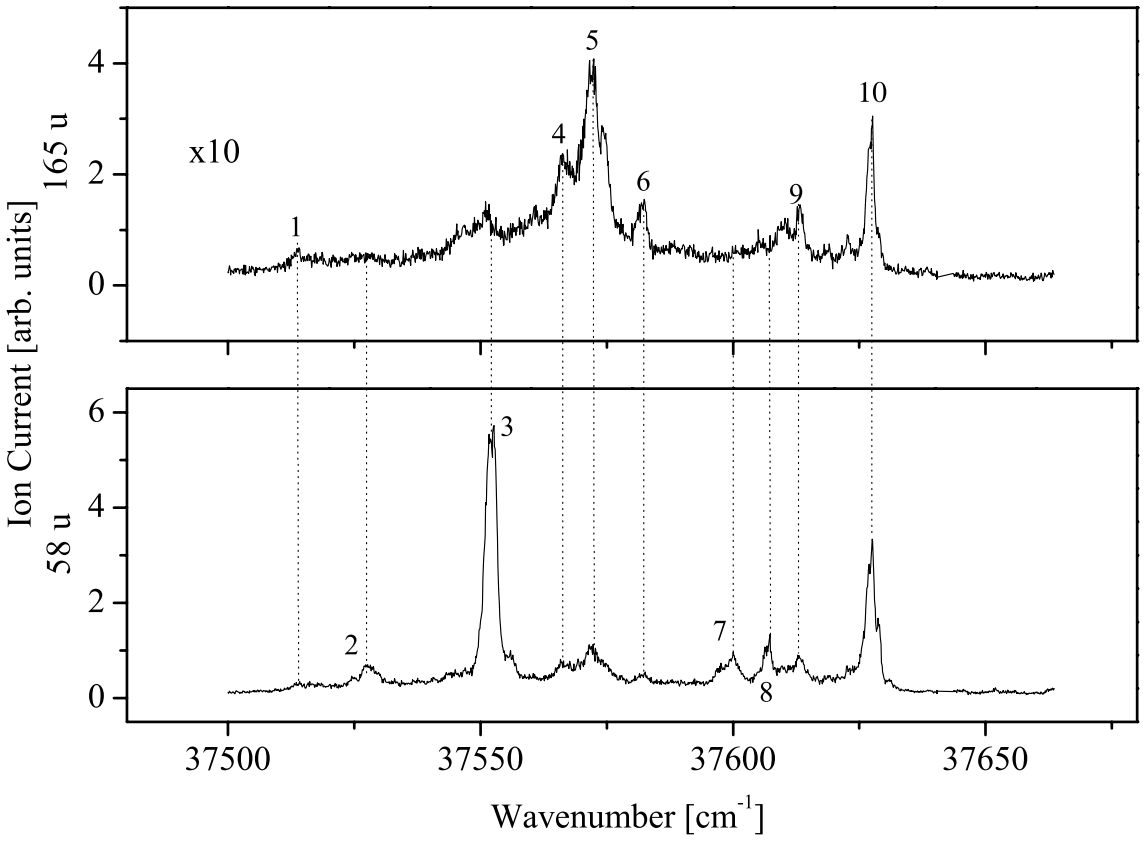

Figure 11.1: *Low-resolution one-colour R2PI spectra of ephedrine (EPD) measured at the parent (m/z165) (upper trace) and fragment (m/z=58)(lower trace) mass channels, respectively. Corresponding peaks are designated by vertical dashed lines.*

energies of the second photon were performed whereas the energy of the excitation photon was fixed to that of the strongest peak, 3, in the $S_1 \longleftarrow S_0$ spectrum (Fig. 11.1, lower trace). The energy of the second photon was decreased stepwise to the lowest possible limit (32260 cm^{-1}) so that ion signal still could be observed. This gives an upper limit of the ionization energy of 69812 cm^{-1} (8.3 eV). For all energies of the second photon, even for the lowest one, however, the fragmentation of the ephedrine parent ion could not be avoided. A plausible interpretation of this result in the two-colour experiment is that the absorption coefficient for the second photon around 32300 cm^{-1} in the ground ionic state of ephedrine is much higher than that for the ionizing step from the S_1 state, this leading to the absorption of a further photon within the EPD cation immediately after it has been produced. This ladder switching process has been shown to lead to an efficient fragmentation of the benzene cation [304, 305].

Fragmentation Behaviour

To investigate the fragmentation behaviour in more detail, the low-resolution one-colour R2PI spectra of the EPD monomer were measured simultaneously at the parent (m/z = 165) and fragment (m/z = 58) mass channels, respectively. The resulting spectra are shown in Fig. 11.1 on a different vertical scale. Most of the peaks in the spectrum measured at the parent mass correlate with the results of Simons and co-workers [127, 128]. The spectra feature well-resolved vibronic structure and display several intense vibronic bands, labelled as 1-10 in Fig. 11.1. Corresponding peaks in the two mass channels are indicated by dashed vertical lines. It can be clearly seen that the relative height of most of the corresponding peaks differs in the two spectra. For example, peak 10 has nearly the same height in both spectra while peak 3 is much higher in the fragment (m/z = 58) mass channel (lower trace), and peak 5 is higher in the parent (m/z = 165) mass channel spectrum (upper trace). A closer inspection reveals that the peaks may be subsumed into three groups with respect to their intensity ratio, defined as the quotient of the intensity measured at the fragment (m/z =58) mass channel and that measured at the parent (m/z =165) mass channel for a certain peak. The summarized information on all of the peaks is presented in Table 11.1, where the last column shows the corresponding peaks from Butz et *al*. [128]. Group I contains only peak 3, where the fragmentation ratio is 58. Group II comprises peaks 2, 7, 8, and 10, characterized by a fragmentation ratio between 10 and 17. Group III encompasses peaks 1, 4, 5, 6, and 9 with a ratio of around 3. The different fragmentation ratio indicates different origins of the three groups of bands; i.e., there are overlapping spectra of three different species, e.g., conformers or clusters produced in the molecular beam contributing to the observed mass channels. The measured fragmentation behaviour represents new information for the identification of the nature of the species observed.

The weakest fragmentation is observed for the peaks in group III. One member of this group, peak 5, has been assigned as originating from an EPD·H_2O cluster [128]. This is an evidence for the presence of water in the vacuum chamber even after the attempts to avoid it. The inefficient fragmentation of the EPD cation in this case can be explained by energy considerations. For the dissociation of the EPD·H_2O cation, energy of about 0.5-1.0 eV [306] is necessary. Thus, the energy released as kinetic energy of the fragments and the internal energy of the water molecule decrease the amount of energy available for the subsequent dissociation of the EPD cation leading to a higher EPD cation signal. As a consequence, a less efficient fragmentation of the EPD cation is indeed observed (Fig. 11.1 and Table 11.1). From their identical fragmentation behaviour, it is inferred that all of the peaks 1, 4, 5, 6, and 9 of group III originate from the EPD·H_2O cluster. The more efficient fragmentation behaviour observed for the peaks in group I and group II brings forward the hypothesis that they come from two distinct EPD conformers. There are four peaks in group II. The efficient fragmentation of the species bringing forth peak 7 has been explained by a special conformer with a weak intramolecular interaction of the benzene ring

Peak	Group	Peak position, cm^{-1}	Ratio, 58/165	Assignment[a]
1	II	37514.1	4.6	···
2	II	37527.6	12	···
3	I	37552.7	59	*A*
4	III	37566.3	3.4	···
5	III	37572.4	2.8	*B*
6	III	37582.4	3.6	*C*
7	II	37600.0	16	*X*
8	II	37607.3	15	*D*
9	III	37613.0	6.2	···
10	II	37627.5	11	*E*

[a]Taken from Refs. [128, 285]

Table 11.1: *Classification of the observed vibrational bands in the low-resolution one-colour two-photon R2PI spectrum of the EPD monomer of Fig. 11.1*

with the side chain ($CH(CH_3)NHCH_3$, m/z = 58) [127]. This peak has been attributed to an *anti-gauche* conformational structure [127]. Thus, it is reasonable to propose that also the other peaks, 2, 8, and 10 of group II originate from the same conformer. Peak 3 from group I has the most pronounced fragmentation behaviour but there is no other prominent (detectable) peak of this category observed in the spectrum. This peak has been assigned by Butz et *al*. to another *anti-gauche* conformer on the basis of a band contour analysis. As a further step in the study of the conformational structure of ephedrine, in the next section, the high-resolution spectrum of this band is presented to complement the existing results with precise information and to check the assignment.

11.3.2 High Resolution Spectrum

The experimental high-resolution UV spectrum of the EPD monomer is depicted in Fig. 11.2 (upper trace). It unveils the rovibronic structure of peak 3 in Fig. 11.1 at 37552.116(1) cm^{-1}. The spectrum was measured at the side-chain ($CH(CH_3)NHCH_3$, m/z = 58) fragment mass channel only since due to the efficient fragmentation upon ionization the signal intensity at the parent mass channel is too weak, which hinders the attainment of a satisfactory signal-to-noise ratio. The rotational temperature has been found to be 8 *K*, which is relatively high and is, most probably, due to nonoptimized cooling conditions. The band is characterized by prominent P and R branches in the wings and a small contribution from the Q branch in the centre. The central dip is not pronounced due to a relatively strong *a* type feature present in the spectrum. The spectrum is classified as *a* and *b* hybrid type [94]. The spectrum does not exhibit single rotational lines

but regularly spaced peaks with FWHM of about 300 MHz formed by aggregation of rotational lines. The rotational constants and the transition moment ratio for the ephedrine monomer have been found by using the computer-assisted routine described in Sec. 6.3. The fitting procedure was initiated with arbitrary starting values of the rotational constants. The resulting best-fit theoretical spectrum is also shown in Fig. 11.2 (lower inverted trace). It was obtained by convoluting the theoretical stick spectrum with a Gaussian line with FWHM of 120 MHz. There is a very good agreement in the peak positions (see Fig. 11.2, inset). The slight mismatch in the peak intensity between the experimental and the simulated spectra is, probably, due to saturation of the induced transitions. Saturation rather than a fast dynamics is assumed also to be responsible for the frequency width of 120 MHz needed for the convolution of the calculated stick spectrum to acquire agreement with the peak width in the experimental spectrum. This width is larger than the frequency width of the exciting laser of *ca*. 100 MHz. The difference in the total intensity in the left side of the experimental and theoretical spectra is tentatively ascribed to a drop of the laser power in the end of the experiment. The obtained values of the rotational constants for the ground and excited state, respectively, and the transition moment ratio, are summarized in Table 11.2. There is a surprisingly good agreement within less than 1% between the values of the rotational constants for the ground, S_0, and the first excited, S_1, electronic states, respectively, obtained from the fitting of our high-resolution spectrum and those calculated by Butz et *al*. [127]. The experimental rotational constants for the ground and the first excited electronic state differ by only 1.5%, which manifests that the investigated conformer is a relatively stable system and it does not experience substantial structural changes when electronically excited. This could be interpreted as a result of the hydrogen bonds that are supposed to stabilize this conformational structure [127, 303]. The fitted transition moment ratio is $\mu_a^2 : \mu_b^2 : \mu_c^2 = 35{:}65{:}0$. This result complies with the hybrid type of the spectrum discussed above. The absence of a *c* type contribution is a plausible and an expected feature having in mind that most of the mass of the molecule is in the plane of the phenyl ring, where the *a* and *b* principal axes of inertia lie. The transition moment ratio found on the basis of the fitting of the high-resolution spectrum disagrees with the result obtained from *ab initio* calculations [127], which is 62:34:4. This is a striking result in view of the good agreement of the experimental and the theoretically predicted rotational constants and demonstrates the problem associated with the calculation of the excited state parameters, in particular charge distributions.

11.4 Summary and Conclusions

Both low- (0.4 cm^{-1}) and high-resolution (0.003 cm^{-1}) resonantly enhanced two-photon ionization spectroscopy studies with mass selection on the EPD monomer have been conducted. The molecule is characterized by an effective fragmentation when ionized, leading to the side-

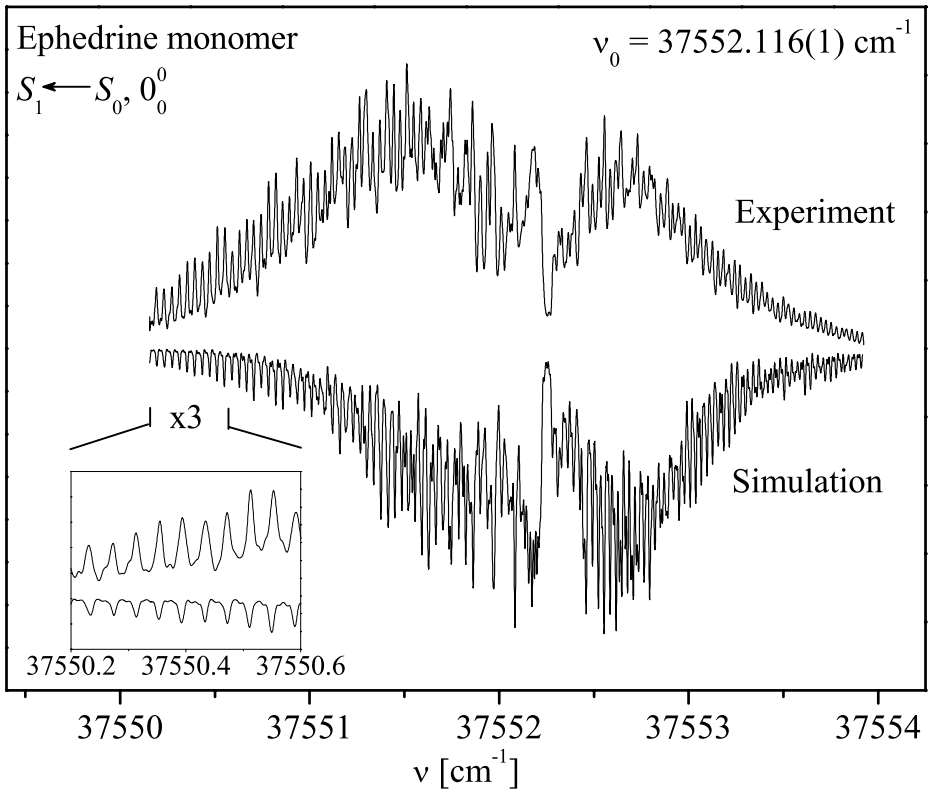

Figure 11.2: *Highly resolved spectrum of peak* 3 *in Fig. 11.1 of EPD at* ν_0*=37552.116(1)* cm^{-1} *recorded at the fragment (m/z=58) mass channel. Upper trace: experimental spectrum. Lower inverted trace: the best-fit simulated spectrum based on the parameters listed in Table 11.2. Inset: magnified part of the spectrum.*

	Ground state S_0		Excited state S_1	
Rotational constant	GHz	cm^{-1}	GHz	cm^{-1}
A	1.9966(42)	0.06660(14)	1.9639(51)	0.06551(17)
B	0.5303(33)	0.01769(11)	0.5231(27)	0.01745(9)
C	0.4941(60)	0.01648(20)	0.4929(48)	0.01644(16)
Transition moment ratio				
$\mu_a^2 : \mu_b^2 : \mu_c^2$	35:65:0			
Origin ν_0, cm^{-1}	37552.116(1)			

Uncertainty of the last significant figure(s) is given in parentheses.

Table 11.2: *Experimental rotational constants of the EPD monomer conformer giving rise to peak* 3 *in Fig. 11.2. The rotational constants and the transition moment ratio have been obtained through computer-aided fit of the highly resolved spectrum (Fig. 11.2) of this conformer.*

chain (($CH(CH_3)NHCH_3$, $m/z = 58$)) cation containing the amino group. In the measured range between 37500 and 37650 cm^{-1} of the low-resolution spectrum 10 peaks have been identified. They are subsumed into three groups showing different fragmentation behaviour. On the basis of the fragmentation ratios, the peaks are suggested to originate, either from dissociation of the EPD·H_2O clusters or from two distinct conformational structures. This demonstrates that not only the difference in the ionization energies but also the different fragmentation efficiency of the ionic conformers can provide an important information on distinguishing conformational structures. The high-resolution spectrum has yielded accurate information on the values of the rotational constants of the EPD monomer for the ground, S_0, and the first excited, S_1, state, respectively. The found values of the rotational constants are in surprisingly good agreement with those obtained from *ab initio* calculations by Simons and co-workers [127]. On the other hand, the transition moment ratio found from the fitting of the presented in this work high-resolution spectrum, departs significantly from that of Ref. [127]. From this, one can conclude that *ab initio* calculations with the present level of precision alone are not sufficient to yield undeniable data on the conformational preferences of biological molecules and, in particular, their transition moment ratio, which is determined by their conformational structure. This brings forward the necessity of high-resolution spectroscopic data for reliable assignment of the structural and transition moment parameters of complicated molecular structures such as ephedrine and other sneurotransmitters.

Part IV

Concluding Remarks

Summary and Conclusions

Molecular interactions and the concept of molecular bonds are the underlying fundament for the understanding of the properties and functionality of chemical and biological systems. Whilst chemical interactions are well-studied, weak molecular interactions have not been complteley elucidated yet. It has been realized, however, that weak molecular interactions and the subtle balance between them are responsible for the conformational stabilization of flexible molecules and play a key role in solavation processes, which are ubiquitous in the living nature. Thus, the profound knowledge on weak interactions is an indispensable prerequisite for the proper description and prediction of molecular shapes and behaviour. The most fruitful approach to getting an insight into weak molecular interactions is the co-operation between high-level theory and experimental spectroscopic investigations of isolated molecular systems in a mutually complementary fashion. Towards this end, the present work describes new results on model molecular systems, including flexible molecules and weakly bound molecular complexes obtained for the first time through the promising combination of high-resolution resonance-enhanced two-photon ionization spectroscopy with mass selectivity, genetic-algorithm-based rotational fitting technique, and high-level *ab initio* quantum chemistry calculations. These results shed light on some particular aspects of weak interactions and their consequences on the molecular shape and binding pattern.
As a first step, a general survey of the theoretical fundamentals has been presented. The types of molecular interactions have been briefly discussed and classified. The concept of weak molecular bonds has been introduced and the distinction between weak molecular interactions and weak molecular bonds has been emphasized. The types of weak chemical bonds have been given along with a discussion on their most typical occurrences.
The practical application of the theories describing weak interactions is realized through quantum-chemistry calculations, which are an important tool for simulation and prediction of molecular structures and properties, and have gained significance in the interpretation and disambiguation of experimentl data. That is why, an overview of the most commonly used theoretical methods along with the most popular commercially available programmes for *ab initio* calculations has been given.
To bridge the gap between the abstract description of molecular interactions and observables obtained from spectroscopy, the interaction between light and matter has been considered within

the framework of the semiclassical model. The Born-Oppenheimer approximation has been elucidated and its use has been argumented. The important concept of the rigid rotor, and the associated with it molecular energy levels, transition moment vector, transition selection rules, and transition intensities have been described.

Spectroscopy provides a nondemolishing and gentle means for probing of various molecular characteristics. That is why, it is most often the method of choice for the investigation of molecular species. Nowadays, there exists an enormous variety of spectroscopic techniques. The most advanced of them which are relevent to the topic discussed in this work have been presented.

The resonance-enhanced two-photon ionization laser spectroscopy with mass selectivity has been employed to obtain the results presented in this work. This technique has been thoroughly described along with the details of the experimental set up in our laboratory. Particular emphasis has been put on the production of supersonic molecular beams, the laser system and the automated control of the laser experiment, and the genetic- algorithm- based fitting routine. The latter has been developed in our group. It has been rendered a due consideration in this work since this advanced fitting routine of molecular specrtra with partial rotational resolution provides accurate values for the rotational constants and the transition moment ratio of the studied species and hence reliable implications on the structure of those species can be inferred.

The presented results can be divided into two main groups. The first one considers the properties and behaviour of aromatic molecules that pertain a double covalent bond in their side chain, and various types of complexes with those molecules. The second group of results encompasses the investigation of flexible molecules, including 2-phenylethanol and the neurotransmitter molecule, ephedrine.

Several important types of weak interactions and the interplay between them have been elucidated through the investigation of styrene and its comolexes with acetylene and argon, and the *para* fluorinated styrene and its singly hydrated complex.

It has been confirmed by high-resolution experiments and rotational fit based on genetic algorithms that the conjugation between the π-electron systems, the one of the benzene ring and the one of the vinyl group, in bare styrene yileds a planar structure for both ground and the first excited electronic state.

The nonconventional C-H$\cdots\pi$- type hydrogen bond has been addressd through the investigation of the weakly bound complex between styrene and acetylene, the latter being also a molecule with a π-electron system. It has been found that the preferred geometry of the complex is the one in which acetylene binds to the benzene ring of styrene as a proton donor, which brings the implication that notwithstanding the π-electron delocalization in styrene, the proton affinity of the aromatic ring is still high enough to favour the formation of a weak hydrogen bond and thus the aromatic ring remains the preferred binding site. The structure in which the acetylene moiety is a proton acceptor from the aromatic ring of styrene is less favoured. No evidences for an interaction between the π electrons of acetylene and those of the vinyl group of styrene have been found. The reduced electron density symmetry of the benzene ring in styrene results in a tilting

of the acetylene moiety relative to the C_6 symmetry axis of the aromatic ring. The formation of a weak C-H$\cdots\pi$ bond does not bring about an observable change of the transition moment vector of the chromophore, as it has been demonstrated for the complex between styrene and acetylene. The effect of the electron conjugation on the van der Waals bond has been studied through the model complex bewteen styrene and argon. It has been shown that the binding pattern in this case is very similar to the one in the complex between benzene and argon. The distance between the argon atom and the aromatic ring in the case of the styrene-argon complex is shorter compared to the one in the benzene-argon complex. This implies that the electron conjugation in this case leads to a strengthtening of the van der Waals bond.

The formation of van der Waals complexes provides a convenient means for testing the planarity of the host molecule through a detection of spectral splittings in the resonance enhanced two-photon ionization spectrum of the complex. The lack of a splitting of the origin band of the styrene-argon complex even under high-resolution conditions has served as an additional eveidence for the planarity of styrene.

The competition between the mesomeric and the electron attraction effects and their influence on the formation of hydrated complexes and their binding motifs have been explored by studying the singly hydrated complex of the *para* fluorinated styrene. Due to the subtle interplay between the electron attraction of the electronegative fluorine atom and the releasing mesomeric effect of the vinyl group, both σ and π hydrogen bonding of water to fluorostyrene are feasible. It has been found, however, that in this case water binds to styrene through the formation of two σ hydrogen bonds: one to the fluorine atom, in which water is the proton donor, and a second one between the water oxygen atom and a hydrogen atom from the benzene ring of styrene, a pattern drastically different from the π bonding in the benzene-water complex.

The importance of the intramolecular hydrogen bonds for the conformational stabilization of flexible molecules has been highlighted through the investigation of the 2-phenylethanol monomer. It has been demonstrated through high-resolution resonance enhanced two-photon ionization spectroscopy combined with rotational fit based on genetic algorithms and quantum chemistry calculations that the most abundant in the cold beam, *gauche*, structure is stabilized by an intramolecular nonconventional hydrogen bond between the OH group of the bent side chain and the π electrons of the aromatic ring.

The concurrence of intramolecular hydrogen bonds and van der Waals interactions has been elucidated through the ivestigation of the complex between 2-phenylethanol and argon. It has been found that in the most abundant configuration, the argon atom binds to the aromatic ring of 2-phenylethanol on the side of the side chain, giving rise to the *cis* conformation of the cluster. The less favoured, *trans*, geometry, in which the argon atom binds to the opposite side of the benzene ring, has also been detected in the molecular beam. A tentative conclusion on the existence of a weak ”hydrogen bond”- type interaction between the side-chain OH group and the argon atom has been drawn to explain the additional stabilization of the *cis* geometry.

For the first time, a bilogically active molecule has been studied by resonance enhanced two-

photon ionization high resolution spectroscopy with mass selectivity. The experiments on ephedrine have shown that the molecule undergoes a very efficient fragmentation upon ionization. The classification of the observed bands according to their fragmentation efficiency have led to the idea of conformer- or state-selective fragmentation. The structure of the most abundant conformation of the ephedrine monomer has been determined on the basis of the high-resolution experimental results and their analysis by a rotational fitting routine employing genetic algorithms. The latter has yielded also an accurate value for the transition moment orientation. The obtained accurate inertial parameters of the ephedrine monomer manifest that even large flexible molecules with many degrees of freedom have well-defined shapes owing to the intramolecular weak hydrogen bonds that stabilize the respective geometries.

The review of the attained results renders confidence that the combination of mass-resolved high-resolution resonance-enhanced two-photon ionization spectroscopy supported by rotational fitting techniques based on genetic algorithms and high-level quantum chemistry calculations provides a powerful but yet gentle approach for the investigation of weak intra- and intermolecular interactions and the subtle interplay between them. The so-obtained results bring important implications both for the fundamental underastanding of the properties and behaviour of various chemical and biological systems and, on the other hand, provide the basis for some practical applications, such as chemical synthesis, molecular design, material science, pharmacology, etc.

Outlook and Perspectives

This work has demonstrated the potential power of the combination of the highly resolved resonance enhanced two-photon ionization spectroscopy with mass selectivity, rotational fitting routine based on genetic algorithms, and high-level quantum chemistry calculations for the investigation of weak molecular interactions. The presented in this work new results provide an insight into some aspects of weak intra- and intermolecular interactions. To rationalize, however, the properties and phenomena governed by weak interactions, the latter must be investigated in their complexity and interconnection. Towards this end, in addition to the discussed results, some possible advanced studies aiming at getting a broader view on weak interactions are proposed.

To produce molecules with low vapour pressure in the gas phase, laser desorption can be used as an alternative to the heating. To study the dynamics of the first excited electronic state by a resonance enhanced two-photon ionization, a controllable variable delay of the ionization laser pulses with respect to the excitation pulses can be introduced. To increase the spectral resolution and at the same time to retain the mass selectivity, a combination between high-resolution resonance enhanced two-photon ionization and laser induced fluorescence experiments is a promising approach. The idea includes a simultaneous scan of both high-resolution spectra. This technique is expected to be helpful in cases when an efficient fragmentation upon ionization takes place.

A possible upgrade of the existing fitting computer programme based on genetic algorithms is the inclusion of an option allowing for the fit of two or more overlapping spectra. An inclusion of corrections in the molecular Hamiltonian accounting better for the molecular nonrigidity is also beneficial.

The pending molecular systems include molecules with π-electron systems and unsaturated bonds (similar to styrene), flexible molecules containing an electronegative atom at different positions, e.g., fluorinated 2-phenylethanol, to study the effect of the substitution on the conformational preference of the species, and stereoisomers of a certain molecule, e.g. ephedrine, pseudoephedrine, and norephedrine, and their hydrated complexes. The idea behind studying isomers is to explore how the sterical arrangement of molecular groups affects the properties of the respective species. The used approach is promising for providing interesting results even on large systems and hence it can be extended to the study of base pairs and amino acids. The ambition for studying hydrated complexes is targeted at polyhydrated clusters containing more

than two water molecules, which are anticipated to yield information on weak interactions and the resulting conformational shapes and binding patterns.

The ultimate purpose of such experiments is to mimic and investigate the behaviour of biologically active species in an environment close to their natural one and,s in a more general concept, to get an insight into the interesting properties taking place at the borderline between the microscopic and mesoscopic world.

Bibliography

[1] G. N. Lewis, *Valence and the Structure of Atoms and Molecules* (Chemical Catalog, New York, 1923).

[2] J. D. van der Waals, *Doctoral Dissertation* (Universiteit Leiden, Leiden, 1873).

[3] E. G. Robertson and J. P. Simons, Phys. Chem. Chem. Phys. **3**, 1 (2001).

[4] J.-M. Lehn, Angew. Chem. Int. Ed. **27**, 89 (1988).

[5] J.-M. Lehn, Angew. Chem. Int. Ed. **29**, 1304 (1990).

[6] J.-M. Lehn, J. L. Atwood, J. E. D. Davies, D. D. MacNicol, and F. Vögtle, *Comprehensive Supramolecular Chemistry* (Pergamon, Oxford, 1996).

[7] C. Bieniarz, *Technology Encyclopedia Pharmaceutical* (Marcel Dekker, New York, 1999).

[8] W. T. S. Huck, L. J. Prins, R. H. Fokkens, N. M. Nibbering, F. C. J. M. van Veggel, and D. N. Reinhoudt, J. Am. Chem. Soc. **120**, 6240 (1998).

[9] J. W. J. Knapen, A. W. van der Made, J. C. de Vilde, P. W. N. M. van Leeuwen, P. Wijkens, D. M. Grove, and G. van Koten, Nature(London) **372**, 659 (1994).

[10] A. Warshel, A. Papazyan, and P. A. Kollman, Science **269**, 102 (1995).

[11] G. Scoles, *Atomic and molecular beam methods* (Oxford University Press, New York, 1988).

[12] D. H. Levy, Ann. Rev. Phys. Chem. **31**, 197 (1980).

[13] T. S. Zwier, Annu. Rev. Phys. Chem. **47**, 205 (1996).

[14] H. J. Neusser and R. Sussmann, *Structure of weakly bound complexes from electronic spectra, Jet spectroscopy and molecular dynamics* (Chapman and Hall, London, 1994).

[15] D. J. Nesbitt, Chem. Rev. **88**, 843 (1988).

[16] A. W. Castleman Jr and R. G. Keesee, Ann. Rev. Phys. Chem. **37**, 525 (1986).

[17] A. Amirav, U. Even, and J. Jortner, J. Chem. Phys. **75**, 2489 (1981).

[18] E. R. Bernstein, K. Law, and M. Schauer, J. Chem. Phys. **80**, 634 (1984).

[19] J. Bösiger and S. Leutwyler, Phys. Rev. Letters **59**, 1895 (1987).

[20] M. Y. Hahn and R. L. Whetten, Phys. Rev. Lett. **61**, 1190 (1988).

[21] U. Even, N. Ben-Horin, and J. Jortner, Chem. Phys. Lett. **156**, 138 (1989).

[22] W. Demtröder, *Laser spectroscopy* (Springer, Berlin, 1988).

[23] C. A. Haynam, D. V. Brumbaugh, and D. H. Levy, J. Chem. Phys. **80**, 2256 (1984).

[24] W. M. van Herpen and W. L. Meerts, Chem. Phys. Lett. **147**, 7 (1988).

[25] S. Sun and E. R. Bernstein, J. Phys. Chem. **100**, 13348 (1996).

[26] E. R. Bernstein, Ann. Rev. Phys. Chem. **46**, 197 (1995).

[27] P. Hobza, H. L. Selzle, and E. W. Schlag, Chem. Rev. **94**, 1767 (1994).

[28] P. M. Felker, P. M. Maxton, and M. W. Schaeffer, Chem. Rev. **94**, 1787 (1994).

[29] W. Klemperer, Science **257**, 887 (1992).

[30] B. Brutschy, Chem. Rev. **92**, 1567 (1992).

[31] G. C. Maitland, M. Rigby, E. B. Smith, and W. A. Wakeham, *Intermolecular forces*, *The International Series of Monographs on Chemistry*, 2nd ed. (Clarendon Press, Oxford, 1987).

[32] F. London, Z. Phys. **63**, 245 (1930).

[33] W. Heitler and F. London, Z. Physik **44**, 455 (1927).

[34] P. M. Morse, Phys. Rev. **34**, 57 (1929).

[35] J. E. Lennard-Jones, Proc. Phys. Soc. **43**, 461 (1931).

[36] R. M. Helm, *Hochaufgelösende UV-Laserspektroskopie: Struktur und Dynamik nach elektronischer Anregung von wasserstoffbrückengebundenen Aromat-Wasser Komplexen* (Herbert Utz Verlag, München, 1998).

[37] M. J. S. Dewar, Nature(London) **156**, 784 (1945).

[38] E. Carrasquillo, T. S. Zwier, and D. H. Levy, J. Chem. Phys. **83**, 4990 (1985).

[39] M. Nishio, M. Hirota, and Y. Umezawa, *The CH/π Interaction: Evidence, Nature and Consequences* (Wiley-VCH, New York, 1998).

[40] S. Djafari, H.-D. Barth, K. Buchhold, and B. Brutschy, J. Chem. Phys. **107**, 10573 (1997).

[41] A. Fujii, S. Morita, M. Miyazaki, T. Ebata, and N. Mikami, J. Phys. Chem. A **108**, 2652 (2004).

[42] S. Chervenkov, P. Wang, J. E. Braun, T. Chakraborty, and H. J. Neusser, Phys. Chem. Chem. Phys. **9**, 837 (2007).

[43] K. Müller-Dethlefs and P. Hobza, Chem. Rev. **100**, 143 (2000).

[44] E. Reed, Alan, A. Curtiss, Larry, and F. Weinhold, Chem. Rev. **88**, 899 (1988).

[45] P. Hobza and Z. Havlas, Chem. Rev. **100**, 4253 (2000).

[46] P. Hobza, V. Špirko, H. L. Selzle, and E. W. Schlag, J. Phys. Chem. A **102**, 2501 (1998).

[47] P. Hobza, V. Špirko, Z. Havlas, K. Buchhold, B. Reimann, H.-D. Barth, and B. Brutschy, Chem. Phys. Lett. **299**, 180 (1999).

[48] G. N. Patwari, T. Ebata, and N. Mikami, J.Phys.Chem. **105**, 8642 (2001).

[49] J. C. Lee Jr., P. Eduardo, A. L. Rheingold, and R. H. Crabtree, J. Am. Chem. Soc. **116**, 11014 (1994).

[50] Q. Liu and R. Hoffmann, J. Am. Chem. Soc. **117**, 10108 (1995).

[51] W. Kauzmann, Adv. Prot. Chem. **14**, 1 (1959).

[52] D. Chandler, Nature **437**, 640 (2005).

[53] P. Hobza and R. Zahradnik, Chem. Rev. **88**, 871 (1988).

[54] J. L. Calais and E. S. Kryachko, *Conceptual perspectives in quantum chemistry* (Spinger Netherland, Amsterdam, 1997).

[55] A. R. Leach, *Molecular modelling principles and applications* (Addison Wesley, Sussex, 1996).

[56] I. N. Levine, *Quantum Chemistry*, 2nd indian reprint ed. (Pearson Education, Singapore, 2004).

[57] A. S. Davydov, *Quantum Mechanics, Monographs in Natural Philosophy*, 1st ed. (Pergamon Press, Oxford, 1965).

[58] D. R. Hartree, Proc. Cambridge Philos. Soc. **24**, 89 (1928).

[59] C. C. J. Roothaan, Rev. Mod. Phys. **43**, 69 (1951).

[60] S. F. Boys, Proc. Phys. Soc. A **200**, 542 (1950).

[61] R. Poirier, R. Kari, and I. G. Csizmadia, *Handbook of Gaussian Basis Sets*, *Physiscal Sciences Data* (Elsevier, Amsterdam, 1985).

[62] J. B. Foresman, M. Head-Gordon, A. Pople, John, and J. EFrisch, Michael, J. Phys. Chem. **96**, 135 (1992).

[63] J. F. Stanton, J. Gauss, N. Ishikawa, and M. Head-Gordon, J. Chem. Phys. **103**, 4160 (1995).

[64] C. Møller and M. S. Plesset, Phys. Rev. **40**, 618 (1934).

[65] R. J. Bartlett, Ann. Rev. Phys. Chem. **32**, 359 (1981).

[66] P. Hohenberg and W. Kohn, Phys. Rev. **136**, 864 (1964).

[67] W. Kohn and L. J. Sham, Chem. Rev. **140**, 1133 (1965).

[68] C. Lee, W. Yang, and R. G. Parr, Phys. Rev. B **37**, 785 (1988).

[69] E. B. Wilson Jr., J. C. Decius, and P. C. Cross, *Molecular Vibrations* (Dover Publications, New York, 1955).

[70] M. J. Frisch, G. W. Trucks, H. B. Schlegel, G. E. Scuseria, M. A. Robb, J. R. Cheeseman, J. A. Montgomery Jr., T. Vreven, K. N. Kudin, J. C. Burant, J. M. Millam, S. S. Iyengar, J. Tomasi, V. Barone, B. Mennucci, M. Cossi, G. Scalmani, N. Rega, G. A. Petersson, H. Nakatsuji, M. Haga, M. Ehara, K. Toyota, R. Fukuda, J. Hasegawa, M. Ishida, T. Nakajima, Y. Honda, O. Kitao, H. Nakai, M. Klene, X. Li, J. E. Knox, H. P. Hratchian, J. B. Cross, C. Adamo, J. Jaramillo, R. Comperts, R. E. Stratmann, O. Yazyev, A. J. Austin, R. Cammi, C. Pomelli, J. W. Ochterski, P. Y. Ayala, K. Morokuma, J. A. Voth, P. Salvador, J. J. Dannenberg, V. G. Zakrzewski, S. Dapprich, A. D. Daniels, M. C. Strain, O. Farkas, D. K. Malick, A. D. Rabuck, K. Raghavachari, J. B. Foresman, J. V. Ortiz, Q. Cui, A. G. Baboul, S. Clifford, J. Cioslowski, B. B. Stefanov, G. Liu, A. Liashenko, P. Piskorz, I. Kamaromi, R. L. Maetin, D. J. Fox, T. Keith, M. A. Al-Laham, C. Y. Peng, A. Nanayakkara, M. Challacombe, P. M. W. Gill, B. Johnson, W. Chen, M. W. Wong, C. Gonzales, and J. A. Pople, Gaussian 03, Revision B.04, 2003.

[71] H.-J. Werner, P. J. Knowles, R. Lindh, F. R. Manby, and M. Schütz, MOLPRO, version 2006.1, a package of ab initio programs.

[72] R. Ahlrichs, M. Bär, M. Häser, H. Horn, and C. Kölmel, Chem. Phys. Lett. **162**, 165 (1989).

[73] I. N. Levine, *Molecular Spectroscopy*, 1st ed. (Wiley-Interscience, New York, 1975).

[74] S. H. Lin, Y. Fujimura, H. J. Neusser, and E. W. Schlag, *Multiphoton Spectroscopy of Molecules, Quantum Electronics, Principles and Applications* (Academic Press, Orlando, 1984).

[75] E. Fermi, *Nuclear Physics* (Chicago University Press, Chicago, 1950).

[76] M. Born and R. Oppenheimer, Ann. Physik **84**, 457 (1927).

[77] E. Teller, Hand- u. Jahrb. Chem. Phys. **9**, 43 (1934).

[78] G. Herzberg and E. Teller, Z. Phys. Chem. **B21**, 410 (1933).

[79] L. D. Landau and E. M. Lifschitz, *Lehrbuch der theoretischen Physik I, Mechanik* (Akademie-Verlag, Leipzig, 1982).

[80] W. Gordy and R. L. Cook, *Microwave molecular spectra*, Vol. XVIII of *Techniques of Chemistry*, 1st ed. (John Wiley and Sons, New York, 1984).

[81] J. E. Wollrab, *Rotational Spectra and Molecular Structure*, Vol. 13 of *A series of Monographs on Physical Chemistry*, 1st ed. (Academic Press, New York, 1967).

[82] R. N. Zare, *Angular Momentum. Understanding Spatial Aspects in Chemistry and Physics* (Wiley-Interscience, New York, 1988).

[83] H. J. Neusser, *Habilitation: Zwei-Photonen-Spektroskopie an Molekülen in der Gasphase* (Fachbereich für Chemie, Biologie und Geowissenschaften der Technischen Universität München, München, 1977).

[84] H. A. Jahn and E. Teller, Proc. R. Soc. London **A161**, 220 (1937).

[85] J. Kraitchman, Am. J. Phys. **21**, 17 (1953).

[86] C. C. Costain, J. Chem. Phys. **29**, 864 (1958).

[87] R. Sussmann, R. Neuhauser, and H. J. Neusser, Can. J. Phys. **72**, 1179 (1994).

[88] T. M. Korter, J. Küpper, and D. W. Pratt, J. Chem. Phys. **111**, 3946 (1999).

[89] K. Siglow and H. J. Neusser, Chem. Phys. Lett. **343**, 475 (2001).

[90] G. Herzberg, *Molecular Spectra and Molecular Structure, I. Spectra of Diatomic Molecules* (Van Nostrand, New York, 1950), Vol. I.

[91] G. Herzberg, *Molecular Spectra and Molecular Structure, II. Infrared and Raman Spectra of Polyatomic Molecules* (Krieger, Malabar, 1991), Vol. II.

[92] G. Herzberg, *Molecular spectra and molecular structure, III. Electronic spectra and electronic structure of polyatomic molecules* (Krieger Publishing Company, Malabar, 1991), Vol. III.

[93] K. H. Hellwege, *Einführung in die Physik der Molekeln* (Springer, Berlin, 1990).

[94] J. M. Hollas, *Modern spectroscopy* (Wiley, New York, 1992).

[95] H. Haken and H. C. Wolf, *Molekülphysik und Quantumchemie. Einführung in die experimentellen und theoretischen Grundlagen* (Springer, Berlin, 2006).

[96] S. Svanberg, *Atomic and Molecular Spectroscopy: Basic Aspects and Practical Applications, Springer Series on Atomic, Optical, and Plasma Physics*, 3rd ed. (Springer, Berlin, 2004).

[97] R. E. Smalley, B. L. Ramakrishna, and D. H. Levy, J. Chem. Phys. **61**, 4363 (1974).

[98] R. E. Smalley, J. A. Blazy, P. S. H. Fitch, M. S. Kim, L. Wharton, and D. H. Levy, Opt. Comm. **18**, 59 (1976).

[99] R. E. Smalley, L. Wharton, D. H. Levy, and D. W. Chandler, J. Mol. Spectrosc. **66**, 375 (1977).

[100] D. H. Levy, L. Wharton, and R. E. Smalley, *Laser Spectroscopy in Supersonic Free Jets, Chemical and Biochemical Applications of Lasers* (Academic, New York, 1977), pp. 1–42.

[101] D. H. Levy, Ann. Rev. Phys. Chem. **31**, 197 (1980).

[102] N. F. Ramsey, *Molecular Beams* (Oxford University Press, New York, 1985).

[103] M. Clara, K. Siglow, and H. J. Neusser, Z. Phys. Chem. **214**, 493 (2000).

[104] E. Whittle, D. A. Dows, and G. C. Pimentel, J. Chem. Phys. **22**, 1943 (1954).

[105] I. R. Dunkin, *Matrix Isolation Techniques: A practical Approach, Practical Approach in Chemistry* (Oxfor University Press, London, 1998).

[106] I. D. Reva, A. M. Plokhotnichenko, S. G. Stepanian, A. Y. Ivanov, E. D. Radchenko, G. G. Sheina, and Y. P. Blagoi, Chem. Phys. Lett. **232**, 141 (1995).

[107] P. J. Toennies and A. F. Vilesov, Ann. Rev. Phys. Chem. **49**, 1 (1998).

[108] J. A. Northby, J. Chem. Phys. **115**, 10065 (2001).

[109] C. Callegari, K. K. Lehmann, R. Schmied, and G. Scoles, J. Chem. Phys. **115**, 10090 (2001).

[110] J. P. Toennies and A. F. Vilesov, Angew. Chem. Int. Ed. **43**, 2622 (2004).

[111] K. K. Lehmann and G. Scoles, Science **279**, 2065 (1998).

[112] A. Lindinger, P. J. Toennies, and A. F. Vilesov, J. Chem. Phys. **110**, 1429 (1999).

[113] M. C. Heaven, Annu. Rev. Phys. Chem. **43**, 283 (1992).

[114] D. J. Nesbitt, Annu. Rev. Phys. Chem. **45**, 367 (1994).

[115] S. Goyal, D. L. Schutt, and G. Scoles, Acc. Chem. Res. **26**, 123 (1993).

[116] R. C. Cohen and R. J. Saykally, Annu. Rev. Phys. Chem. **42**, 369 (1991).

[117] J. M. Hutson, Annu. Rev. Phys. Chem. **41**, 123 (1990).

[118] K. R. Leopold, G. T. Fraser, S. E. Novick, and W. Klemperer, Chem. Rev. **94**, 1807 (1994).

[119] P. M. Felker, J. Phys. Chem. **96**, 7844 (1992).

[120] R. Ferraro, John and K. Nakamoto, *Introductory Raman Spectroscopy*, 1st ed. (Academic Press, Boston, 1994).

[121] J. S. Baskin, P. M. Felker, and A. H. Zewail, J. Chem. Phys. **84**, 4708 (1986).

[122] M. R. Topp, Int. Rev. Phys. Chem. **12**, 149 (1993).

[123] I. Hargittai and M. Hargittai, *Stereochemical Applicationd of Gas-Phase Electron Diffraction*, Vol. I of *Methods in Stereochemical Analysis* (Wiley-VCH, Weinheim, 1988).

[124] K. Müller-Dethlefs, O. Dopfer, and T. G. Wright, Chem. Rev. **94**, 1845 (1994).

[125] L. Zhu and P. M. Johnson, J. Chem. Phys. **94**, 5769 (1991).

[126] J. A. Dickinson, M. R. Hockridge, R. T. Kroemer, E. G. Robertson, J. P. Simons, J. McCombie, and M. Walker, J. Am. Chem. Soc. **120**, 2622 (1998).

[127] P. Butz, R. T. Kroemer, N. A. Macleod, and J. P. Simons, J.Phys.Chem. **105**, 544 (2001).

[128] P. Butz, R. T. Kroemer, N. A. Macleod, and J. P. Simons, Phys. Chem. Chem. Phys. **4**, 3566 (2002).

[129] Y. Lee, J. Jung, B. Kim, P. Butz, L. C. Snoek, R. T. Kroemer, and J. P. Simons, J. Phys.Chem. A **108**, 69 (2004).

[130] D. W. Pratt, Annu. Rev. Phys. Chem. **49**, 481 (1998).

[131] J. T. Yi, E. G. Robertson, and D. W. Pratt, Phys. Chem. Chem. Phys. **4**, 5244 (2002).

[132] J. R. Roscioli, D. W. Pratt, Z. Smedarchina, W. Siebrand, and A. Fernandez-Rámoz, J. Chem. Phys. **120**, 11351 (2004).

[133] C. Kang, D. W. Pratt, and M. Schäfer, J. Phys. Chem. A **109**, 767 (2005).

[134] J. T. Yi, J. W. Ribblett, and D. W. Pratt, J. Phys. Chem. A **109**, 9456 (2005).

[135] J. T. Yi, L. Alvarez-Valtierra, and D. W. Pratt, J. Chem. Phys. **124**, 244302 (2006).

[136] T. V. Nguyen, J. T. Yi, and D. W. Pratt, Phys. Chem. Chem. Phys. **8**, 1049 (2006).

[137] G. Berden, J. v. Rooy, W. L. Meerts, and K. A. Zachariasse, Chem. Phys. Lett. **278**, 373 (1997).

[138] K. Remmers, E. Jalviste, I. Mistrik, G. Berden, and W. L. Meerts, J. Chem. Phys. **108**, 8436 (1998).

[139] J. A. Hageman, R. Wehrens, R. de Gelder, W. L. Meerts, and L. M. C. Buydens, J. Chem. Phys. **113**, 7955 (2000).

[140] M. Schmitt, C. Ratzer, and W. L. Meerts, J. Chem. Phys. **120**, 2752 (2004).

[141] G. Myszkiewicz, W. L. Meerts, C. Ratzer, and M. Schmitt, Phys. Chem. Chem. Phys. **7**, 2142 (2005).

[142] R. Neuhauser, *Hochauflösende kohärente und inkohärente Laserspektroskopie an Molekülen und van der Waals Komplexen: Schwingungszustände im elektronischen Grundzustand und hohe Rydbergzustände nahe der Ionisationsschwelle (n¿100)* (Herbert Utz Verlag, München, 1997).

[143] K. Siglow, *Dissertation* (Fachbereich für Chemie der Technischen Universität München, München, 2000).

[144] R. Neuhauser and H. J. Neusser, Chem. Phys. Lett. **253**, 151 (1996).

[145] R. G. Neuhauser, K. Siglow, and H. J. Neusser, J. Chem. Phys. **106**, 896 (1997).

[146] K. Siglow and H. J. Neusser, J. Electron Spectrosc. Relat. Phenom. **112**, 199 (2000).

[147] K. Müller-Dethlefs, M. Sander, and E. W. Schlag, Chem. Phys. Lett. **112**, 291 (1984).

[148] K. Müller-Dethlefs, M. Sander, and E. W. Schlag, Z. Naturforsch. **39a**, 1089 (1984).

[149] W. A. Chupka, J. Phys. Chem. **103**, 8169 (1999).

[150] K. Suzuki, Y. Emura, S. i. Ishiuchi, and M. Fujii, J. Electron Spectrosc. Relat. Phenom. **108**, 13 (2000).

[151] U. Aigner, L. Y. Baranov, H. L. Selzle, and E. W. Schlag, J. Electron Spectrosc. Relat. Phenom. **112**, 175 (2000).

[152] P. M. Johnson and L. Zhu, Int. J. Mass Spectrom. Ion Proc. **131**, 193 (1994).

[153] J. Braun, H. J. Neusser, and P. Hobza, J. Phys. Chem. A **107**, 3918 (2003).

[154] S. Georgiev, T. Chakraborty, and H. J. Neusser, J. Phys. Chem. A **108**, 3304 (2004).

[155] S. Georgiev and H. J. Neusser, Chem. Phys. Lett. **389**, 24 (2004).

[156] S. Georgiev and H. J. Neusser, J. Electron Spectrosc. and Relat. Phenom. **142**, 207 (2005).

[157] N. Kohles, R. Dohlus, H. Graener, and A. Laubereau, *New Results on Vibrational Dynamics in Liquids Using IR Double Resonance Spectroscopy and Other Techniques, in "Ultrafast Phenomena in Spectroscopy", eds. Z. Rudzikas, A. Piskarskas, and R. Baltramiejunas* (World Scientific, Singapore, 1988).

[158] R. J. Lipert and S. D. Colson, J. Phys. Chem. **93**, 3894 (1989).

[159] R. J. Lippert and S. D. Colson, Chem. Phys. Lett. **161**, 303 (1989).

[160] M. Mons, E. G. Robertson, L. C. Snoek, and J. P. Simons, Chem. Phys. Lett. **310**, 423 (1999).

[161] E. Nir, C. Janzen, P. Imhof, K. Kleinermanns, and M. S. de Vries, J. Chem. Phys. **115**, 4604 (2001).

[162] K. Remmers, W. L. Meerts, A. Zehnacker-Rentien, K. LeBarbu, and F. Lahmani, J. Chem. Phys. **112**, 6237 (2000).

[163] R. H. Page, Y. R. Shen, and Y. T. Lee, J. Chem. Phys. **88**, 4621 (1988).

[164] R. H. Page, Y. R. Shen, and Y. T. Lee, J. Chem. Phys. **88**, 5362 (1988).

[165] T. Ebata, A. Fujii, and N. Mikami, Int. Rev. Phys. Chem. **17**, 205 (1998).

[166] R. Neuhauser, K. Siglow, and H. J. Neusser, Phys. Rev. Lett. **80**, 5089 (1998).

[167] C. J. Gruenloh, J. R. Carnery, F. Hagemeister, C. A. Arrington, T. S. Zwier, S. Y. Fredericks, J. T. Wood, and K. D. Jordan, J. Chem. Phys. **109**, 6601 (1998).

[168] T. Ebata, A. Fujii, and N. Mikami, Int. Rev. Phys. Chem. **17**, 331 (1998).

[169] S. I. Ishiuchi, H. Shitomi, K. Takazawa, and M. Fujii, Chem. Phys. Lett. **283**, 243 (1998).

[170] A. Mitsuzuka, A. Fujii, T. Ebata, and N. Mikami, J. Chem. Phys. **105**, 2618 (1996).

[171] D. T. Anderson, S. Davis, and D. Nesbitt, J. Chem. Phys. **105**, 4488 (1996).

[172] D. T. Anderson, M. Schuder, and D. Nesbitt, J. Chem. Phys. **239**, 253 (1998).

[173] D. A. G. Deacon and A. O'Keefe, Rev. Sci. Instrum. **59**, 2544 (1988).

[174] J. J. Scherrer, J. B. Paul, A. O'Keefe, and R. J. Saykally, Chem. Rev. **97**, 25 (1997).

[175] J. B. Paul, R. A. Provencal, C. Chapo, K. Roth, R. Casaes, and R. J. Saykally, J. Phys. Chem. A **103**, 2972 (1999).

[176] M. Araki, T. Motylewski, P. Kolek, and J. P. Maier, Phys. Chem. Chem. Phys. **7**, 2138 (2005).

[177] K. Liu, R. P. Fellers, M. R. Viant, R. P. McLaughlin, M. G. Brown, and R. J. Saykally, Rev. Sci. Instrum. **67**, 410 (1996).

[178] G. Winnewisser, B. S. Dumesh, I. Pak, L. A. Surin, F. Lewen, D. A. Roth, and F. S. Rusin, J. Mol. Spectrosc. **192**, 243 (1998).

[179] R. D. Suenram and F. J. Lovas, J. Mol. Spectrosc. **72**, 372 (1978).

[180] P. D. Godfrey, R. D. Brown, and L. D. Hatherley, J. Am. Chem. Soc. **117**, 8204 (1995).

[181] H. J. Krautwald, L. Schnieder, and K. H. Welge, Faraday. Discuss. **82**, 1 (1986).

[182] R. D. Suenram, G. T. Fraser, and F. J. Lovas, J. Chem. Phys. **89**, 6141 (1988).

[183] M. Canagaratna, J. A. Phillips, M. E. Ott, and K. R. Leopold, J. Phys. Chem. **102**, 1489 (1998).

[184] C. Riehn, A. Weichert, U. Lommatzsch, M. Zimmermann, and B. Brutschy, J.Chem.Phys. **112**, 3650 (2000).

[185] L. Schafer, I. S. Bin Drees, R. F. Frey, C. van Alsenoy, and J. D. Ewbank, J. Mol. Struct. (Theochem) **338**, 71 (1995).

[186] M. Knerich, *Diplomarbeit* (Fachbereich für Chemie, Biologie und Geowissenschaften der Technischen Universität München, München, 1990).

[187] T. Weber, *DissertationFachbereich für Chemie, Biologie und Geowissenschaften der Technischen Uneversität München* (Fachbereich für Chemie, Biologie und Geowissenschaften der Technischen Uneversität München, München, 1991).

[188] W. C. Wiley and I. H. McLaren, Rev. Sci. Instr. **26**, 1150 (1955).

[189] R. Wallenstein and T. W. Hänsch, Opt. Comm. **14**, 353 (1975).

[190] R. Wallenstein and T. W. Hänsch, Phys. Rev. A **22**, 192 (1980).

[191] M. M. Salour, Opt. Commun. **22**, 202 (1977).

[192] E. Riedle, R. Moder, and H. J. Neusser, Opt. Commun. **43**, 388 (1982).

[193] A. E. Siegman, *Lasers*, 1 ed. (University Science Books, Mill Valley, CA, 1986).

[194] R. Neuhauser, *Diplomarbeit: Kohärente Hochauflösende Ionendip Spektroskopie* (Fachbereich für Chemie, Biologie und Geowissenschaften der Technischen Universität München, München, 1993).

[195] U. Schubert, *Dissertation* (Institut für Chemie, Biologie und Geowissenschaften der Technischen Universität München, München, 1988).

[196] W. H. Press, S. A. Teukolsky, W. T. Vetterling, and B. P. Flannery, *Numerical recipes in C: The art of scientific computing* (Cambridge University Press, Cambridge, 1992).

[197] C. A. Haynam, D. V. Brumbaugh, and D. H. Levy, J. Chem. Phys. **81**, 2282 (1984).

[198] L. A. Philips and D. H. Levy, J. Chem. Phys. **85**, 1327 (1986).

[199] R. M. Helm, H. P. Vogel, and H. J. Neusser, Chem. Phys. Lett. **270**, 285 (1997).

[200] R. Wehrens and L. M. C. Buydens, Trends Analyt. Chem. **17**, 193 (1998).

[201] S. Chervenkov, P. Q. Wang, J. E. Braun, and H. J. Neusser, J. Chem. Phys. **121**, 7169 (2004).

[202] A. E. Nikolaev, G. Miszkiewicz, G. Berden, W. Leo Meetrs, J. Pfanstiel, and D. W. Pratt, J. Chem. Phys. **122**, 084309 (2005).

[203] S. Chervenkov, P. Q. Wang, J. E. Braun, S. Georgiev, C. K. Nandi, T. Chakraborty, and H. J. Neusser, J. Chem. Phys. **122**, 244312 (2005).

[204] M. Schmitt, D. Krüger, M. Böhm, C. Ratzer, V. Bednarska, I. Kalkman, and W. L. Meerts, Phys. Chem. Chem. Phys. **8**, 228 (2006).

[205] S. Chervenkov, R. Karaminkov, J. E. Braun, H. J. Neusser, S. S. Panja, and T. Chakraborty, J. Chem. Phys. **124**, 432302 (2006).

[206] G. R. Desiraju and T. Steiner, *The Weak Hydrogen Bond* (Oxford University Press, New York, 1999).

[207] G. A. Jeffrey, *An Introduction to Hydrogen Bond* (Oxford University Press, New York, 1997).

[208] S. H. Pine, J. B. Hendrickson, D. J. Cram, and G. S. Hammond, *Organic Chemistry*, 4th ed. (McGraw-Hill, New York, 1980).

[209] S. Tsuzuki, K. Honda, T. Uchimaru, M. Mikami, and K. Tanabe, J. Phys. Chem. A **103**, 8265 (1999).

[210] K. S. Kim, P. Tarakeshwar, and J. Y. Lee, Chem. Rev. **100**, 4145 (2000).

[211] M. Y. Shelley, H. L. Dai, and T. Troxler, J. Chem. Phys. **110**, 9081 (1999).

[212] R. K. Sampson, S. M. Bellm, J. R. Gascooke, and W. D. Lawrance, Chem. Phys. Lett. **372**, 307 (2003).

[213] R. N. Pribble, A. W. Garret, K. Haber, and T. S. Zwier, J. Chem. Phys. **103**, 531 (1995).

[214] H. Mahmoud, I. N. Germanenko, Y. Ibrahim, and M. S. El-Shall, Chem. Phys. Lett. **356**, 91 (2002).

[215] S. F. Boys and F. Bernardi, Mol.Phys. **19**, 553 (1970).

[216] O. Dimopoulou-Rademann, U. Even, A. Amirav, and J. Jortner, J. Phys. Chem. **92**, 5371 (1988).

[217] S. Chervenkov, P. Q. Wang, T. Chakraborty, and H. J. Neusser, Z. Phys. Chem. **221**, 619 (2007).

[218] J. W. Ribblett, D. R. Borst, and D. W. Pratt, J. Chem. Phys. **111**, 8454 (1999).

[219] W. Caminati, B. Vogelsanger, and A. Bauder, J. Mol. Spectrosc. **128**, 384 (1988).

[220] A. Hartford Jr. and J. R. Lombardi, J. Mol. Spectrosc. **35**, 413 (1970).

[221] J. K. G. Watson, Mol. Phys. **15**, 479 (1968).

[222] J. K. G. Watson, Mol. Phys. **19**, 465 (1970).

[223] H. Meyer, Annu. Rev. Phys. Chem. **53**, 141 (2002).

[224] M. H. Hui and S. A. Rice, J. Chem. Phys. **61**, 833 (1974).

[225] J. M. Hollas, E. Khalilipour, and S. N. Thakur, J. Mol. Spectrosc. **73**, 240 (1978).

[226] J. M. Hollas and T. Ridley, J. Mol. Spec. **89**, 232 (1981).

[227] J. A. Syage, F. A. Adel, and A. H. Zewail, Chem. Phys. Lett. **103**, 15 (1983).

[228] V. H. Grassian, E. R. Bernstein, H. V. Secor, and J. I. Seeman, J. Phys. Chem. **93**, 3470 (1989).

[229] S. Zilberg and Y. Haas, J. Chem. Phys. **103**, 20 (1995).

[230] C. H. Choi and M. Kertesz, J. Phys. Chem. A **101**, 3823 (1997).

[231] A. Karpfen, C. H. Choi, and M. Kertesz, J. Phys. Chem. A **101**, 7426 (1997).

[232] X. Gong and H. Xiao, Int. J. Quant. Chem. **69**, 659 (1998).

[233] H. J. Neusser and H. Krause, Chem. Rev. **94**, 1829 (1994).

[234] R. M. Helm, H. P. Vogel, H. J. Neusser, V. Storm, D. Consalvo, and H. Dreizler, Z. Naturforsch. **52a**, 655 (1997).

[235] R. M. Helm, M. Clara, T. L. Grebner, and H. J. Neusser, J. Phys. Chem. A **102**, 3268 (1998).

[236] R. M. Helm, H. P. Vogel, and H. J. Neusser, J. Chem. Phys. **108**, 4496 (1998).

[237] Y. Matsumoto, T. Ebata, and N. Mikami, J. Chem. Phys. **109**, 6303 (1998).

[238] R. M. Helm and H. J. Neusser, Chem. Phys. **239**, 33 (1998).

[239] P. Hobza and J. Sponer, Chem. Rev. **99**, 3247 (1999).

[240] H. J. Neusser and K. Siglow, Chem. Rev. **100**, 3921 (2000).

[241] S. Tsuzuki, K. Honda, T. Uchimaru, M. Mikami, and K. Tanabe, J. Am. Chem. Soc. **122**, 3746 (2000).

[242] C. Ramos, P. R. Winter, J. A. Stearns, and T. S. Zwier, J. Phys. Chem. A **107**, 10280 (2003).

[243] K. Sundararajan, K. S. Viswanathan, A. D. Kulkarni, and S. R. Gadre, J. Mol. Struct. **613**, 209 (2002).

[244] P. Tarakeshwar, H. S. Choi, S. J. Lee, J. Y. Lee, K. S. Kim, T.-K. Ha, J. H. Jang, J. G. Lee, and H. Lee, J. Chem. Phys. **111**, 5838 (1999).

[245] S. M. Beck, M. G. Liverman, D. L. Monts, and R. E. Smalley, J. Chem. Phys. **70**, 232 (1979).

[246] J. B. Hopkins, D. E. Powers, and R. E. Smalley, J. Phys. Chem. **85**, 3739 (1981).

[247] K. O. Börnsen, H. L. Selzle, and E. W. Schlag, J. Phys. Chem. **92**, 5482 (1988).

[248] H. J. Neusser, R. Sussmann, A. M. Smith, E. Riedle, and T. Weber, Ber. Bunsenges. Phys. Chem. **96**, 1252 (1992).

[249] S. Leutwyler, U. Even, and J. Jortner, J. Chem. Phys. **79**, 5769 (1983).

[250] S. Leutwyler and J. Bösiger, Z. Phys. Chem. **154**, 31 (1987).

[251] S. Leutwyler and J. Bösiger, Chem. Rev. **90**, 489 (1990).

[252] T. Weber, A. M. Smith, E. Riedle, H. J. Neusser, and E. W. Schlag, Chem. Phys. Lett. **175**, 79 (1990).

[253] T. Weber and H. J. Neusser, J. Chem. Phys. **94**, 7689 (1991).

[254] M. Schmidt, M. Mons, J. LeCalvé, P. Millié, and C. Cossart-Magos, Chem. Phys. Lett. **183**, 69 (1991).

[255] T. Weber, E. Riedle, H. J. Neusser, and E. W. Schlag, Chem. Phys. Lett. **183**, 77 (1991).

[256] Z. Xu, J. M. Smith, and J. L. Knee, J. Chem. Phys. **97**, 2843 (1992).

[257] R. Sußmann and H. J. Neusser, Chem. Phys. Lett. **221**, 46 (1994).

[258] E. Riedle and A. van der Avoird, J. Chem. Phys. **104**, 882 (1996).

[259] M. Becucci, G. Pietraperzia, N. M. Lakin, E. Castellucci, and P. Bréchignac, Chem. Phys. Lett. **260**, 87 (1996).

[260] P. Hobza, H. L. Selzle, and E. W. Schlag, J. Chem. Phys. **95**, 391 (1991).

[261] P. Hobza, O. Bludský, H. L. Selzle, and E. W. Schlag, J. Chem. Phys. **97**, 335 (1992).

[262] J. A. Menapace and E. R. Bernstein, J. Phys. Chem. **91**, 2533 (1987).

[263] O. Bludský, V. Špirko, V. Hrouda, and P. Hobza, Chem. Phys. Lett. **196**, 410 (1992).

[264] P. Parneix, N. Halberstadt, P. Bréchignac, F. G. Amar, A. van der Avoird, and J. W. van-Bladel, J. Chem. Phys. **98**, 2709 (1993).

[265] S. Melandri, D. Consalvo, W. Caminati, and P. G. Favero, J. Chem. Phys. **111**, 3874 (1999).

[266] I. López-Tocón, J. C. Otero, M. Becucci, G. Pietraperzia, E. Castellucci, and P. Bréchignac, Chem. Phys. **269**, 29 (2001).

[267] R. J. Doyle, E. S. J. Love, R. Da Campo, and S. R. Mackenzie, J. Chem. Phys. **122**, 194315 (2005).

[268] B. Brutschy, Chem. Rev. **100**, 3891 (2000).

[269] J. D. Dunitz and R. Taylor, Chem. Eur. J. **3**, 89 (1997).

[270] P. Tarakeshwar, K. S. Kim, and B. Brutschy, J. Chem. Phys. **110**, 8501 (1999).

[271] A. J. Gotch and T. S. Zwier, J. Chem. Phys. **96**, 3388 (1992).

[272] H. S. Gutowsky, T. Emilsson, and E. Arunan, J. Chem. Phys. **99**, 4883 (1993).

[273] S. Suzuki, P. G. Green, R. E. Bumgarner, S. Dasgupta, W. A. Goddard, and G. A. Blake, Science **257**, 942 (1992).

[274] S. Georgiev, H. J. Neusser, and T. Chakraborty, J. Chem. Phys. **120**, 8015 (2004).

[275] R. N. Pribble and T. S. Zwier, Science **265**, 75 (1994).

[276] H. D. Barth, K. Buchhold, S. Djafari, B. Reimann, U. Lommatzsch, and B. Brutschy, Chem. Phys. **239**, 49 (1998).

[277] V. Brenner, S. Martrenchard-Barra, P. Millie, C. Dedonder-Lardeux, C. Jouvet, and D. Solgadi, J. Phys. Chem. **99**, 5848 (1995).

[278] P. Biswas and T. Chakraborty, (Unpublished results).

[279] N. M. Lakin, G. Pietraperzia, M. Becucci, and M. Coreno, J. Mol. Struct. **410**, 59 (1997).

[280] S. Sun and E. R. Bernstein, J. Am. Chem. Soc. **118**, 5086 (1996).

[281] S. J. Martinez III, J. C. Alfano, and D. H. Levy, J. Mol. Spectrosc. **158**, 82 (1998).

[282] N. Guchhait, T. Ebata, and N. Mikami, J.Am.Chem.Soc. **121**, 5705 (1999).

[283] P. D. Godfrey, R. N. Jorissen, and R. D. Brown, J. Phys. Chem. A **103**, 7621 (1999).

[284] R. D. Brown and P. D. Godfrey, J. Phys. Chem. A **104**, 5742 (2000).

[285] P. Butz, R. T. Kroemer, N. A. Macleod, E. G. Robertson, and J. P. Simons, J.Phys.Chem. **105**, 1050 (2001).

[286] P. Butz, N. A. Macleod, L. C. Snoek, F. O. Talbot, and J. P. Simons, Central Laser Facility Annual Report **2000/2001**, 97 (2002).

[287] S. S. Panja and T. Chakraborty, J. Phys. Chem. A **107**, 10984 (2003).

[288] M. Hockridge and E. G. Robertson, J. Phys. Chem. A **103**, 3618 (1999).

[289] J. E. Braun, T. L. Grebner, and H. J. Neusser, J. Phys. Chem. **102**, 3273 (1998).

[290] R. Weinkauf, F. Lehrer, E. W. Schlag, and A. Metsala, Faraday Discuss. **115**, 363 (2000).

[291] T. Weber, A. von Bargen, E. Riedle, and H. J. Neusser, J. Chem. Phys. **92**, 90 (1990).

[292] P. W. Joireman, R. T. Kroemer, D. W. Pratt, and J. P. Simons, J. Chem. Phys. **105**, 6075 (1996).

[293] H. Krause and H. J. Neusser, J. Chem. Phys. **99**, 6278 (1993).

[294] E. Riedle, R. Sussmann, T. Weber, and H. J. Neusser, J. Chem. Phys. **104**, 865 (1996).

[295] C. G. Eisenhardt and H. Baumgärtel, Ber. Bunsenges. Phys. Chem **102**, 12 (1998).

[296] S. R. Haines, C. E. H. Dessent, and K. Müller-Dethlefs, J. Electron. Spectrosc. Relat. Phenom. **108**, 1 (2000).

[297] O. Dopfer, M. Melf, and K. Müller-Dethlefs, Chem. Phys. **207**, 437 (1996).

[298] D. M. Chapman, F. J. Hompf, K. Müller-Dethlefs, E. Waterstradt, P. Hobza, and V. Špirko, Chem. Phys. **239**, 417 (1998).

[299] G. A. Jeffrey and W. Saenger, *Hydrogen Bonding in Biological Structures* (Spinger, Berlin, 1991).

[300] S. H. Snyder, *Drugs and the Brain* (Scientific American Library, New York, 1999).

[301] A. D. Strosberg, Annu. Rev. Pharmacol. Toxicol. **37**, 421 (1997).

[302] M. F. Zigmond, *Fundamental Neuroscience* (Academic Press, London, 1998).

[303] J. Yao, H. S. Im, M. Foltin, and E. M. Bernstein, J. Phys. Chem. A **104**, 6197 (2000).

[304] U. Boesl, H. J. Neusser, and E. W. Schlag, J. Chem. Phys. **72**, 4327 (1980).

[305] W. Dietz, H. J. Neusser, U. Boesl, E. W. Schlag, and S. H. Lin, Chem. Phys. **66**, 105 (1982).

[306] J. E. Braun, T. Mehnert, and H. J. Neusser, Int. J. Mass. Spectrom. **203**, 1 (2000).

List of Figures

1.1 Bonding potential of weak molecular interactions. 21
1.2 Molecular interactions and molecular bonds. 26

6.1 Resonant two-photon ionization (R2PI) scheme. 62
6.2 Schematic view of the molecular-beam set up and the time-of-flight mass spectrometer set up. 64
6.3 Schematic representation of the laser system for low- and high-resolution resonance enhanced two-photon ionization experiments. 66
6.4 Block diagram of the genetic algorithm computer-aided rotational fitting routine. 71

7.1 Atom labels of the styrene-acetylene complex. 77
7.2 Geometries of the two lowest-energy conformers of the 1:1 complex of styrene with acetylene. 80
7.3 Low-resolution R2PI spectra of styrene and its complexes with acetylene. 81
7.4 Low resolution R2PI spectra of styrene and its complexes with acetylene plotted with a common origin. 82
7.5 High-resolution two-colour UV R2PI spectrum of the $S_1 \longleftarrow S_0$, 0_0^0 origin band of styrene. 84
7.6 High-resolution two-colour UV R2PI spectrum of the $S_1 \longleftarrow S_0$, 0_0^0 origin band of styrene-acetylene. 86

8.1 Theoretically predicted electronic ground state structure of the complex between styrene and acetylene. 96
8.2 Low-resolution one-colour R2PI spectra of the $S_1 \longleftarrow S_0$ electronic transition of jet-cooled styrene and its complexes with Ar. 98
8.3 High-resolution two-colour UV R2PI spectrum of the $S_1 \longleftarrow S_0$, 0_0^0 origin band of the complex between styrene and Ar. 100

9.1 Geometries of the four lowest-energy conformers of the 1:1 complex of *p*-fluorostyrene and water. 106

9.2 Low-resolution spectra of the *p*-fluorosryrene monomer and the complex bewteen *p*-fluorostyrene and water. 110
9.3 Highly resolved spectrum of the 0_0^0 origin band of the *p*-fluorostyrene-water complex. 113

10.1 One-colour low-resolution R2PI spectrum of 2-phenylethanol. 118
10.2 High-resolution two-colour UV R2PI spectrum of the origin band of 2-phenylethanol. 119
10.3 High-resolution two-colour UV R2PI spectra of the *cis* and *trans* conformations of the 2-PE·Ar complex. 122
10.4 Optimized structure of the 2-PE monomer at the MP2/6-31G (*d*, *p*) level of theory: 3D image and atom labels 125
10.5 Electronic ground state structures of the *cis* conformer of the 2-PE·Ar complex optimized at the MP2/6-31G (*d*, *p*) level of theory. 126

11.1 Low-resolution spectra of the ephedrine monomer measured at its parent (*m/z*=165) and fragment (*m/z*=58) mass channels. 138
11.2 Experimental and calculated highly resolved spectra of the origin band of the ephedrine monomer. 142

List of Tables

4.1 Rigid asymmetric-top energy levels 48

6.1 Doppler broadening as a function of the carrier gas and the nozzle-to-skimmer distance. 65

7.1 Binding energies, typical geometrical parameters and rotational constants for the ST·C_2H_2 complex for its ground, S_0 ans first excited, S_1, electronic state obtained from *ab initio* calcuations. 79
7.2 Experimental and calculated (CIS/6-311++G (*d*, *p*)) level of theory) intermolecular vibrational frequencies of the styrene-acetylene complex. 83
7.3 Experimental rotational constants, transition moment ratio, origin band position, and rotational temperature of the styrene monomer. 85
7.4 Experimental rotational constants, transition moment ratio, origin band position, and rotational temperature of the observed complex of styrene with acetylene. . . 87

8.1 Theoretically predicted structural and inertial parameters of the complex of styrene with Ar. 96
8.2 Experimental rotational constants, transition moment ratio and band origin frequency of the styrene-argon complex. 99

9.1 Theoretical molecular parameters of the four energetically most stable conformations of the *p*-FST·H_2O complex obtained from *ab initio* quantum chemistry calculations. 107
9.2 Molecular rotational constants and transition moment ratio of the most abundant structure of the complex between *p*-fluorostyrene and water. 113

10.1 Experimental parameters of the 2-PE monomer obtained from the fit of its highly resolved R2PI spectrum. 120
10.2 Experimental parameters of the *cis* 2-PE·Ar complex obtained from the fit of its highly resolved R2PI spectrum. 123

10.3 Theoretical geometrical parameters of the *gauche* conformer of 2-phenylethanol for its ground, S_0, and first excited, S_1 electronic state. 126
10.4 Theoretical geometrical parameters for the ground, S_0, electronic state of the *cis* and *trans* conformers of the complex between 2-phenylethanol and Ar. 127
10.5 Position of the Ar atom in the 2-PE·Ar complex determined from the Kraitchman equations. 128
10.6 Orientation of the transition moment vector relative to the benzene ring in 2-phenylethanol and its complex with Ar. 129

11.1 Classification of the observed vibrational bands in the low-resolution one-colour two-photon R2PI spectrum of the ephedrine monomer. 140
11.2 Best-fit experimental parameters of the most abundant ephedrine conformer. . . . 142

List of Publications

S. Chervenkov, P. Q. Wang, J. E. Braun, and H. J. Neusser, *Fragmentation and Conformation Study of Ephedrine by Low- and High-Resolution Mass Selective UV Spectroscopy*,
J. Chem. Phys. **121** (15), 7169 (2004).

S. Chervenkov, P. Q. Wang, R. Karaminkov, T. Chakraborty, J. E. Braun, and H. J. Neusser, *High Resolution UV Resonance Two Photon Ionization Spectroscopy with Mass Selection of Biologically Relevant Molecules in the Gas Phase* in *13th International School on Quantum Electronics: Laser Physics and Applications, P. A. Atanasov, S. V. Gateva, L. A. Avramov, A. A. Serafetinides, eds.*,
Proc. SPIE **5830**, 246 (2005).

S. Chervenkov, P. Q. Wang, J. E. Braun, S. Georgiev, and H. J. Neusser, *High Resolution Ultraviolet Spectroscopy of p-fluorostyrene-Water: Evidence for a σ Hydrogen-bonded Dimer*,
J. Chem. Phys. **122**, 244312 (2005).

S. Chervenkov, R. Karaminkov, J. E. Braun, H. J. Neusser, S. S. Panja, and T. Chakraborty *Specific and Nonspecific Interactions in a Molecule with Flexible Side Chain: 2-phenylethanol and its 1:1 Complex with Argon studied by High Resolution UV Spectroscopy*,
J. Chem. Phys. **124**, 234302 (2006).

S. Chervenkov, P. Q. Wang, J. E. Braun, T. Chakraborty, and H. J. Neusser, *Evidence for a C-H$\cdots\pi$ Type Weak Interaction: 1:1 Complex of Styrene with Acetylene Studied by Mass Selective High-Resolution UV Spectroscopy and Ab initio Calculations*,
Phys. Chem. Chem. Phys. **9**, 837 (2007).

S. Chervenkov, P. Q. Wang, T. Chakraborty, and H. J. Neusser, *Van der Waals Bonding to a Molecule with π-electron Conjugation: Styrene-Argon Complex Studied by Mass Selective High Resolution R2PI Spectroscopy and Ab initio Calculations*,
Z. Phys. Chem. **221**, 1 (2007).

R. Karaminkov, S. Chervenkov, P. Härter, and H. J. Neusser, *Resonance-Enhanced Two-Photon Ionization Mass Spectrometry of a Flexible Molecule: Indication of State Selective Fragmentation in Ephedrine*,
submitted for publication.

Poster and Oral Presentations

17th International Conference on High Resolution Molecular Spectroscopy
Prague, The Czech Republic, 01. 09.-05. 09. 2002
Poster
High Resolution Spectroscopy and Stark Splitting in Aromatic Molecules: Benzonitrile and Fluorostyrene

18th Colloquium on High Resolution Molecular Spectroscopy
Dijon, France, 08. 09.-12. 09. 2003
Poster
High Resolution Spectroscopy of Fluorostyrene, 3-Methylindole, Ephedrine, and Their Noble Gas and Water Clusters

EURESCO Conference on Molecules of Biological Interest in the Gas Phase
Exeter, The United Kindom, 13. 04.-18. 04. 2004
Poster
High Resolution Spectroscopy of Biologically Relevant Molecules: Ephedrine and 2-Phenylethanol

18th International Conference on High Resolution Molecular Spectroscopy
Prague, The Czech Republic, 08. 09.-12. 09. 2004
Poster
High Resolution Spectroscopy of Ephedrine and 2-Phenylethanol and Their Water Clusters
Awardee of the "Joseph Plíva Prize"

13th International School on Quantum Electronics: Laser Physics and Applications
Bourgas, Bulgaria, 20. 09.-24. 09. 2004
Poser and Oral Presentation
High Resolution UV Resonance Enhanced Two-Photon Ionization Spectroscopy with Mass Selection of Biologically Relevant Molecules in Gas Phase

91st Bunsen Colloquium, Spectroscopy and Dynamics of Molecular Coils and Aggregates
Göttingen, Germany, 05. 04.-06. 04. 2005
Poster
High Resolution Spectroscopy of Ephedrine and 2-Phenylethanol and Their Water Clusters

Kansas State University, Department of Physics Seminar
Manhattan, KS, USA, 18. 06. 2005
Invited talk
An Insight into the Microworld: Investigation of Structure and Dynamics of Isolated Molecules and Clusters by Laser Spectroscopy Techniques

60th International Symposium on Molecular Spectroscopy
Columbus, OH, USA, 20. 06.-24. 06. 2005
Oral presentation
Conformation Study of 2-Phenylethanol and Ephedrine, and Their Hydrated Clusters by Mass Selective High Resolution UV Spectroscopy and Ab initio Calculations

Technische Universität München, Physikalische Chemie I, Kaffeeseminar
München, Germany, 03. 02. 2006
Oral presentation
Conformational Preferences of Biomolecules and Complexes Studied by High Resolution UV Laser Spectroscopy with Mass Selectivity

Gordon Research Conference, Electronic Spectroscopy and Dynamics
Les Diablerets, Switzerland, 10. 09.-15. 09. 2006
Poster
High-Resolution Mass Selective UV R2PI Spectroscopy of Flexible and Biological Molecules and Complexes: Weak Interactions and Conformational Structures

Index

Symbols

p-hydroxy-3-phenyl-1-propionic acid, 132
π electron
  delocalized, 88
2-phenylethanol (2-PE), 9, 99, 115–119, 121, 124–130, 132, 133, 136
  anti, 132
  cation, 117
  gauche, 115, 116, 124, 125, 129–132
2-phenylethylamine, 116, 132
3-phenyl-1-propionic acid, 129

A

absorption, 117, 138
acceptor, 22, 76
  hydrogen bond, 77
  proton, 22, 80, 88, 90
ACES II, 38
acetylcholine, 136
acetylene (C_2H_2), 9, 64, 76, 78, 81, 89–91
acid dissociation constant, 76
additivity rule, 101
adiabatic cooling, 55
adiabatic expansion, 63, 104
adiabatic ionization energy (AIE), 117
adrenalin, 136
alkanes, 76
alkynes, 76
amplification, 67
amplifier, 66
amplitude, 33
angle, 36
  dihedral, 36, 51, 124, 125
  planar, 51, 124, 125
angular, 45
  momentum, 46
  velocity, 45
anharmonicity, 100
anti-Stokes, 59
approximation, 30, 40
  Born-Oppenheimer, 30, 43, 44, 50
    break-down, 44
  electric dipole, 40, 49
argon (Ar), 9, 94, 98, 99, 105, 115–117, 123–125, 128–132, 137
aromatic amine, 116
aromatic molecule, 9, 118
aromatic ring, 94, 104, 108, 111, 115–117, 130, 131, 133
aspartate, 136
asymmetry paramater
  Ray, 48
asymmetry parameter, 48
axis of inertia
  principal, 45, 120, 121, 123, 128, 129
axis switching, 101, 121
axis system
  principal, 89

B

B3LYP, 88–90, 105, 108, 114
B3LYP/6-311++G (*d*, *p*), 79
B3LYP/6-311++G (*d*, *p*), 80, 90
B3LYP/6-311+G (*d*, *p*), 105, 109
backing pressure, 105
band contour

low-resolution, 120
rotational, 120
band structure
rotational, 123, 130
bandwidth, 67
basis set superposition error (BSSE), 80, 105
benzene (Bzn), 51, 76, 116, 126, 129, 131, 132
cation, 138
derivative, 126, 130
monosubstituted, 130
unsubstituted, 132
benzene ring, 24, 88, 90, 94, 99–101, 108, 115, 123–125, 128, 129, 131–133, 139
Bernardy, 105
beta-barium-borate (BBO), 66, 67
binding energy, 105, 108, 109, 116, 124, 130, 131, 133
binding site, 9, 116, 124, 125, 130
biological membranes, 104
biomolecule, 116
blue shift, 110, 111
Bohr radius, 20
Boltzmann
constant, 50
population, 130
bond, 6
charge-transfer (CT), 24
chemical, 17
covalent, 5, 6, 17
covalent nonpolar, 17
covalent polar, 17
homopolar, 17
ionic, 17
metallic, 17
covalent
X-H, 23
dihydrogen, 23, 24
dispersion, 25
hydrogen, 22, 25, 116, 130, 131
acceptor, 104
blue-shifting, 23
C-H$\cdots\pi$, 87
conventional, 23
improper, 23
intermolecular, 9
intramolecular, 115, 133
nonconventional, 76
nonconventional C-H·Y, 22
π, 114, 115, 130
π-HO, 130, 131
proper, 23
red-shifting, 23
σ, 114
intramolecular
OH$\cdots\pi$, 9
ion-mediated, 24
nonclassical π-hydrogen, 132
nonconventional
CH$\cdots\pi$, 9
noncovalent
classical X-H$\cdots$Y, 116
hydrogen, 6, 116
nonclassical π-hydrogen, 116
π, 25
quadrupole-quadrupole, 24, 25
σ, 25
unsaturated carbon, 94
boxcar integrator, 68
Boys, 29, 105
broadening, 8
Doppler, 8, 64
lifetime, 112
Brutschy, 105, 111
buffer gas, 64, 105
Butz, 139–141

C

CADPAC, 38

calculation
ab initio, 28, 29, 76, 87, 90, 94, 95, 101, 109, 111, 112, 118, 120, 125, 126, 128–132, 136, 141, 143
B3LYP, 77
MP2, 76, 77
quantum chemistry
ab initio, 102
ab initio, 8, 28, 75, 78, 95, 101, 104, 105, 110, 115, 121, 130, 132
carrier gas, 55, 64, 118
catalysis, 6
cation, 24, 57, 137
metallic, 24
centre of mass (COM), 51, 108, 127
centrifugal distortion, 50
constant, 50
chloroform, 24
chromophore, 9
CIS, 78, 104, 108
CIS/6-311++G (*d*, *p*), 87, 90, 121, 132
CIS/6-31G (*d*), 120
CIS/6-31G (*d*, *p*), 120, 124, 125
cluster, 127
2-PE·Ar, 123, 129
cis, 123
trans, 123
aromatic molecule·Ar, 118
Bzn·Ar, 116
formation, 125, 127, 132
ion, 130
molecular, 5
noble-gas, 126
weakly bound, 55
cluster operator, 33
one-particle excitation, 33
two-particle excitation, 33
Coester, 33
collisional cooling, 64
complete active space self-consistent field (CASSCF), 111
complex
2-PE·Ar, 115–118, 121, 123–128, 130, 132
cis, 125
cis, 115, 121, 123–125, 127–133
trans, 115, 121, 124, 125, 131, 132
trans, 125
2-PE·H_2O, 130
acetylene·ethane, 76
Bzn·C_2H_2, 88
Bzn·$(C_2H_2)_2$, 89
Bzn·C_2H_2, 91
Bzn·Ar, 125, 130
Bzn·Ar_2, 130, 131
Bzn·H_2O, 76, 77, 111, 130
Bzn·Ar, 116
chloroform·fluorobenzene, 24
deuterated, 109
dimeric, 76
EPD·H_2O, 135, 139, 143
cation, 139
p-fluorobenzene·water, 105
fluorobenzene·H_2O (FBzn·H_2O), 111
fluorobenzene·water (FBzn·H_2O), 108
formation, 7
fragmentation, 7
hydrated, 82, 118
indole·benzene, 116
ionic, 130
molecular, 5–8, 57, 58, 63, 65, 69
noncovalently bound, 7
p-difluorobenzene·water, 105, 110, 114
p-FST·$(H_2O)_2$, 109
p-FST·H_2O, 104, 105, 108–112
p-fluorotoluene·Ar, 131
p-FST·H_2O, 110
phenol·Ar, 131
π hydrogen bonded, 105

σ hydrogen bonded, 105
singly hydrated, 9
ST·C_2H_2, 75, 78, 81–83, 85, 87, 89, 90
ST·$(C_2H_2)_2$, 81
ST·Ar, 95, 101
ST·Ar_2, 100, 101
ST·Ar, 94, 95, 97, 99, 100
ST·Ar_2, 95, 100
ST·H−2O, 110
ST·H_2O, 77, 89
ST·$(H_2O)_n$, 109
ST·Ar, 82
ternary
phenol·water·Ar, 131
toluene·Ar, 131
van der Waals, 76, 101, 130
weakly bound, 6, 7, 62, 90
computer-assisted fitting routine, 78
computer-assisted fitting techniques, 68
computer-assisted rotational fit, 90
configuration interaction (CI), 30, 31
configuration interaction singles (CIS), 31
configuration mixing, 30
conformation, 6, 8, 36, 55, 78, 116, 124, 129
2-phenylethanol (2-PE)
cis, 125
gauche, 124, 129, 132
2-PE·Ar
cis, 131
trans, 131
anti, 103
in-plane, 78
out-of-plane, 78
conformer, 36, 105, 109, 115, 118, 135, 139–141
2-phenylethanol (2-PE), 118
anti, 132
gauche, 119
gauche, 117–120, 124, 125, 129–132
2-PE·Ar
cis, 121, 123–125, 127–133
trans, 121, 123–125, 131
in-plane, 108, 114
anti, 112, 114
gauche, 114
out-of-plane, 105, 108, 114
conjugation, 90, 91, 94, 101
π-electron, 9
contraction coefficient, 29
convolution, 85
cooling conditions, 109
Coriolis coupling, 44, 50
Coulomb, 32
Coumarin 521, 67, 117
counterpoise correction, 80
coupled-cluster (CC), 33
cross correlation, 69, 78, 84, 95, 105, 117, 137
crossover, 70
crystal engineering, 76
crystal packing, 6, 76

D

data acquisition system, 63, 68
deflector, 65
delay generator, 68
delocalization, 94, 101
density functional theory (DFT), 34
B3LYP, 78, 87, 105
Dewar, 22
diafragm, 65
dimer, 110, 124, 125
hydrogen-bonded
phenol·water, 131
p-FST·H_2O, 110
dipole moment, 19
electric, 19
local, 111
directionality, 23, 25

dissociation, 137, 143
dissociation energy, 62, 63
dissociation limit, 88
dissociation threshold, 130
distortion coefficient, 45
distribution
  Boltzmann, 49
  charge, 18
  electron density, 19, 34, 35, 128
  mass, 128
  permanent charge, 25
  probability, 35
  static-charge, 18
  thermal, 49
DNA, 6, 7
donor, 22
  electron, 24, 108
  hydrogen bond, 76
  proton, 22, 23, 80, 87–90
dopamine, 136
doubling crystal, 67
downhill simplex method, 69
drug design, 6
drug synthesis, 136
drug-receptor matching, 6
dye laser
  broad-band, 67
  broad-band tuneable, 66
  ring, 117
    continuous wave (cw), 66, 67
    narrow-band, 66, 67
    single-mode, 66, 67

E

effect, 44
  electron-withdrawing, 9
  Herzberg-Teller, 44, 50
  Jahn-Teller, 50
  mesomeric, 9, 94, 104
  saturation, 97
electric charge, 19
electron
  delocalized, 9
electron affinity, 17, 24
electron attraction, 104
electron correlation, 29, 30, 104, 105
electron density, 129, 131, 133
electron diffraction, 60
electron gas, 18
electronegative atom, 22
electronegative substituent, 9
electronegativity, 17, 133
electronic origin, 109, 130
elitism, 70
energy, 38
  vibrational, 38
    zero-point (ZPVE), 38
energy calculation, 36
  single point, 36, 78
energy minimization, 36
enthalpy, 25
entropy, 25
enzyme catalysis, 6
ephedra, 136
ephedrine (EPD), 9, 117, 135–141, 143
  anti-gauche conformer, 140
  cation, 138, 139
epinephrine, 136
equation, 28
  Kraitchman, 51, 126–128, 131, 132
  Schrödinger, 28, 30, 43
    time-dependent, 39
  secular, 31
equilibrium geometry, 35
error, 30
  truncation, 30
evaluation, 69
evaporative cooling, 97

excess energy, 88, 108, 117, 130, 137
excimer laser, 66–68
  XeCl, 66
excitation, 62, 119
excitation photon, 66

F

Fabry-Perot interferometer, 68
  confocal, 68
factor, 29
  normalization, 29
Fermi's golden rule, 40
fitness, 69
fitting routine
  computer-assisted, 117
fluorescence, 7
fluorescence emission, 7
fluorination, 111
fluorine, 77, 104, 108, 111
fluorine-substituted compounds, 104
fluorobenzene, 24, 105, 111
force constant, 35
  mass-weighted, 38
Fourier transform-limited, 67
fragment, 139
fragmentation, 8, 9, 62, 83, 88, 97, 100, 109, 110, 118, 123, 130, 135–141, 143
frequency, 38, 67
  absolute, 67
  fundamental, 38
frequency doubling, 66
frequency mixer, 58
fringe pattern, 68
Fujii, 76
function, 28
  basis, 28
    Gaussian-type (GT), 29
    Slater-type (ST), 29
  configuration, 30
  configuration-state (CSF), 30
  Gaussian, 29
    primitive, 29
  multielectron, 30
  one-electron spatial, 28
  wave, 28, 32
    antisymmetricity, 32
    electronic, 33
    orthonormal, 39
    stationary-state, 39
    time-independent, 39
functional, 35
  B3LYP, 35

G

GAMESS, 38
gas electron diffraction, 56
Gaussian, 38, 78, 95, 105, 124
generation, 78, 105, 117
genetic algorithm (GA), 69, 78, 85, 97, 101, 105, 112, 115, 117, 121, 123, 128, 137
global optimizer, 37
glutamate, 136
glycine, 136
gradient method, 69
grid search, 78, 90
group
  alcoholic, 116
  amino, 137, 143
  hydroxyl, 129
  methyl, 137
  OH, 117, 131–133
  phenyl, 76
  unsaturated, 87
  vinyl, 88, 89, 91, 94, 101, 104, 108, 111
  X-H, 22

H

Hamiltonian, 27, 32, 39, 40
  asymmetric top

Watson, 85, 112
nonrelativistic, 28
one-electron, 27
Heitler, 20
helium (He), 118
helium droplet, 56
Hessian, 38
HF, 108
high-Q cavity, 59
histamine, 136
Hohenberg-Kohn theorem, 34
hot band, 118
hybrid spectrum, 85, 86, 97, 112, 119, 140
hybridization, 70
hypersurface, 36
Hänsch, 67
Hückel, 27

I

individual, 69, 78, 95, 105, 117, 137
inertia defect, 84, 86
inertial parameter, 8, 88, 97
interaction, 5
Ar-Ar, 116
bonding, 18
charge-transfer (CT), 6, 23
covalent, 5
dispersion, 9, 19, 23, 115, 116, 130–133
intermolecular, 9
electrostatic, 6, 18, 23
exchange, 20
hydrophobic, 6, 25, 104
induction, 23
interelectronic, 28
intermolecular, 6, 25, 128, 132
intramolecular, 25, 128, 139
London, 19
metal coordination, 6
multipole, 24
nonbonded, 5, 6, 9
intermolecular, 6
nonbonding, 18
noncovalent, 5, 6, 18, 116
attractive, 18
intermolecular, 9
intramolecular, 6, 9
repulsive, 18
nonspecific, 131
π-hydrogen, 76
repulsive, 20
stacking, 6
three-body, 100
through-ring, 101
van der Waals, 94, 95, 98, 129, 131
vibration-rotation, 44
weak, 5, 8, 18, 55
dispersion, 18
electrostatic, 18
inductive, 18
intermolecular, 6
intramolecular, 9
interatomic distance, 51, 125
interference, 60
interference filter, 67
internal rotation, 109
ion laser, 67
Ar^+, 67, 78, 95, 117
ionization, 62, 88, 100, 117, 121, 135, 137, 140
vertical, 130
ionization energy, 138
adiabatic, 130
ionization limit, 63
ionization photon, 66, 88
isoenergetic, 130, 131
isomerization, 8
iteration, 95, 137

J

Jaguar, 38
jet expansion, 89
Johnson, 58
Jortner, 97

K

kinetic energy, 46, 65
  rotational, 46
Kohn, 35
Kümmel, 33

L

LabVIEW, 68
ladder switching, 138
laser
  continuous-wave (cw), 57
  infrared, 58
  pulsed, 57
least squares, 69
Lehn, 6
Levine, 32
Lewis, 5
lifetime, 85
Lombardi, 84
London, 19, 20
lone electron pair, 22
lone pair, 130

M

Müller-Dethlefs, 58
macromolecule, 6, 24
Mahmoud, 77, 89, 109, 110
mass analysed threshold ionization (MATI), 130
mass effect, 89, 91, 101, 112, 128
mass selection, 78, 104, 117
mass selective, 116, 135
mass selectivity, 7, 8, 95, 137, 141
mass spectrometer, 63
  time-of-flight (TOF), 63, 68, 104
    Wiley-McLaren, 64
matrix element, 38
matrix isolation, 56
Meerts, 57
mesh, 65
mesomeric effect, 111
methane, 76
methanol, 64
method, 30, 36
  variational, 30
micelles, 104
microchannel plate, 65
microsolvation, 94, 112
minimum, 36
  global, 36
  local, 36
mirror
  plano-concave, 59
mode (vibrational)
  intermolecular, 109
  intramolecular, 109
  stretching
    antisymmetric, 111
mode(vibrational), 118
model, 27
  molecular orbital, 27
  semiempirical, 27
molecular beam, 8, 55, 86, 95, 104, 119, 124, 133, 137, 139
  cold, 55, 64, 115, 117
  jet-cooled, 117, 132
  supersonic, 8, 78
molecular electronics, 6
molecular jet, 97
molecular mechanics (MM), 35
molecular recognition, 6, 76
molecular transport, 6
Molpro, 38
moment of inertia, 45, 46, 60

principal, 45
MP2, 78, 88, 89, 105, 108, 114
MP2/6-311++G (*d*, *p*), 79
MP2/6-311++G (*d*, *p*), 80, 87, 90, 95
MP2/6-31G (*d*, *p*), 124, 125, 128, 130, 131
MP2/cc-pVTZ, 95, 101
multipole moment, 18
mutation, 69, 70

N

neuron, 136
neurotransmission, 6
neurotransmitter, 9, 116, 132, 135, 136
noble-gas atoms, 94
noradrenalin, 136
norephedrine, 136
norepinephrine, 136
nozzle, 68, 137
heatable, 63
pulsed, 55, 63, 105
nucleon, 43

O

operator, 32
Coulomb, 32
exchange, 32
optical parametric oscillator (OPO), 58
optimization, 36, 124
geometry, 36
method
gradient, 36
Newton-Raphson, 36
steepest-descend, 36
multidimensional, 36
structural, 124, 125
orbital, 23
antibonding, 23
molecular, 28
vacant, 24, 30
orbital exponent, 29
oscillator, 66
overtone, 109

P

p-difluorobenzene, 105
p-fluorostyrene (*p*-FST), 9, 104, 105, 109, 111
p-fluorotoluene, 131
parent molecule, 51, 127
Pauli exclusion principle, 18, 20, 28
perturbation theory, 18, 19, 32
first-order, 18
Møller-Plesset, 32
second-order, 19
phenethylamine (PEA), 136
phenol, 131
phenyl ring, 76, 87, 89, 91
phenylalanine, 136
photodiode, 68
π electron, 89, 90, 94, 100, 125, 129, 131–133
π-electron density, 132
Pimentel, 56
pinhole, 67
plane wave, 41
polarizability, 19
Pople, 32
population, 69
position vector, 19
potassium-dihydrophosphate (KDP), 66, 67
potential, 21
attractive, 21, 25
ionization, 24
Lennard-Jones, 22
Morse, 22
repulsive, 21
torsional, 86
potential minimum, 88
local, 88
Pratt, 57, 86, 114
protein, 6, 104

protein folding, 132
protic solvents, 104
pseudoephedrine, 136
pulsed amplification, 67

Q

Q-Chem, 38
quadrupole moment, 19
    electric, 19
quantum number
    rotational, J, 85

R

random number generator, 69
receptor, 116, 136
red shift, 118, 124, 130, 131
reduced mass, 51
repeller plate, 65
reproduction, 69
resonance condition, 41
RHF, 105, 114
Rhodamine 6G, 67, 78, 95
Riedle, 67
rigid body, 45
Roothan, 28
rotational constant, 8, 46, 50, 68, 69, 86, 112, 119–121, 123–125, 127, 132, 135, 136, 141, 143
rotational contour, 114
rotational fit
    computer-aided, 115, 120, 123
rotational structure, 8, 119, 121, 123, 128
Rydberg series, 57
Rydberg state, 57
    high-lying, 57

S

saddle point, 36, 80
Salour, 67
Sander, 58
saturation, 85, 141
Saykally, 59
Schlag, 58
search method, 37
    diffusion equation, 37
    distance-geometry, 37
    genetic algorithm (GA), 37
    grid, 37
    low-mode, 37
    Metropolis, 37
    molecular dynamics, 37
    Monte Carlo, 37
    random, 37
    stochastic, 37
    systematic, 37
second harmonic generation (SHG), 67
secondary structure, 6
selection, 69
selection rule, 41, 49
self-consistent field, 28
    Hartree-Fock (HF SCF), 28
semiclassical theory, 40
sequence transition, 109
serotonin, 136
Sham, 35
shell, 28
signal-to-noise ratio, 69, 140
Simons, 136, 139, 143
simulaton annealing, 69
single rotational line assignment, 68
skimmer, 63, 64, 105
Slater determinant, 33
slit jet, 59
solvation, 6
SPARTAN, 38
spectroscopy, 7
    cavity ring-down (CRD), 59
    coherent ion-dip, 58
    dispersed fluorescence (DF), 76

double resonance
IR ion-dip, 136
IR-UV, 76, 130
IR-UV ion-depletion, 58
UV hole-burning, 136
UV-UV hole-burning, 58
double-resonance, 58
electronic, 56
far-infrared (far-IR), 56, 59
fluorescence detection, 84
fluorescence excitation (FE), 56, 76, 86
gas electron diffraction, 60
high-resolution, 117
infrared, 7
ion-depletion
infra-red (IR), 111
laser induced fluorescence (LIF), 7, 56, 58, 98
low-resolution, 7, 117
mass analysed threshold ionization (MATI), 56, 57, 116
mass selective, 90
microwave, 7, 56, 59, 84, 86, 94, 98, 120
near-infrared (near-IR), 56, 58
pump-probe, 60
Raman, 56, 59
resonance enhanced multiphoton ionization (REMPI) UV, 57, 58
resonance enhanced two-photon (R2PI) UV
low-resolution, 94
one-colour, 94
two-colour, 94
resonance enhanced two-photon ionization (R2PI) UV, 7, 62, 63, 76, 78, 104, 108, 115, 117, 136, 137
high-resolution, 8, 63, 90, 94, 98, 118–121, 132, 135–137, 140, 141
low-resolution, 63, 90, 117, 130, 135, 137, 139, 141
one-colour, 62, 77, 104, 109, 117, 139
rotationally resolved, 8
two-colour, 62, 104, 105, 121, 137
two-photon, 119
resonnce enhanced two-photon ionization (R2PI) UV, 95
rotational coherence (RC), 56, 60
ultraviolet (UV), 7
vibration-rotation tunnelling, 59
vibrational, 7
zero electron kinetic energy (ZEKE), 56, 57
spin, 28
nuclear, 49
splitting, 99, 101, 109, 111
spontaneous emission, 67
amplified, 67
stagnation pressure, 64, 137
state, 39
electronic, 125
excited, 119–121, 123
ground, 116, 123, 125, 128
stationary, 39
statistical weight, 49
stick spectrum, 85, 112, 120
Stokes, 59
structural optimization, 78
structure, 24, 25, 36
secondary, 24
stable-equilibrium, 36
supramolecular, 25
tertiary, 24
unstable-equilibrium, 36
styrene (ST), 9, 76–78, 81–87, 89, 90, 94, 95, 97, 98, 108
substituted benzene, 94
substitution, 104
isotopic, 51, 52
supersonic jet expansion, 55, 62, 76

supramolecular assembly, 76, 94
supramolecular chemistry, 6
surface, 36
  potential energy, 36
symmetry axis, 95, 125
  C_6, 101, 124, 131, 132
synthesis, 6

T

Tamm-Dancoff, 31
Tarakeshwar, 108, 111
targeted synthesis, 6
taylorization, 33
temperature
  rotational, 50, 69, 85, 97, 119, 120, 123, 124, 140
tensor of inertia, 45
theory of perturbations, 40, 50
thermocontroller, 64
toluene, 100, 131
top, 45
  asymmetric, 45, 48, 49
    oblate, 48
    prolate, 48
  spherical, 45
  symmetric, 45, 48
    oblate, 45
    prolate, 45
torsion, 88
transition, 39
  allowed, 41
  electronic, 117
  forbidden, 41
  one-photon, 49
  rotationless, 119
  two-photon, 49
transition dipole moment, 60
transition moment (TM), 8, 49, 112, 115, 128, 129, 132, 135, 143
  deviation, 129
  orientation, 91, 98, 114, 121, 124, 128, 129, 132
  projection, 123, 128
  ratio, 8, 68, 69, 78, 86, 87, 89, 97, 101, 112, 114, 119–121, 123–125, 129, 136, 141, 143
  vector, 89
trigger, 68
Tsuzuki, 76
tunnelling, 109
Turbomol, 38
turbomolecular pump, 63

V

vacuum chamber, 63, 67
van der Waals, 5, 9
vibration, 23, 76
  bending, 83, 95, 101
    long-axis, 99
    short-axis, 99
  intermolecular, 82, 109
  stretching, 23, 83, 95, 99, 101
    antisymmetric, 76
  swinging, 83
  twisting
    in-plane, 109
    out-of-plane, 109
vibrationally averaged, 45
vinyl substitution, 76
vinylbenzene (ST), 77
virus detection, 6

W

Wallenstein, 67
water, 64, 76, 130
wave function, 44
wavemeter, 67
Weinkauf, 117
Winnewisser, 59

Z

Zewail, 60
Zhu, 58

Acknowledgements

I would like to thank all those who have contributed to the succesfull completion of this work.

I give my special thanks to Prof. Dr. Hans Jürgen Neusser for the constructive work atmosphere in his group, for his involvement and keen interest in the scientific research, for his open-mindedness and tolerance and attention, for his support and willingness to help. I appreciate the stimulating discussions and the valuable advices he has given.

I warmly thank my colleagues and good friends, M. Sc. Stoyan Georgiev, and M. Sc. Rossen Karaminkov, for the nice time we have together, for their trust, understanding, responsiveness, attention, and help.

I would like to cordially thank Dr. Pengqian Wang for the motivating work I had with him, for his amicability, and friendly advices; Dr. Klaus Siglow and Dr. Julian E. Braun for their approachability and underastanding and their indispensable help during the initial stage of my work; Prof. Tapas Chakraborty for our fruitful cooperation and for the valuable suggestions, discussions, and ideas he has given; Dr. Heinrich Selzle for his affability, attention, and the expert help in various areas, especially in computers and quantum chemistry calculations.

I sincerely thank our secretary, Mrs. Thiem, for her responsiveness and assistance.

I thank also Mr. Max Wiedeman and Mr. Hans-Arnulf Müller and the staff of the Electroncs workshop for their indispensable help in the lab, Mr. Werner Tauchman for his assistance for solving computer problems, Mr. Otto Strasser and his colleagues from the Mechanics Workshop.

I would like to thank also all my colleagues from the Institute, and especially Dr. Martin Tschurl for his amiability and approachability and the valuable advices on the preparation of this work.

I thank all my friends for their support. I appreciate the responsiveness and help of Dr. Hristo Iglev.

I thank wholeheartedly all of my family for their love, encouragement, underastanding, and support.